Ground state properties of neutron-rich Mg isotopes – the “island of inversion” studied with laser and β-NMR spectroscopy

Dissertation
zur Erlangung des Grades
“Doktor der Naturwissenschaften”
am Fachbereich Physik, Mathematik und Informatik
der Johannes Gutenberg-Universität
in Mainz

Magdalena Kowalska
geb. in Poznań, Polen

Mainz, August 2006

Contents

List of Figures

List of Tables

Introduction

Our current understanding of both nuclear structure and nucleosynthesis is largely based on what is known about the properties of stable and long-lived, near-stable nuclei. Between these nuclei and the drip lines, where nuclear binding comes to an end, lies an unexplored landscape containing more than 90 percent of all expected bound nuclear systems, a region where many new nuclear phenomena are anticipated. The limits of the nuclear binding are poorly known at present and exploring them is expected to bring new information about the fundamental properties of the nucleonic many-body system, about astrophysical processes and the origin of elements, and about fundamental symmetries. New, unexpected phenomena may be discovered [Com99].

The strong interaction that binds nucleons together in nuclei is much more complex than the electromagnetic force that holds electrons in atoms, and atoms in molecules. While it is believed that nuclei can ultimately be described in terms of quantum chromodynamics (QCD), more empirical models of nuclear physics have provided a realistic framework for understanding a rich array of observed nuclear phenomena. These include shell structure, which makes some nuclei much more tightly bound than others; collective rotations and vibrations of many nucleons in the nucleus; transitions between regular and chaotic behavior in nuclear spectra; and weakly bound halo nuclei with an enormous increase in nuclear size. Deep insight into the crucial features of nuclear structure can be gained from an understanding of where these approximations work well and where they break down [Com99].

One region of the nuclear chart in which the nuclear structure described by the nuclear shell model appears to be anomalous consists of neutron-rich Ne, Na and Mg isotopes around the shell gap $N = 20$. While the shapes of nuclei at major shell closures are generally spherical, it is now clear from numerous experiments that at least some of the above mentioned isotopes are quite deformed in their ground states. This can be interpreted in terms of a reduction of the neutron shell gap and promotion of neutrons across $N = 20$ at surprisingly low excitation energies or even as the ground state, while leaving unoccupied single particle orbits below, thus the name of the region: “island of inversion”. However, physical reasons for such a behaviour are still not clear. Although this region has been investigated over about 30 years, it is not even known how many nuclei exhibit such anomalous properties. This situation requires further experimental and theoretical studies.

The study of ground state properties of several neutron-rich Mg isotopes presented in this thesis is motivated by the unclear situation concerning the borders and the origin of the “island of inversion”. It aims to contribute to the extensive experimental effort in exploring this interesting part of the nuclear landscape.

The outline of the thesis is as follows: in Chapter 1 a more detailed introduction to the "island of inversion" is given, followed by a motivation of our measurements. Chapter 2 summarises the importance of the ground state properties, i.e charge radii, spins and electromagnetic moments, in the description of nuclei, especially far from stability. It is followed by a part (Chapter 3) devoted to the nuclear information provided by laser and β-NMR studies, which includes nuclear parameters derived from the hyperfine structure, isotope shifts or nuclear magnetic resonance. Chapter 4 presents the experimental techniques: collinear laser spectroscopy, as well as optical pumping and nuclear polarisation, followed by a description of the experimental setup. The last two chapters are devoted to the experimental results (Chapter 5) on charge radii of $^{24-26}$Mg, together with spins and g-factors of ^{29}Mg and ^{31}Mg, as well as their interpretation (Chapter 6). The thesis is closed by a conclusion and an outlook.

Chapter 1

Motivation – “island of inversion”

The conceptual framework for the description of atomic nuclei is the shell model, in which each nucleon is assumed to move in an average potential generated by its interactions with all other nucleons in the nucleus. This potential, or mean field, leads to the prediction that the quantum levels in a nucleus form shells within which several nucleons can reside. Such a mean field picture of protons and neutrons explains a host of phenomena: the existence of particularly stable magic nuclei corresponding to completely filled shells, the properties of low-lying states of nuclei such as their energy and spin, and their collective response in the absorption of photons and other excitations. After including the residual part of the nucleon-nucleon interaction that could not be absorbed into the mean field, a one-to-one correspondence emerges between the resulting shell model states and the energy levels measured in nuclei. Many properties of the actual states, especially when the nucleus is probed at appropriately long wavelengths, are found to match closely those of the corresponding shell model states [Com99].

However, successful as it is, the shell model – with its shell gaps and magic numbers – fails in some parts of the nuclear landscape. One of such regions is located around $Z = 10 - 12$ and the $N = 20$ shell closure (Fig. 1.1), where a collapse of the usual shell model ordering of the single particle states takes place.

1.1 Experimental evidence

Nuclear masses

The first signature of unexpected properties of nuclei around $Z = 10 - 12$ and $N = 20$ came in 1975 from mass measurements of sodium isotopes [Thi75], where it was noted that ^{31}Na and ^{32}Na were considerably more bound than predicted theoretically for a closed $N = 20$ shell. The authors’ suggestion that this might be due to deformation, was supported shortly afterwards by Hartree-Fock calculations [Cam75] which could reproduce ^{31,32}Na binding energies only when promotion of neutrons from the $d_{3/2}$ to the $f_{7/2}$ intruder orbit was allowed[1], which also gave large deformations. The occupation of intruder orbits was very surprising, since $N = 20$ was believed to be a magic number and no excitations across the shell gap should be present at low excitation energies, let alone in the ground state. Later, mass measurements were extended to Mg isotopes and it was found that both ^{31}Mg and ^{32}Mg were also far

---

[1] The $f_{7/2}$ orbit is called an intruder state, since it belongs to the next major shell, as shown in Fig. 1.1.

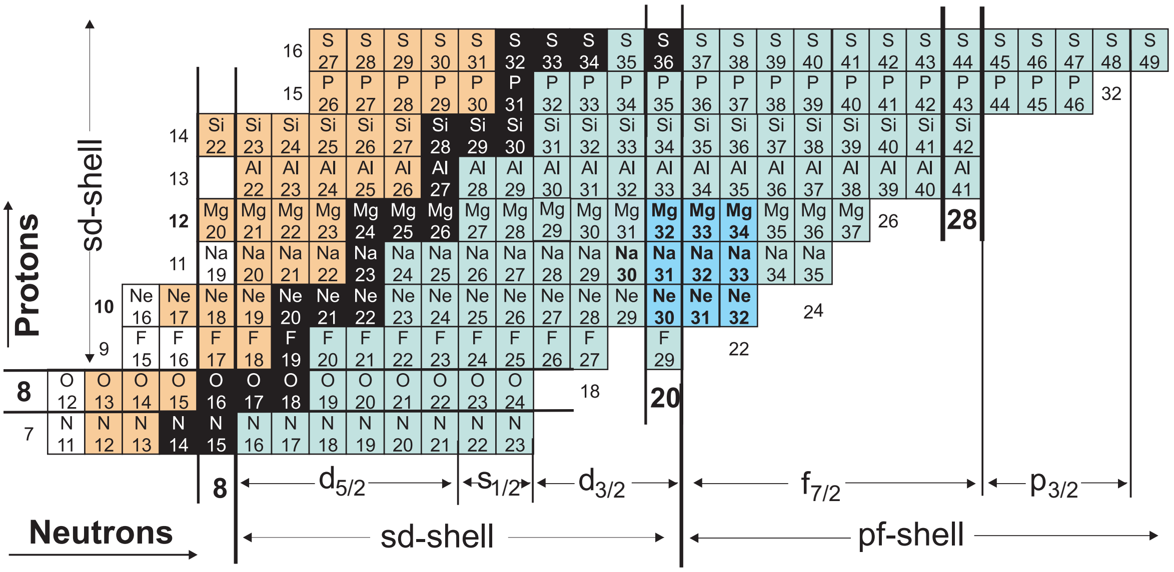

Figure 1.1: Part of the nuclear chart around the "island of inversion". Neutron and proton numbers, as well as different nuclear shells are shown.

more bound than expected. These studies were repeated and extended with use of different techniques (for recent tabulated values see [Aud03]). In the cases of Ne, Na and Mg around $N = 20$ even most recent models assuming a closed *sd* shell cannot predict the experimental binding energies, although they are successful in other cases. Moreover, nuclei with the same number of neutrons, but more protons ($Z > 12$, e.g. S) do not exhibit such strange properties, as presented for example in Fig. 1.2 or 1.4. Both of these facts and their interpretation in terms of pf-shell intruder states gave rise to the name of the region: the "island of inversion" [War90]. In the original publication this region was predicted to include only nuclei with $Z = 10 - 12$ and $N = 20 - 22$. In this thesis the term "island of inversion" will be applied in a broader sense to nuclei around $N = 20$ for which intruder states from the pf shell influence the properties of nuclear states at low excitation energies or even of the ground state.

Another indication for a closing of a neutron shell derivable from nuclear masses is a sharp drop in the two-neutron separation energy[2] S_{2n} with increasing number of neutrons. This effect is due to filling of a new neutron shell with smaller binding energy. Such a plot for nuclei in the region of interest is presented in Fig. 1.3. For Na and Mg isotopes there is no sharp decrease in S_{2n} as one crosses $N = 20$, which confirms that the shell is not closed there. This is in contrast to neighbouring chains of isotopes, especially K or Ca, where a clear drop can be observed.

Energies and transition probabilities of first 2^+ states in even-even nuclei

The strange behaviour of Na and Mg isotopes, derived from mass measurements, was confirmed by studies of the excitation energy of the first excited 2^+ state in even-even Ne and Mg isotopes. For $N = 20$ isotones, ^{30}Ne [Yan03] and ^{32}Mg [Det79], as well as for ^{34}Mg [Yon01] with 22 neutrons, this level was found at a remarkably low energy around 0.8 MeV, clearly indicating deformation properties. Systematics of $E(2^+)$ in this area of the nuclear chart are

---

[2] S_{2n} is the energy needed to remove two neutrons from a nucleus. It is used more often than the one-neutron separation energy, because it allows to ignore the influence of the pairing force causing even-neutron nuclei to be more bound than their odd-neutron neighbours, which can blur the effects of a shell closure.

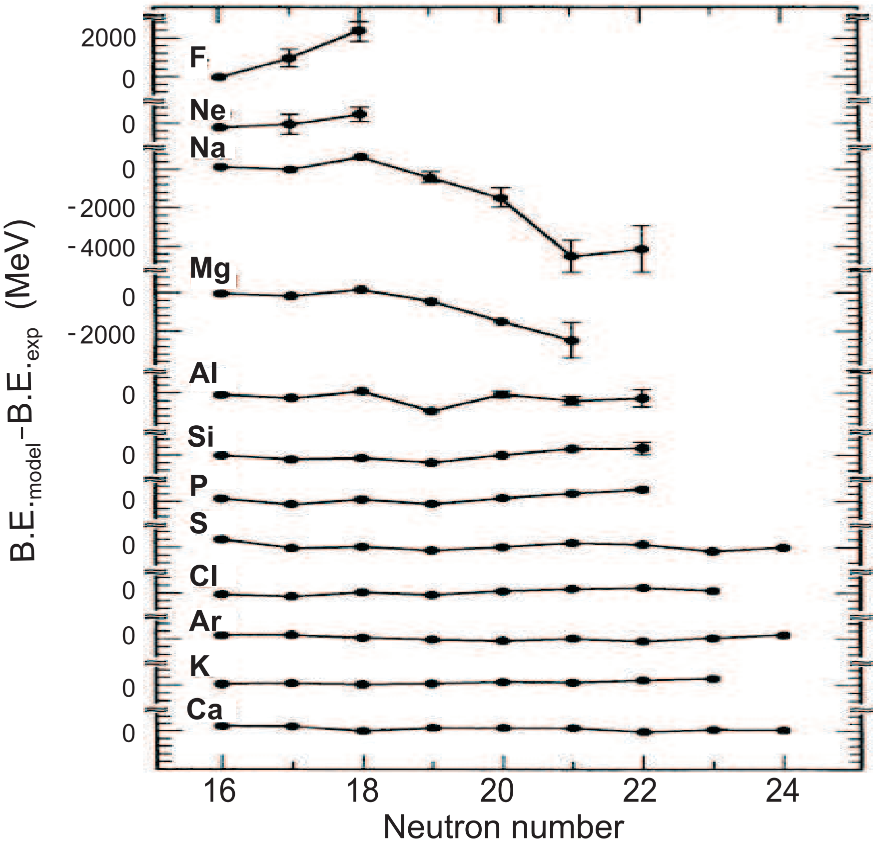

Figure 1.2: Ground state binding energies of *sd* and *sd-pf* nuclei: difference in measured values and predictions based on the shell model assuming a closed $N = 20$ core, from [War90]. Clear discrepancies are visible for neutron-rich Ne, Na and Mg isotopes.

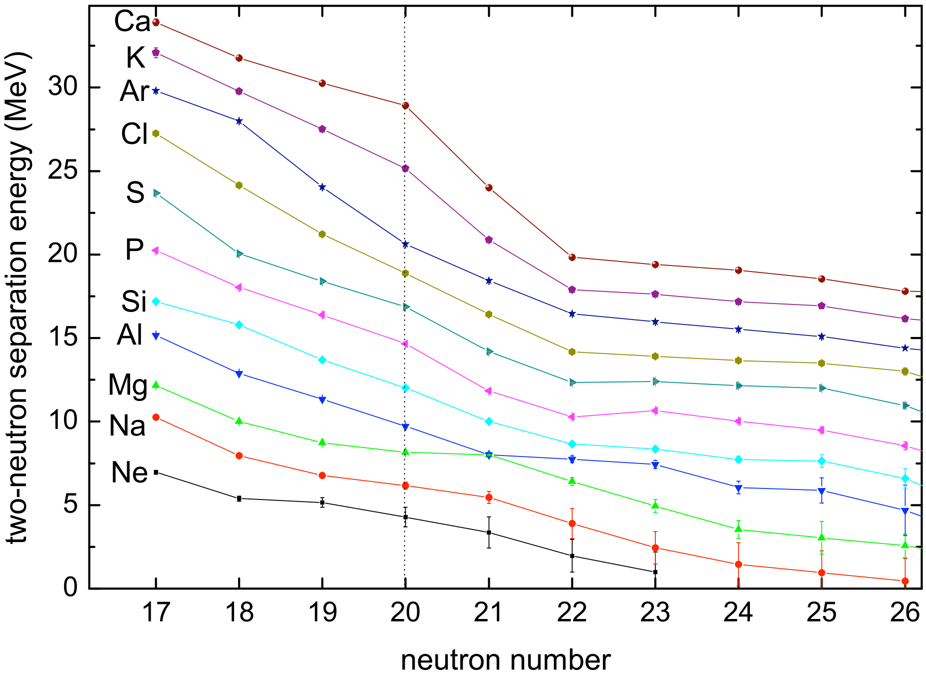

Figure 1.3: Measured two-neutron separation energies for nuclei around around $N = 20$ and $Z = 10 - 20$. Ne, Na and Mg isotopes show a clear deviation from a closed $N = 20$ shell. Data taken from [Aud03] and [Aud06].

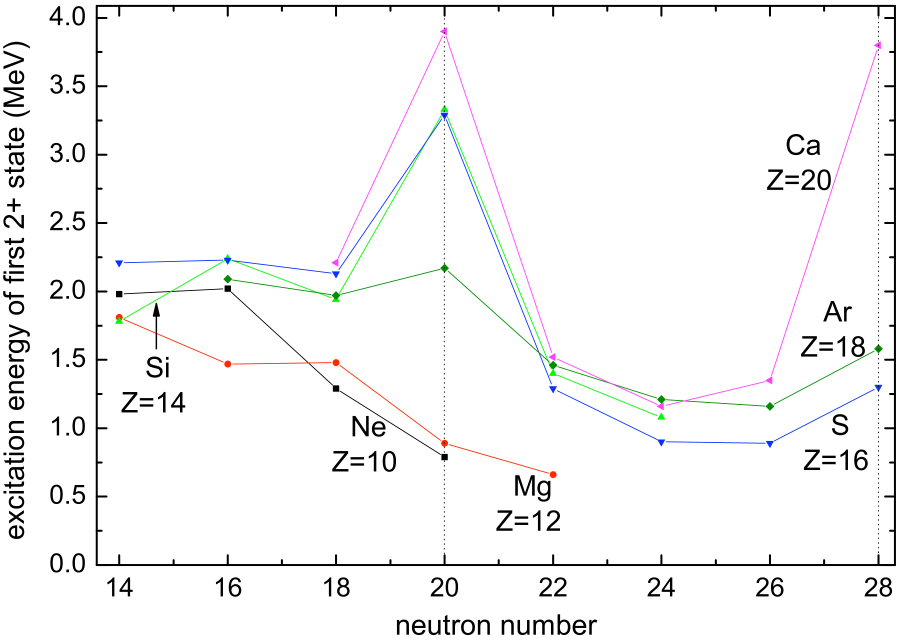

Figure 1.4: Experimental energies of first 2^+ states in even-even nuclei around "island of inversion". The drop at $N = 20$ for Ne and Mg points to deformation and absence of a closed shell. Source: [Fir03], [Iwa05], [Yan03] and [Yon01].

shown in Fig. 1.4, from which it is easy to see that probably also ^{28}Ne, with 18 neutrons, has a deformed ground state. At the same time Si, S, Ar or Ca show typical characteristics of a closed shell, namely a large 2^+ excitation energy at $N = 20$ [Fir03].

More recently, also reduced transition probabilities $B(E2)$ from the 0^+ ground state to the first excited 2^+ state have been measured [Mot95]. Although the data from different facilities in several cases are still not consistent with each other, the results indicate a large deformation around $N = 20$ (see Fig. 1.5). It is clear that ^{30}Ne and ^{32,34}Mg have large $B(E2)$ values [Mot95], [Pri99], [Iwa01], [Chi01], [Yan03], whereas data for $N = 18$ isotones, ^{28}Ne [Iwa05] and ^{30}Mg, [Pri99], [Chi01], [Sch05] are not yet conclusive.

Differences in charge radii

Early efforts using laser spectroscopy of Na isotopes [Hub78] revealed an increase in mean square charge radius for ^{29}Na ($N = 18$), consistent with the onset of deformation. Later measurements on Ne, performed by our group up to $N = 18$ [Gei02] showed that the charge radius and thus the deformation for ^{28}Ne is larger than expected for the approach to an $N = 20$ magic number, thus confirming the deformed character suggested by the low energy of the first 2^+ state. For Mg no such measurements have been performed prior to this study. The same is the case for other neighbouring isotope chains, such as F, Al or Si.

Electromagnetic moments

Deformations around $N = 20$ were also observed in the early studies on magnetic moments of $^{26-31}$Na performed at CERN [Hub78] in connection with measurements of charge radii mentioned in the previous paragraph. Precise quadrupole moments were obtained recently

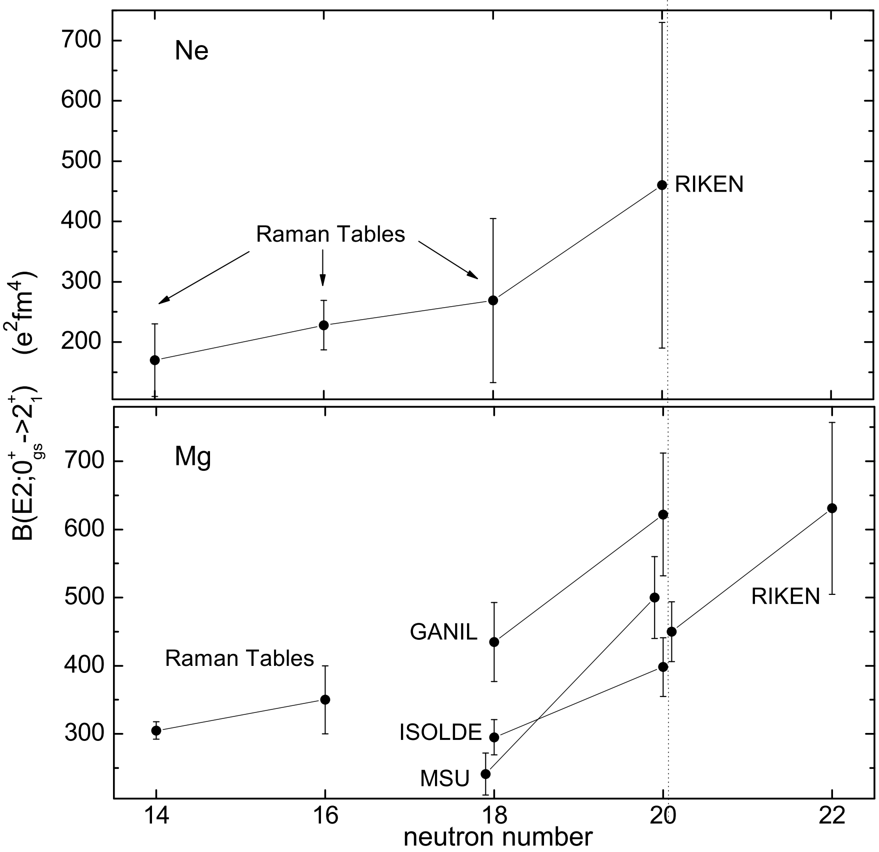

Figure 1.5: $B(E2; 0^+_{g.s.} \rightarrow 2^+_1)$ values for neutron-rich even-even Ne and Mg isotopes. An increase is clear for isotopes with 20 and 22 neutrons, which is a sign of large deformations. References: [Yan03], [Chi01], [Mot95], [Pri99], [Iwa01], [Sch05] and [Ram01].

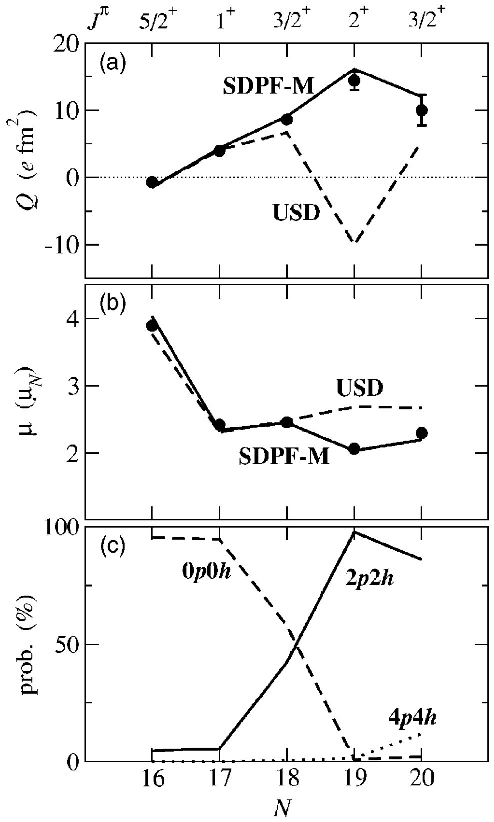

Figure 1.6: Electromagnetic moments and the contributions to the wave-function from 0 (0*p*0*h*), 2 (2*p*2*h*) and 4(4*p*4*h*) neutrons in the *pf* shell for the ground states of neutron-rich Na isotopes, as a function of the neutron number. Taken from [Uts04].

by our group using β-NMR and optical polarisation techniques [Kei00], [Wil98]. The results show strong deformations present at $N = 19, 20$ and to some extent also at $N = 18$ (see also [Uts04]).

In Fig. 1.6 the experimental magnetic and quadrupole moments are compared with the results of an *sd*-shell model calculation (USD interaction) and a Monte Carlo shell model calculation (SDPF-M interaction) allowing promotion of neutrons into the *pf* shell [Uts04]. There are clear deviations from the *sd*-only picture for $N = 20, 21$ and partly for $N = 19$. At the same time, the *sd*-*pf* model shows remarkable agreement throughout the Na isotope chain and it predicts a two-neutron intruder ground state for $^{30-31}$Na with $N = 20$ and 21 neutrons, as well as a 50 % mixture of a normal and intruder state for ^{29}Na.

For Ne no data exist for very neutron-rich isotopes. However, the Leuven group has very recently measured magnetic moments of Al isotopes, which lie at the border of “island of inversion”. For $N < 20$ they find very good agreement with a closed *sd* shell, whereas ^{33}Al and ^{34}Al with $N = 20$ and 21 are found to contain partly an intruder configuration [Him06a], [Him06b].

The above results show the importance of nuclear electromagnetic moments in the determination of the ground state wave-function and in the identification of the borders of the “island of inversion”, since contributions from intruder states can change μ_I and Q quite drastically.

1.2 Theoretical explanation

Since the discovery of large deformation around $N = 20$, intensive theoretical effort has been concentrated on this phenomenon. The calculations by Campi *et al.* [Cam75] were followed by other theoretical work using also Hartree-Fock aproach [Ter97], as well as the shell model [Chu80], [Pov87], [War90], [Fuk92], [Cau98] and the relativistic mean field approach [Pat91], [Ren96]. As a result, the first suggestions from 1975 that the observed large deformations are due to a promotion of neutrons across the magic $N = 20$, were quickly confirmed by other theoretical calculations.

It is important to consider the origins of such a surprising behaviour so close to an expected shell closure. Presently, it is rather commonly agreed that there are two contributions: a lowered *sd-pf* shell gap and a large correlation energy E_{corr} for deformed intruder states with neutrons in the pf shell. If the energy gain due to these dynamical correlations is larger than the gap, promotion of neutrons beyond $N = 20$ is more favoured that the shell closing, as it is apparently the case in the "island of inversion".

1.2.1 Decreased shell gap

The change in the $N = 20$ gap for nuclei around $Z = 10 - 12$ was first postulated by Storm *et al.* [Sto83], who saw in their shell model calculations that the single particle energy of the neutron $f_{7/2}$ orbit actually dropped below $d_{3/2}$. Most present authors predict a decrease of the *sd-pf* shell gap, but do not find it as drastic as leading to the inversion of the orbits (see e.g. Warburton *et al.* [War90]). It is now commonly agreed that one of reasons for the existence of the "island of inversion" is a smaller, but still positive, $d_{3/2}$-$f_{7/2}$ gap compared to nuclei closer to β stability.

Proton-neutron "spin-flip" interaction

Otsuka *et al.* [Ots01] proposed that the decrease in the shell gap for neutron-rich nuclei is due to neutron-proton "spin-flip" interaction (called also spin-isospin interaction, since it inverts both spin and isospin). This interaction is strongly attractive for spin-orbit partners, i.e. a proton and a neutron occupying orbitals with the same orbital angular momentum ($\Delta\ell = 0$), but with different total angular momentum ($\Delta j = 1$), such as a $d_{5/2}$ proton and a $d_{3/2}$ neutron[3]. Due to this interaction the effective single-particle energy, i.e. the single-particle energy including effects of the monopole interaction with other valence nucleons, of the neutron $d_{3/2}$ orbital is much smaller for stable nuclei, for which the proton $d_{5/2}$ orbital is nearly filled and a strong attraction of the nucleons in these two orbitals takes place. This is in contrast to very neutron-rich nuclei, where the proton $d_{5/2}$ orbit is nearly empty and thus the neutron $d_{3/2}$ is lifted up and moved closer to the pf orbitals, thus decreasing the $N = 20$ shell gap. The described difference is schematically illustrated in Fig. 1.7.

Tensor interaction

The one-pion exchange produces another important interaction, the tensor (non-central) interaction [Ots05], whose monopole component is responsible for the shift of the nuclear levels.

---

[3] This mechanism has origins in the theory of the strong force, quantum chromodynamics, where it is caused by the one-pion exchange.

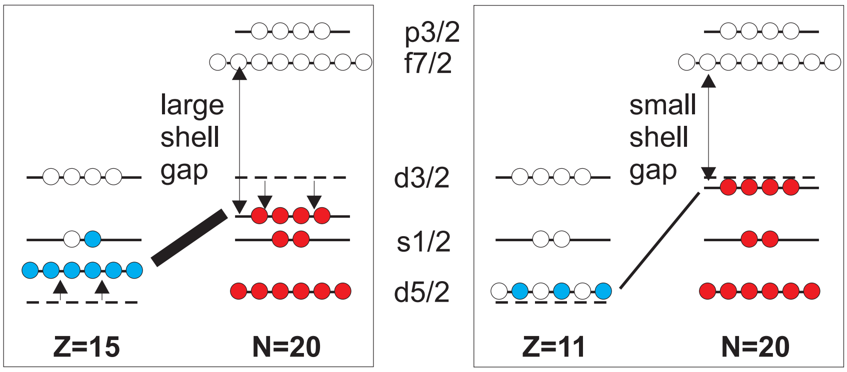

Figure 1.7: Schematic picture of the proton-neutron "spin-flip" interaction for a nucleus outside (left) and inside (right) the "island of inversion". Thick diagonal line corresponds to a strong interaction, thin line to a weak interaction. The $N = 20$ shell is larger for $Z > 12$ due to a strong attractive interaction between the proton in a $d_{5/2}$ orbit and neutron in a $d_{3/2}$ orbit. Based on [Ots05].

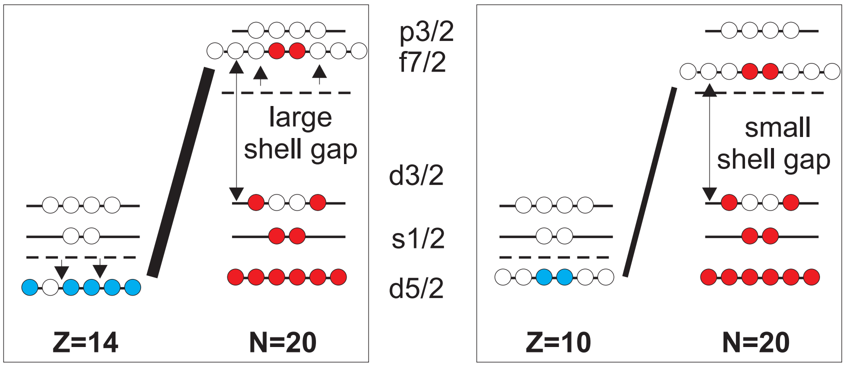

Figure 1.8: Schematic representation of the orbital shift due to the repulsive tensor force between a proton in a $d_{5/2}$ orbit and a neutron in a $f_{7/2}$ orbit for a nucleus outside (left) and inside (right) the "island of inversion". Thick diagonal line corresponds to a strong interaction, thin line to a weak interaction. Adapted from [Ots05].

The tensor force is attractive between a proton with angular momentum $\ell + 1/2$ and a neutron with $\ell' - 1/2$ (and vice versa), whereas it is repulsive for a proton with $\ell + 1/2$ and neutron with $\ell' + 1/2$ (or $\ell - 1/2$ and $\ell' - 1/2$). This force is strongest between protons and neutrons in orbits of different parity and orbital angular momenta ($\ell \neq \ell'$).

A situation typical for the nuclei around the "island of inversion" is presented in Fig. 1.8, where neutrons are placed in the $f_{7/2}$ orbit and protons fill the $d_{5/2}$ orbit. Since nucleons in these orbits have spin $\ell + 1/2$ and $\ell' + 1/2$, their tensor interaction will be repulsive. For nuclei close to stability the $d_{5/2}$ orbit is filled and therefore the repulsion is strong. Hence it pushes the $f_{7/2}$ neutron orbit strongly upwards and creates a large $N = 20$ shell gap. For nuclei with $Z \approx 11$ inside the "island of inversion" the proton $d_{5/2}$ orbit is only half-filled and the interaction is less repulsive, which leads to a smaller neutron $d_{3/2}$-$f_{7/2}$ gap. However, the quantitative influence of the tensor force on single particle energies in this region has not been studied so far.

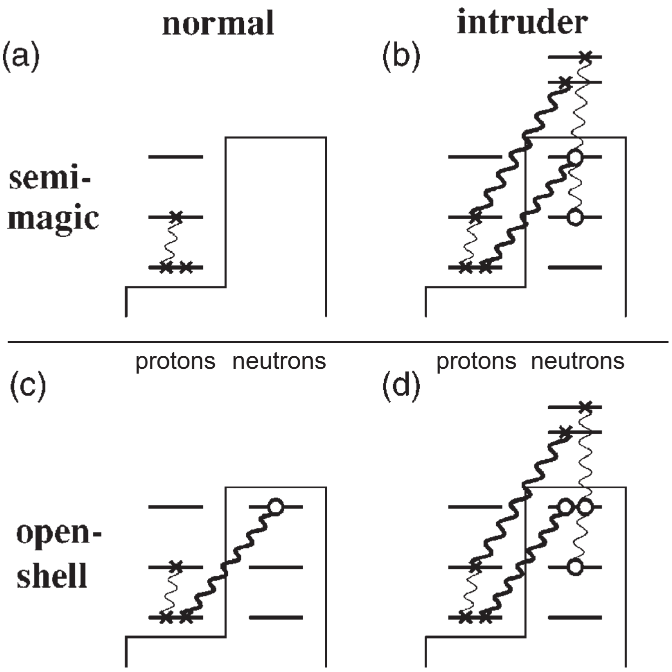

Figure 1.9: Schematic sketch of the suggested sources of the correlation energy for intruder and normal states (a), (b) of semi-magic and (c), (d) open-shell nuclei. Rectangles denote closed shells. Thick wavy lines show the stronger proton-neutron correlations, thin lines represent weaker correlations between like nucleons. Typical configurations for these states are shown. Taken from [Uts04].

1.2.2 Correlation energy

The importance of correlations between nucleons for the occurence of the “island of inversion” was first pointed out by Poves and Retamosa [Pov87], [Cau98]. It was suggested that correlation energy includes proton-neutron quadrupole interaction [Cau02], [Ots01], as well as pairing interaction between like nucleons coupled to total spin 0 [War90]. In Fig. 1.9 the sources of the correlation energy according to Utsuno *et al.* [Uts04] are presented schematically (according to the authors the proton-neutron interaction produces much larger correlation energies than for like nucleons). In a normal *sd* state of a semi-magic nucleus ($N = 20$), only the proton rearrangement is relevant to the correlation energy E_{corr}, which is generally small (a). On the other hand, E_{corr} is very large in the case of a pf intruder state, due to large numbers of particles and holes in active orbits (b). For this reason $N = 20$ nuclei will favour an intruder configuration even with a large shell gap. On the other hand, in an open-shell nucleus a normal *sd* state has a neutron hole already causing larger correlation energy (c) than in a semi-magic nucleus. The neutron rearrangement is then also possible and E_{corr} is even stronger, like for $N = 20$ nuclei. However, the difference in E_{corr} between (a) and (b) is larger than for (c) and (d), due to the saturation of the correlation energy with many particles and many holes, as it is the case in (d). This implies that the intruder dominance becomes less favoured as N goes away from 20, which corresponds to the experimental observations.

The above discussion also implies that normal-dominant and intruder-dominant states compete with each other in nuclei around $N = 20$. It is probable that these two configurations coexist in the low-lying energy region. Utsuno *et al.* [Uts02] give as an example ^{34}Si which has a normal ground state and a low-lying intruder 2^+ state. It would be very interesting to investigate this phenomenon around the "island of inversion" also among the known low-energy levels in odd-N nuclei such as ^{31}Mg.

To summarise this theoretical section, the phenomenon of the "island of inversion" around $N = 20$ is still not fully understood, although there exist possible explanations for the underlying physical mechanism. This area of the nuclear chart is very important, since it probes the nuclear interaction between nucleons in two different shells, *sd* and pf. If studied more intensively, this cross-shell region could provide valuable input in our understanding of the strong force in the nuclear medium as a whole. It is therefore of high importance to collect more specific experimental data, especially concerning the electromagnetic moments and spins, which are very sensitive to the composition of the nucleon wave-function (see Section 2.3). Measurements of ground state properties of neutron-rich Mg isotopes presented in this thesis aim to contribute to this intensive research programme pursued around the world.

1.3 Known properties of neutron-rich Mg isotopes

As a starting point for the presentation of measurements and experimental results described further in this thesis, Table 1.3 summarises the ground state properties of neutron-rich Mg isotopes (with $N > Z$) known prior to our measurements.

Table 1.1: Ground state properties of neutron-rich Mg isotopes ($Z = 12$). For charge radii the uncertainty is split in the statistical (1st bracket) and systematic part (2nd bracket). Data taken from [Fir03], [Aud03], [Fri95] and [Rag89].

	N	mass$-A$ (μu)*	$t_{1/2}$	I^π	$\langle r^2\rangle^{1/2}$ (fm)	μ_I (μ_N)	Q (mbarn)
^{24}Mg	12	$-15506.88(1)$	stable	0^+	3.057(1)(70)	0	0
^{25}Mg	13	$-14711.66(3)$	stable	$5/2^+$	3.029(1)(70)	-0.85546(1)	201(3), 199.4(20)
^{26}Mg	14	$-17955.65(3)$	stable	0^+	3.034(1)(70)	0	0
^{27}Mg	15	$-16207.99(5)$	9.5 min	$1/2^+$	unknown	unknown	unknown
^{28}Mg	16	$-16671.8(22)$	20.9 h	0^+	unknown	0	0
^{29}Mg	17	$-11949(15)$	1.3 s	$3/2^+$	unknown	unknown	unknown
^{30}Mg	18	$-10115(9)$	335 ms	0^+	unknown	0	0
^{31}Mg	19	$-4003(13)$	230 ms	$(3/2)^+$	unknown	unknown	unknown
^{32}Mg	20	$-1574(19)$	120 ms	0^+	unknown	0	0
^{33}Mg	21	4705(21)	90 ms	unknown	unknown	unknown	unknown
^{34}Mg	22	8911(250)	20 ms	0^+	unknown	0	0

* mass = mass of a singly charged ion, Mg$^+$

From this tabulated summary it is clear that not much is known about the ground state properties of these nuclei, except for spins and parities of even-N isotopes (equal to 0^+) and of odd-N isotopes with $N \leq 17$, which naturally agree with the *sd*-shell picture, since they are far away from $N = 20$. Close to $N = 20$, not even the spins of odd-A isotopes are unambiguously assigned. For the electromagnetic moments, the situation is much worse, as data exist only for the stable odd-even ^{25}Mg.

This situation can be largely improved by our measurements. In this thesis I will present the first part of a study on changes in charge radii (for stable Mg isotopes), serving as a starting point for planned measurements on radioactive isotopes. I will mainly discuss the measurements on spins and electromagnetic moments of ^{29}Mg and the highlight nucleus, ^{31}Mg.

Chapter 2

Nuclear ground state properties

Among other nuclear characteristics, the ground state properties such as spin, charge radius, and electromagnetic moments, contribute considerably to our understanding of the nuclear landscape by giving us the static picture of a system of nucleons. These observables reveal valuable information about the coupling between nucleons, about symmetry of the nuclear wave-functions and thus about the symmetry of the nuclear interaction itself. In this way, for example, the discovery that the nuclei can possess electric quadrupole moment [Sch35],[Kel39] gave the decisive proof for the existence of non-central (tensor) parts of the nucleon-nucleon force [Bla52].

2.1 Charge radius

The nuclear radius, like the radius of an atom, is not a precisely defined quantity: neither atoms nor nuclei are solid spheres with abrupt boundaries or a constant density. Therefore an average quantity has to be defined to describe the size of a nucleus. Experimental observables are usually sensitive to the second radial moment of the nuclear matter or charge distribution, therefore a widely used quantity is the mean square radius $\langle r^2 \rangle$, defined as

$$\langle r^2 \rangle = \frac{\int \rho(\boldsymbol{r}) r^2 \, d^3r}{\int \rho(\boldsymbol{r}) \, d^3r} \;, \tag{2.1}$$

where the $\rho(\boldsymbol{r})$ represents the matter or charge density distribution of the nucleus, and $\int \rho(\boldsymbol{r}) \, d^3r$ is the normalisation factor equal to the total mass or charge of the nucleus.

The electromagnetic interaction, used as a probe of the nucleus in the measurements described in this thesis, is only sensitive to the charge distribution. Thus the quantity important in this context is the charge radius, which reflects the proton distribution inside the nucleus. Information about this radius can be gained from electron scattering, X-ray transitions in muonic atoms, or optical transitions in "normal" atoms. In the last method the mean square radii, or rather their changes from one isotope to another, can be derived.

If the nuclear density distribution is spherical, it is common to parametrise it and describe it with the so called Fermi distribution [Nil95] given by

$$\rho(r) = \frac{\rho_0}{1 + e^{(r - R_{1/2})/a}} \;, \tag{2.2}$$

where $t = 4a \ln 3$, and $\int 4\pi r^2 \rho(r) dr = Ze$. The two parameters in this formula are the mean radius $R_{1/2}$, at which the density is half its central value, and the "skin thickness" t, over

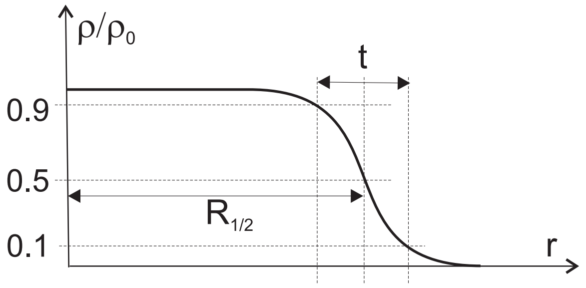

Figure 2.1: Mean radius and skin thickness of a nucleus.

which the density drops from 90 % to 10 % of its central value [Kra88], as presented in Fig.2.1.

However, nuclei are not necessarily spherical. The shell structure causes deformed equilibrium shapes mainly in the regions between the shell closures of protons and neutrons. Usually this deformation is described by a quadrupole deformation parameter β defined by an angular dependence of the length of the radius vector to the nuclear surface expressed in spherical harmonics. Assuming rotational symmetry, β can be related to the mean square radius of a deformed nucleus by

$$\langle r^2 \rangle = \langle r^2 \rangle_{sph} \, (1 + \frac{5}{4\pi}\beta^2) \ , \tag{2.3}$$

where $\langle r^2 \rangle_{sph}$ is the mean square radius of a spherical nucleus which has the same volume. The quantity accessible to laser spectroscopy measurements is the difference in charge radii $\delta\langle r^2 \rangle^{A,A'} = \langle r^2 \rangle^{A'} - \langle r^2 \rangle^{A}$ for different isotopes of the same chemical element. This observable is sensitive to changes of the nuclear shape.

For example, the study of $\delta\langle r^2 \rangle$ showed that the charge radii of ^{181,183,185}Hg are much larger than those of the more neutron-rich Hg isotopes [Ulm86], which is a sign of strong prolate deformation. As another example, the recently measured nuclear charge radius of ^{11}Li is comparable with the radii of other Li isotopes [San06], although – at the same time – its matter radius is much larger [Tan85]. This is a clear signature of a halo phenomenon [Arn87], [Han87], where weakly bound valence neutrons form a so called halo around the spherical ^{9}Li core.

2.2 Spin

In contrast to atoms, in nuclei the term "spin" is not reserved only to intrinsic angular momentum of the constituents, but it describes the whole system containing the total angular momenta $\boldsymbol{j}_k$ of all nucleons, arising from the coupling of orbital and intrinsic momenta, $\boldsymbol{l}_k$ and $\boldsymbol{s}_k$. To the extend that the nuclear potential is central, $\boldsymbol{l}_k$ and $\boldsymbol{s}_k$ (and thus $\boldsymbol{j}_k$) are constants of motion, and thus every nucleon can be labelled with the corresponding quantum numbers ℓ_k, s_k and j_k [Kra88]. The total spin of the nucleus $\boldsymbol{I}$ can be then obtained by adding the spins of all nucleons. Like elsewhere in quantum mechanics $\boldsymbol{I}^2 = \hbar^2 \, I \, (I+1)$ and $I_z = m \, \hbar$, with $m = -I, ..., I-1, I$. Similar to atomic physics, the paired protons and neutrons do not contribute to the total spin, and $\boldsymbol{I}$ is determined only by the unpaired nucleons. For many applications involving angular momentum the nucleus behaves as if it was a single entity with the intrinsic spin I.

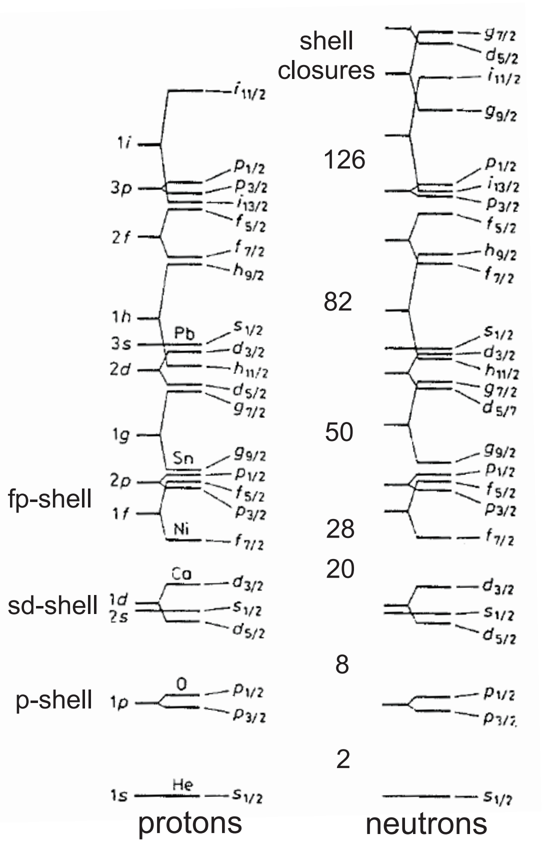

Figure 2.2: Level ordering in the nuclear shell model with the spin-orbit splitting. From [Kra88].

Due to a strong pairing force, in the nuclear ground state normally at most one neutron or/and proton is unpaired. Hence, all even-even nuclei have $I = 0$, for odd-even nuclei the spin is determined by the single unpaired nucleon, and in the odd-odd case I is given by the coupling of spins of the valence neutron and proton. Exceptions from this rule are odd-even nuclei with $I = j - 1$, where the so called "anomalous coupling" takes place due to large contributions from the quadrupole interaction (see e.g. [Ike66]).

In the simplified picture of single-nucleon orbits, in analogy to the atom, the protons and neutrons fill independently energy shells which are characterized by spin and parity. Due to a very strong spin-orbit coupling, the shell gaps and the magic numbers associated with them are slightly different from the atomic case. The nuclear ordering of levels and magic numbers are shown in Fig. 2.2.

The measured values of I provide basic information about the nuclear structure. Its prime use is the determination of single-particle orbits occupied by the valence nucleons.

2.3 Electromagnetic moments

In a simple picture the atomic nucleus has a point-like structure and the electrostatic potential it creates has spherical symmetry. In reality the nuclear charge and current distributions are more complex and may be expanded into electromagnetic multipole moments [Rin80] of higher order than the electric monopole. Of these, the magnetic dipole moment μ_I and electric quadrupole moment Q play the dominant role. The importance of electromagnetic moments in the understanding of nuclei can be attributed to the well-defined, simple structure of the electromagnetic operators.

2.3.1 Magnetic dipole moment

The magnetic moment is connected to the nuclear magnetisation. It arises from the current distribution of moving charged nucleons (protons), related to their orbital angular momenta $\boldsymbol{\ell}_k$, as well as from magnetic fields due to the intrinsic angular momentum of all nucleons (both protons and neutrons), the spins $\boldsymbol{s}_k$. The magnetic dipole moment operator $\boldsymbol{\mu_I}$, which includes magnetic contributions from all nucleons, is given by [Rin80]

$$\boldsymbol{\mu_I} = \sum_{k=1}^{A} g_l^k \, \boldsymbol{\ell}_k + \sum_{k=1}^{A} g_s^k \, \boldsymbol{s}_k \ , \tag{2.4}$$

where g_l^k and g_s^k are the gyromagnetic ratios of the k-th nucleon.

In experiments one observes the magnetic moment μ_I, which is the expectation value of the dipole operator in the nuclear sub-state $|I, m_I = I\rangle$:

$$\mu_I = \langle I, m = I | \boldsymbol{\mu}_I | I, m = I \rangle \ . \tag{2.5}$$

In analogy to free nucleons

$$\boldsymbol{\mu_I} = g_I \boldsymbol{I} \, \mu_N \tag{2.6}$$

and $\mu_I = g_I I \, \mu_N$, where g_I is the nuclear g-factor and the nuclear magneton $\mu_N = e\hbar/2m_p$ related to the proton mass m_p is the natural unit of μ_I.

In the extreme single-particle model, the magnetic moment of an odd-mass nucleus is given by that of an unpaired nucleon. Using the moments of the free proton and neutron, $\mu_p = 2.79 \, \mu_N$ and $\mu_n = -1.91 \, \mu_N$ one obtains [Rin80], [Cas90] in this way for the odd proton

$$\mu = (j - 1/2) + \mu_p \qquad \text{for } j = \ell + 1/2 \ , \tag{2.7}$$

$$\mu = \frac{j}{j+1} \, (j + 3/2 - \mu_p) \quad \text{for } j = \ell - 1/2 \ , \tag{2.8}$$

and for one the odd neutron

$$\mu = \mu_n \qquad \text{for } j = \ell + 1/2 \ , \tag{2.9}$$

$$\mu = -\frac{j}{j+1} \, \mu_n \quad \text{for } \ j = \ell - 1/2 \ , \tag{2.10}$$

The above predictions can be compared with the measured magnetic moments in a so called Schmidt diagram, as shown in Figs. 2.3 and 2.4. If the theory was exact, all μ_I values would lie on the Schmidt lines. However, the experimental magnetic moments, almost without exception, lie in between the two lines, most of them being grouped closer to one of the lines. This discrepancy has two possible sources. Firstly, the single-particle wave-function is certainly not the full description of nuclei. Secondly, the core is assumed to be inert and not to contribute to the measured magnetic moment. However, if configuration mixing is included [Ari54] and the nucleons are allowed to be described by a superposition of single-particle orbits or if "effective" g-factors are introduced [Rin80] accounting for the so called "core polarisation", the calculated magnetic moments in many cases agree remarkably well with the experiment.

From the above discussion it is visible that the magnetic moments are very sensitive to the nucleon configuration and they serve as an excellent tool to investigate the nuclear levels and their composition, in particular also their parity.

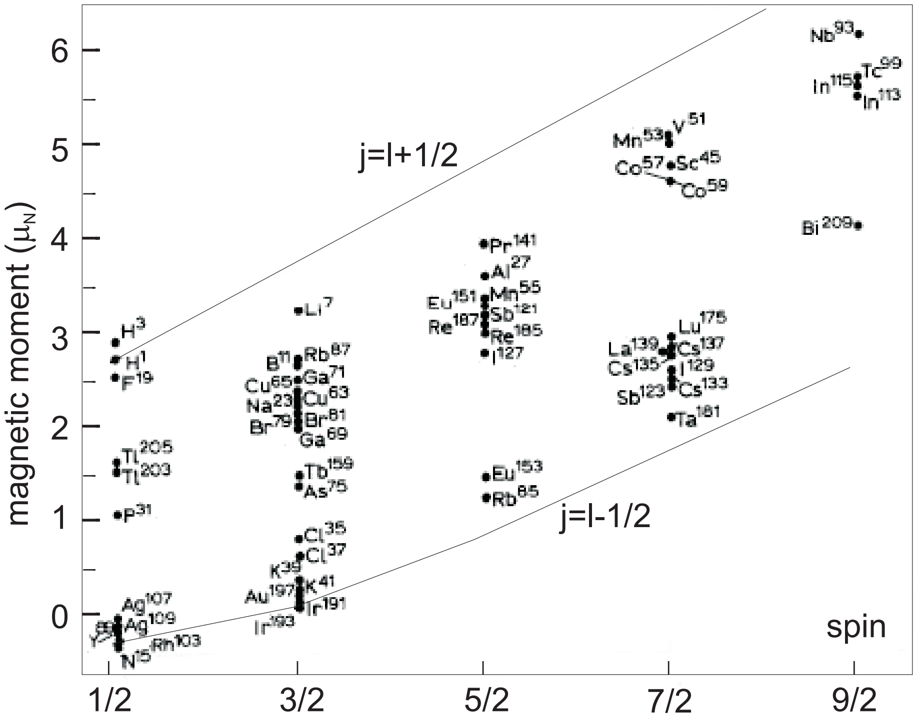

Figure 2.3: Schmidt magnetic moments of odd-Z even-N nuclei as a function of angular momentum. Adapted from [Kop69].

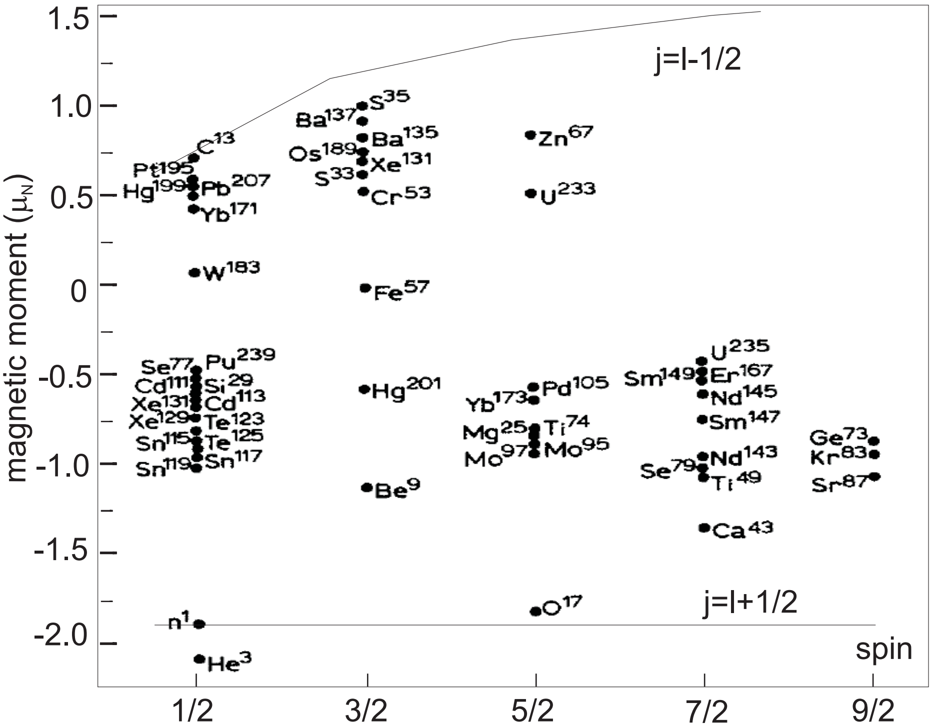

Figure 2.4: Schmidt magnetic moments of odd-N even-Z nuclei as a function of angular momentum. Adapted from [Kop69].

2.3.2 Electric quadrupole moment

The electric quadrupole moment Q is another important property of the nucleus, which describes the non-sphericity of the nuclear charge distribution. Its operator is given by [Rin80]

$$\boldsymbol{Q} = \sqrt{\frac{16\pi}{5}} \sum_{k=1}^{A} q_k {r_k}^2 \, Y_2^0(\theta_k, \phi_k) = \sum_{k=1}^{A} q_k {r_k}^2 (2\cos^2\theta_k - 1) \; , \tag{2.11}$$

where $q_k = e$ is equal to the unit charge for protons, and $q_k = 0$ for neutrons.

As in the case of μ_I, the experimentally observed quantity, i.e. the spectroscopic electric quadrupole moment, is equal to the expectation value of $\boldsymbol{Q}$ in the state $|I, m_I = I\rangle$ [Rin80]:

$$eQ = \langle I, m = I | \boldsymbol{Q} | I, m = I \rangle \; . \tag{2.12}$$

The spectroscopic quadrupole moment Q of a nuclear state with spin $I < 1$ is zero [Neu06]. Hence, although a nucleus with spin $I = 0$ or $1/2$ can possess an intrinsic deformation, one can not measure this via the quadrupole moment. For $I > 1/2$ the quadrupole moment is positive when the nuclear charge distribution is elongated along the spin direction (prolate), and negative when it is flattened (oblate).

For well deformed nuclei one can define an intrinsic quadrupole moment Q_0 which can be related to the observed Q only if certain assumptions are made. When the nuclear deformation is axially symmetric with the nuclear spin having a well-defined direction with respect to the symmetry axis of the deformation, their relation is the following [Poe96]

$$Q_0 = Q \, \frac{(I+1)(2I+3)}{3K^2 - I(I+1)} \; , \tag{2.13}$$

where K is the projection of the nuclear spin onto the deformation axis. This parameter is further connected with the deformation parameter β [Rin80] introduced in eqn. 2.3:

$$Q_0 = \frac{3}{5\pi} Z {R_0}^2 A^{2/3} \beta (1 + 0.36\beta) \; , \tag{2.14}$$

where $R_0 = 1.2$ fm.

Since the quadrupole moment is very sensitive to deviations from the spherical shape of the nuclear charge distribution, it can be used complementarily to charge radii in determining and interpreting the deformation of nuclei. There is however no general formula linking these two observables. Such a connection is only possible in a model dependent way, e.g. in the single-particle picture the deformation parameter has no meaning and the quadrupole moment for an unpaired nucleon in an orbit with angular momentum $\boldsymbol{j}$ is given by

$$Q_{s.p.} = -\frac{q_j}{e} \, \frac{2j-1}{2(j+1)} \, \langle {r_j}^2 \rangle \; , \tag{2.15}$$

with q_j as the effective charge of the nucleon in this orbit and $\langle {r_j}^2 \rangle$ as its mean square radius. Free neutrons have no charge, and thus don't induce a single-particle quadrupole moment. However, in a nucleus, they interact with the nucleons of the core and can polarize the core, which is reflected by giving the neutrons an effective charge.

Chapter 3

Nuclear information from laser and β-NMR spectroscopy

The present chapter describes in which way the hyperfine structure, isotope shift or nuclear magnetic resonance, available experimentally with laser and β-NMR spectroscopy, are used to measure the nuclear ground state properties, such as charge radii, spins or electromagnetic moments.

3.1 Hyperfine structure

The nuclear multipole moments described in the previous chapter interact with the electromagnetic field produced by the electrons at the site of the nucleus [Bra86]. This interaction leads to a splitting of an atomic level with angular momentum $\boldsymbol{J}$ into a number of components, each of which corresponds to a definite value of the total angular momentum of the atom $\boldsymbol{F} = \boldsymbol{I} + \boldsymbol{J}$. This effect is known as the hyperfine structure, due to its extremely small magnitude compared with the fine structure.

In the central-field approximation of multi-electron systems (like Mg) only electrons outside closed shells contribute to the hyperfine splitting. Electrons in closed shells couple to a "core" of angular momentum $J = 0$, and don't contribute to the multipole interaction. For Mg ions described in this thesis it is thus the single valence electron in the $3s\,^2S_{1/2}$ ground state or in one of the excited $3p\,^2P_{1/2,\,3/2}$ states, which determines the hyperfine structure, and thus gives information on the electric and magnetic moments of the nucleus.

3.1.1 A-factor and the nuclear magnetic moment

The magnetic dipole interaction associated with the nuclear spin represents the interaction of the nuclear magnetic moment μ_I (or rather of its operator $\boldsymbol{\mu_I}$ defined in eqn. 2.4) with the magnetic field B_0 generated by the electrons at the site of the nucleus. It can be described by the Hamiltonian [Bra86]

$$H_m = -\boldsymbol{\mu_I} \cdot \boldsymbol{B}_0 \ , \tag{3.1}$$

which in the first order perturbation theory gives rise to the shift in the electron energies equal [Bra86] to

$$\Delta E_m = \frac{A}{2} K, \tag{3.2}$$

where $K = F(F+1) - J(J+1) - I(I+1)$ and $F = |I - J|, ..., I + J$.

The factor A depends on the value of the magnetic moment and can be expressed as

$$A = \frac{\mu_I B_0}{I\,J} \ , \tag{3.3}$$

In the case of a single s-electron (ground state of Mg^+), whose wave-function does not vanish at the site of the nucleus, A can be written [Kop69] as

$$a_{ns} = \frac{8\pi}{3} hcR_\infty \alpha^2 {a_0}^3 \,(1-\delta)\,(1-\epsilon)\; F_r(j, Z_i)\,|\Psi(0)|^2_{ns}\,\frac{\mu_I}{I\mu_B}, \tag{3.4}$$

where $|\Psi(0)|^2_{ns}$ is the non-relativistic probability density of the s-electron at the nucleus, R_∞ is the Rydberg constant, a_0 is the Bohr radius, μ_B the Bohr magneton and α the fine-structure constant. $F_r(j, Z_i)$ represents a relativistic correction, while δ and ϵ arise due to the finite size of the nucleus.

For electrons with the orbital angular momentum $\ell > 0$ ($\ell = 1$ for both excited states studied in this thesis), A takes a different form [Kop69]:

$$a_{nl} = hcR_\infty \alpha^2 {a_0}^3\, \frac{\ell(\ell+1)}{j(j+1)}\,(1-\delta)\,(1-\epsilon)\,F_r(j, Z_i)\,\langle r^{-3}\rangle_{n\ell}\,\frac{\mu_I}{I\,\mu_B} \ , \tag{3.5}$$

with $\langle r^{-3}\rangle_{n\ell}$ being the non-relativistic radial integral for an electron in such a state.

The relativistic correction F_r depends on the total angular momentum $\boldsymbol{j}$ of the state and on the effective nuclear charge Z_i[1] [Kop69]:

$$F_r(j, Z_i) = \frac{4j(j+1/2)(j+1)}{\sigma(4\sigma^2-1)} \ , \tag{3.6}$$

with $\sigma = \sqrt{(j+1/2)^2 - Z_i^2\alpha^2}$.

The so called Breit-Rosenthal correction δ, which arises from the distribution of the nuclear charge over the whole volume of the nucleus [Ros32], can be expressed [Kop69] as

$$\delta \approx \frac{2(1-\sigma)\sigma(2\sigma+1)}{(2\sigma-1)\Gamma^2(2\sigma+1)}\left(\frac{2Z\,r_0}{a_0}\right)^{2(\sigma-1)} \ , \tag{3.7}$$

with $r_0 = 1.5\ \mathrm{fm}\cdot A^{-1/3}$, where A is the mass number.

On the other hand, the correction ϵ, which is due to the magnetic moment being spread over the nuclear volume, was first pointed out by Bohr and Weisskopf [Boh50], and can be approximated by

$$\epsilon \approx \frac{Z\,r_0}{a_0} \times \left(\frac{a_0}{2Zr_0}\right)^{2(1-\sigma)} \left\langle \frac{r^2}{{r_0}^2} \right\rangle \ , \tag{3.8}$$

with the expectation value for magnetisation distributed uniformly over the nucleus $\langle r^2/{r_0}^2\rangle = 3/5$ [Kop69].

In the case of the $3s\,{}^2S_{1/2}$ state in Mg^+, which is of interest here, the three above corrections have the following values [Kop69]

$$F_r(1/2, 12) = 1.0142 \ , \tag{3.9}$$

$$\delta = 0.006 \ , \tag{3.10}$$

$$\epsilon = 0.0005 \ , \tag{3.11}$$

---

[1] From empirical information $Z_i = Z$ for s states and $Z - 4$ for p electrons.

and with the accuracy of our hyperfine structure measurements in the order of 1 %, the two latter corrections can be neglected.

If the ground state A-factor and the magnetic moment are both known for at least one isotope, one can avoid the direct, but not very accurate, calculations based on eqn. 3.4 or 3.5[2]. In this case, by using the reference isotope and neglecting the ϵ and δ corrections, the expression for an unknown magnetic moment takes a simple form of

$$\mu_I = \frac{A\, I}{A_{ref}\, I_{ref}}\, \mu_{ref}\ . \tag{3.12}$$

In the case of Mg isotopes, ^{25}Mg can serve as such a reference, with the known $A_{3s}=$ 596.254376(54) MHz [Ita81] and $\mu_I = -0.85545(8)\ \mu_N$ [Rag89].

3.1.2 *B*-factor and the electric quadrupole moment

The second important term in the hyperfine splitting is due to the interaction of the nuclear quadrupole moment $\boldsymbol{Q}$ with the gradient of the electric field $\boldsymbol{\nabla E}$ generated by the electrons at the site of the nucleus. Here $\boldsymbol{Q}$ represents the full second-rank tensor operator, of which only the component Q_2^0 was given for defining the quadrupole moment in eqn. 2.11 [Bra86]:

$$H_Q = -\frac{1}{6}\boldsymbol{Q}\cdot\boldsymbol{\nabla E}\ , \tag{3.13}$$

with $\nabla E_{ij} = -\partial^2 V_e/\partial x_i \partial x_j$, where V_e is the electrostatic potential created by the electrons at the nucleus.

This interaction shifts the energy levels [Bra86] by

$$\Delta E_Q = \frac{B}{4}\,\frac{\frac{3}{2}\,K(K+1) - 2\,I\,(I+1)\,J(\,J+1)}{I\,(2I-1)\,J\,(2J-1)}\ , \tag{3.14}$$

with the B-factor depending on Q in a straightforward way:

$$B = eQ\,\langle\frac{\partial V_e}{\partial z^2}\rangle. \tag{3.15}$$

There is no shift for s-states, since their charge distribution is spherically symmetric and thus produces no field gradient. Furthermore, nuclei with $I = 0$ or $1/2$ have no electric quadrupole moment, so ΔE_Q vanishes also in this case.

For a single electron the formula for the average gradient of the electric field produced by the electron at the nucleus takes the form

$$\langle\frac{\partial V_e}{\partial z^2}\rangle = \frac{2j-1}{2j+2}\,\frac{e}{4\pi\varepsilon_0}\,R_r(j, Z_i)\,\langle r^{-3}\rangle_{nl}\ , \tag{3.16}$$

where $R_r(j, Z_i)$ is the relativistic correction depending on j and Z_i. Hence, in order to derive the quadrupole moment from the hyperfine structure, again the radial integral $\langle r^{-3}\rangle_{nl}$ has to be determined.

As in the case of the magnetic dipole interaction, there is another possibility to deduce Q from the hyperfine structure: by measuring the B-factor for an isotope with a known quadrupole moment. This approach yields the simple formula

$$Q = \frac{B_{ref}}{B}\,Q_{ref}\ . \tag{3.17}$$

---

[2] Formula 3.4 will be used in Section 3.2 to derive changes in charge radii from isotope shift measurements.

As the quadrupole moment of ^{25}Mg was measured using transitions in muonic atoms and $Q_{25} = 201(3)$ mbarn [Web82] or 199.4(20) mbarn [Sun91], one can use this method also for Mg isotopes.

3.2 Isotope shift

The change in frequency of an atomic transition between different isotopes of the same element $\nu^{A,A'} = \nu^{A'} - \nu^{A}$ is called the isotope shift [Kin84]. It arises due to the finite mass and extended charge distribution of the nucleus, both of which are felt by the electrons. Hence the total shift can be divided into two parts, the mass and the field shift

$$\delta\nu^{A,A'} = \delta\nu_{MS}^{A,A'} + \delta\nu_{FS}^{A,A'} \ . \tag{3.18}$$

3.2.1 Field shift

The field shift is attributed to the variation, both in volume and shape, of the nuclear charge distribution from one isotope to another. The best probe for this effect are the s-electrons, since their charge density does not vanish at the site of the nucleus. In a relativistic treatment, this is the case also for $p_{1/2}$ states, although with a much smaller magnitude. Other electrons can be regarded as probing the nucleus to a negligible extent.

The field shift can be expressed as a product of the electronic factor F, depending only on the electronic structure of the atomic levels, and the nuclear parameter $\lambda^{A,A'}$ [Kin84], which contains information about the nucleus:

$$\delta\nu_{FS}^{A,A'} = F\,\lambda^{A,A'} \ . \tag{3.19}$$

According to Seltzer [Sel69], $\lambda^{A,A'}$ arises from the changes in even radial moments of the nuclear charge distribution between the involved isotopes

$$\lambda^{A,A'} = \sum_{n} \frac{C_n}{C_1}\,\delta\langle r^{2n}\rangle^{A,A'} = \delta\langle r^2\rangle^{A,A'} + \frac{C_2}{C_1}\,\delta\langle r^4\rangle^{A,A'} + \dots\ . \tag{3.20}$$

For light elements, including Mg, the coefficients C_i/C_1 are very small (around 10^{-4} fm^{-2} and smaller [Sel69]) and within the experimental accuracy one can assume that

$$\delta\nu_{FS}^{A,A'} = F\,\delta\langle r^2\rangle^{A,A'} \ , \tag{3.21}$$

where $\delta\langle r^2\rangle^{A,A'}$ is the change in the mean square charge radius, as defined in Chapter 2.

In first order perturbation theory the electronic factor [Kin84] is given by

$$F = \frac{2\pi}{3}\,Z\,e^2\,\Delta|\Psi(0)|^2_{rel} = \pi\,\frac{{a_0}^3}{Z}\,f(Z)\,\Delta|\Psi(0)|^2 \tag{3.22}$$

Here $\Delta|\Psi(0)|^2_{rel}$ is the change in the relativistic electron density at the nucleus due to the transition, $\Delta|\Psi(0)|^2$ is the change in the corresponding non-relativistic density, whereas the factor $f(Z)$ includes the details of the Dirac wave function calculated for an extended nucleus and normalised to $|\Psi(0)|^2/Z$ [Hei74], [Ahm88].

For $ns \rightarrow np$ transitions in alkali-like systems, such as Mg$^+$, $\Delta|\Psi(0)|^2$ can be assumed to depend only on the charge density of the ns state [Hei74], hence

$$\Delta|\Psi(0)|^2 \approx \beta\,|\Psi(0)|^2_{ns} \ , \tag{3.23}$$

where β is the screening factor, which takes into account the change in the screening of the core electrons when the valence electron is excited. In this way the final expression for the electronic factor of Mg$^+$ in the transitions $^2S_{1/2} \rightarrow {}^2P_{1/2,3/2}$ becomes

$$F = \pi \, \frac{{a_0}^3}{12} \, f(12) \, \beta \, |\Psi(0)|^2_{3s} \, , \tag{3.24}$$

with $f(12)$ [Blu85] and β [Tor85] equal to

$$f(12) = -240 \text{ MHz/fm}^2 \, , \tag{3.25}$$

$$\beta = 1.097 \, . \tag{3.26}$$

Determination of $|\Psi(0)|^2$ and F

In order to find the electronic factor for Mg$^+$ ions, the density of the $3s$ electron at the nucleus has to be known. The way to find it is either by *ab initio* calculations, or by one of two established empirical methods based on (i) the Goudsmit-Fermi-Segré (GFS) formula for the ns energy levels, or on (ii) the magnetic hyperfine splitting for a nucleus with a known spin and magnetic dipole moment.

(i) According to the GFS formula [Kop69], $|\Psi(0)|^2$ can be obtained from

$$|\Psi(0)|^2_{ns} = \frac{Z_i \, Z_a}{\pi \, {a_0}^3 \, {n_a}^3} \, (1 - \frac{d\Delta}{dn}) \, , \tag{3.27}$$

where Z_a is the so called spectrum number (1 for neutral atoms, 2 for single ions), n_a is the effective quantum number and $\Delta = n - n_a$ is the quantum defect. The value of n_a can be derived from the level energies E_{ns} with respect to the ionisation limit via [Kop69]:

$$n_a = \sqrt{R_\infty / |E_{ns}|} \, , \tag{3.28}$$

and the dependence of Δ on the principal quantum number n can be presented [Kop69] as

$$d\Delta/dn = \frac{d\Delta/d_{ns}}{d\Delta/dE_{ns} - n_a/(2E_{ns})} . \tag{3.29}$$

For Mg$^+$ this was determined by a second order polynomial fit of $\Delta(E_{ns})$ to the available data for n = 3-10, which gives

$$n_a = 1.9026 \, , \tag{3.30}$$

$$d\Delta/dE_{ns} = 0.0285 \, , \tag{3.31}$$

$$d\Delta/dn = -0.0342 \, . \tag{3.32}$$

Using the above values and eqn. 3.27, the non-relativistic $3s$-electron density in the Mg$^+$ ground state becomes

$$|\Psi(0)|^2_{GFS} = 2.295 \; a_0^{-3} \, , \tag{3.33}$$

based on which the electronic factor is calculated to be

$$F_{GFS} = -158 \text{ MHz/fm}^2 \, . \tag{3.34}$$

(ii) The other semi-empirical approach to $|\Psi(0)|^2$ is based on the formula for the hyperfine structure constant (eqn. 3.4), which for this purpose can be written as

$$|\Psi(0)|^2_{ns} = \frac{3 \, a_{ns} \, \mu_B I}{8\pi hc \, R_\infty {a_0}^3 \, \alpha^2 \, F_r(j, Z_i) \, \mu_I} \, . \tag{3.35}$$

This equation can be used for ^{25}Mg, since for this isotope (as mentioned in the context of Section 3.1) A and μ_I have been measured with high precision. Inserting these quantities in eqn. 3.35 gives

$$|\Psi(0)|^2_{HFS} = 2.150 \; a_0^{-3} \; , \tag{3.36}$$

$$F_{HFS} = -148 \text{ MHz/fm}^2 \; . \tag{3.37}$$

Both semi-empirical approaches are limited by the uncertainty in the screening factors and are only approximate themselves, with an accuracy usually assumed to be about 10 %. Therefore their agreement within 7 % is acceptable and for further applications their arithmetical average with an error corresponding to their deviation from this average will be used:

$$F_{se} = -153(5) \text{ MHz/fm}^2 \; . \tag{3.38}$$

For Mg isotopes also two *ab initio* calculations exist, which use the Dirac-Fock (DF) [Tor85] and the relativistic Hartree-Fock approach (HF) [Ber03], from which

$$F_{DF} = -117 \text{ MHz/fm}^2 \; , \tag{3.39}$$

$$F_{HF} = -127 \text{ MHz/fm}^2 \; . \tag{3.40}$$

Since the uncertainly in these values reaches also several percent, the quantity used further will be the arithmetic average with the error determined in the same way as in the semi-empirical approach:

$$F_{ai} = -122(5) \text{ MHz/fm}^2 \; . \tag{3.41}$$

The 20 % difference in F_{se} and F_{ai} follows the usual trend of semi-empirical and *ab initio* values of the electronic factors [Mue83], [Tor85], [Mar92]. There is no clear understanding what are the reasons for this discrepancy, nor which approach gives correct values. The *ab initio* calculations might underestimate F due to insufficient account for far configuration mixing effects, whereas the semi-empirical approach can suffer from overestimation due to large uncertainties for spin-exchange core polarisation [Kin86]. From previous measurements on other isotope chains [Mue83], [Ahm88] it turns out that usually a more consistent nuclear physics interpretation is reached when using the semi-empirical values.

3.2.2 Mass shift

The mass shift $\delta\nu^{A,A'}_{MS}$ arises from the motion of the nucleus and the electrons around their common centre of mass. It can be further split into the normal (NMS) and specific shift (SMS). The first part takes into account the reduced mass of the nucleus and an electron, whereas the latter involves correlations in the motion of electrons [Woo80], [Kin84]. In general, the mass shift is hence presented [Kin84] as

$$\delta\nu^{A,A'}_{MS} = K_{MS} \, (\frac{1}{m_{A'}} - \frac{1}{m_A}) = K_{MS} \, \frac{m_A - m_{A'}}{m_A \, m_{A'}} \; , \tag{3.42}$$

with $K_{MS} = K_{NMS} + K_{SMS}$. Here m_A and $m_{A'}$ are the masses of the two isotopes, while K_{NMS} and K_{SMS} are the isotope-independent mass shift constants. Because of the proportionality to $1/m^2$ of both mass terms, $\delta\nu^{A,A'}_{MS}$ is small in heavy elements, but dominant in the Mg mass region and in lighter atoms.

K_{NMS} can be derived in a straightforward way from the transition frequency ν_0 and the electron mass m_e:

$$K_{NMS} = -\nu_0\, m_e\ , \tag{3.43}$$

and for Mg ion transitions $^2S_{1/2} \rightarrow {}^2P_{1/2,\,3/2}$ this gives

$$K_{NMS}[^2S_{1/2} \rightarrow {}^2P_{1/2}] = -586.6 \text{ GHz u}\ , \tag{3.44}$$

$$K_{NMS}[^2S_{1/2} \rightarrow {}^2P_{3/2}] = -588.1 \text{ GHz u}\ . \tag{3.45}$$

K_{SMS}, on the other hand, is very difficult to calculate and has to be derived using *ab initio* calculations. These are available for both transitions [Ber03], however with errors too large for our purposes, as shown below:

$$K_{SMS}[^2S_{1/2} \rightarrow {}^2P_{1/2}] = -373(12) \text{ GHz u}\ , \tag{3.46}$$

$$K_{SMS}[^2S_{1/2} \rightarrow {}^2P_{3/2}] = -373(6) \text{ GHz u}\ . \tag{3.47}$$

3.2.3 Determination of $\delta\langle r^2\rangle$

If precise theoretical predictions exist for both F and K_{SMS}, the way to determine the difference in charge radii based on the isotope shift studies is quite straightforward: one needs to use the measured isotope shift together with equations 3.18, 3.21, and 3.42. If, however, such calculations do not exist, or their errors are too large, as is the case for Mg isotopes where the uncertainty in the mass shift is as large as the expected field shift of about 20-30 MHz, another approach has to be taken. It is based on at least three known charge radii, measured with other techniques such as electron scattering or transitions in muonic atoms [Kin84].

Charge radii of all three stable Mg isotopes have been determined by studying X-ray transitions in muonic atoms [Fri95], thus they can be used with the corresponding isotope shifts for the determination of $\delta\langle r^2\rangle^{24,A'}$ for radioactive isotopes for which the isotope shift is measured. One starts with the isotope shift formula, in which for Mg A=24 and A'=25 or 26:

$$\delta\nu_{IS}^{24,A'} = K_{MS}\, \frac{m_{24} - m_{A'}}{m_{24}\, m_{A'}} + F\, \delta\langle r^2\rangle^{24,A'}\ , \tag{3.48}$$

and converts it into an expression showing a linear dependence between $\delta\nu^{24,A'}$ and $\delta\langle r^2\rangle^{24,A'}$, both modified by the mass factor $m_{24}\, m_{A'}/(m_{24} - m_{A'})$

$$\delta\nu^{24,A'}\, \frac{m_{24}\, m_{A'}}{m_{24} - m_{A'}} = K_{MS} + F\, \delta\langle r^2\rangle^{24,A'}\, \frac{m_{24}\, m_{A'}}{m_{24} - m_{A'}}\ . \tag{3.49}$$

This is a special form the so called King plot [Kin84]. By fitting eqn. 3.49 to points corresponding to the data for $^{25-24}$Mg and $^{26-24}$Mg, one can determine K_{MS} and F, as well as extrapolate $\delta\langle r^2\rangle^{24,A'}$ to other isotopes. In order to properly evaluate the fit and extrapolation errors, a detailed treatment of uncertainties in charge radii from muonic atom transitions is necessary, as presented below.

Charge radii from muonic atoms

Transitions in muonic atoms can be used to determine absolute nuclear charge radii, and not only their differences. This is due to the large mass of a muon, which allows one to nearly ignore the influence of atomic electrons and to treat muonic atoms as hydrogen-like systems, where comparison with very accurate atomic theory is possible.

R.C. Barrett [Bar70] showed that the energies of muon transitions measured in the experiment are best interpreted in terms of the generalised moments $\langle r^k\, e^{-\alpha\, r}\rangle$ of the nuclear charge distribution, where k and α are smoothly varying functions of Z for a transition between given muonic levels, and α is almost the same for all transitions in a particular element. Such moments are almost independent of assumptions made about the actual shape of the nuclear charge distribution and therefore are described as "model-independent". Because of this property, muonic results are usually expressed in terms of the so called Barrett radius $R_{k\alpha}$. This quantity represents a model-independent radius of a nucleus with uniform charge density, having the same moment $\langle r^k\, e^{-\alpha\, r}\rangle$ as the actual nucleus [Kin84], [Fri95]. It is defined by

$$3R_{k\alpha}^{-3}\int_0^{R_{k\alpha}} r^k e^{-\alpha r} r^2 dr = \langle r^k e^{-\alpha r}\rangle\ . \tag{3.50}$$

However, the quantity derived from isotope shifts in atomic transitions is the change in the mean square radii, not in the Barrett radii. In order to derive $\delta\langle r^2\rangle$ from muonic atoms, one has to assume a given charge distribution and to derive $\langle r^2\rangle$ based on this distribution. For light nuclei, on the assumption of a Fermi distribution (eqn. 2.2), $k \approx 2$ and $\alpha \approx 0$, so $\langle r^2\rangle$ is very close to the generalised moment $\langle r^k\, e^{-\alpha\, r}\rangle$.

Uncertainties in determining nuclear charge radii from muonic transitions have several sources. The first arises from the statistical error of the $2p$-$1s$ muonic transition energy. The second is due to the uncertainty in the nuclear polarisation correction and it corresponds to 30 % of the total nuclear polarisation value [Fri95]. The third source of uncertainty is another systematic effect due to the choice of the skin thickness t of the Fermi distribution (eqn. 2.2). Fricke *et.al* [Fri95] recommend to vary t by ±10 % for the evaluation of this error. The charge radii and their uncertainties, as well as Barrett radii used for their derivation, are presented in Table 3.1.

Table 3.1: Nuclear charge radii and their uncertainties (in fm) of stable Mg isotopes, derived from muonic atom experiments. Data from [Fri95].

A	$R_{k\alpha}$	σ_{stat}	σ_{syst1}	$\langle r^2\rangle^{1/2}$	σ_{stat}	σ_{syst1}	σ_{syst2}
24	3.9291	0.0005	0.0030	3.0570	0.0004	0.0023	0.0700
25	3.8924	0.0008	0.0025	3.0290	0.0006	0.0019	0.0700
26	3.8992	0.0008	0.0026	3.0340	0.0006	0.0020	0.0700

The differences in charge radii and their uncertainties based on the above values are summarised in Table 3.2. For $\delta\langle r^2\rangle$, the main contribution to the error comes from the systematic uncertainty in the nuclear polarisation corrections, which was taken to be 10 % of the larger of the nuclear polarisation values for the two isotopes [Fri95]. Next comes the statistical error arising from the uncertainty in the transition energy. This error is comparable to systematic uncertainties due to the skin thickness t, which were calculated assuming the same value of t for all three Mg isotopes.

The above values will be used for the empirical derivation of K_{MS} and F in Chapter 5.

Table 3.2: Differences in charge radii (in fm) and their uncertainties (in fm and %) for stable Mg isotopes, derived from muonic atom experiments. Based on [Fri95].

A,A'	$\delta\langle r^2\rangle^{A,A'}$	σ_{stat}	σ_{syst1}	σ_{syst2}	$\sigma^{rel}_{syst1}(\%)$	$\sigma^{rel}_{syst2}(\%)$
25,24	-0.1704	0.0045	0.017	0.0051	10%	3%
26,24	-0.1401	0.0045	0.014	0.0042	10%	3%

3.3 Nuclear magnetic resonance

The principle of nuclear magnetic resonance (NMR) is the interaction of electromagnetic radiation with nuclei having a non-zero magnetic moment and placed in external magnetic field. It can be explained both by classical, as well as by the quantum theory. In this chapter the latter approach will be followed.

3.3.1 NMR and the nuclear electromagnetic moments

Nuclear magnetic resonance is described by the same Hamiltonian as the magnetic hyperfine structure (eqn. 3.1). In this case, however, the source of the magnetic field are not the atomic electrons, but an external magnetic field [Abr61], [Sch90].

For a static magnetic field B_0 directed along the z-direction, this Hamiltonian becomes [Abr61]

$$H_0 = -\boldsymbol{\mu_I} \cdot \boldsymbol{B_0} = -g_I\,\mu_N \boldsymbol{I} \cdot \boldsymbol{B_0} = -g_I \mu_N I_z B_0 \; , \tag{3.51}$$

which causes the nuclear state with spin I to split into $2I+1$ sub-levels with $I_z = m_I = -I, ..., I-1, I$, known as the Zeeman effect. In absence of other fields, the previously degenerate m_I states are shifted by the magnetic energy proportional to the g-factor of the nucleus [Abr61]:

$$\Delta E(m_I) = -m_I g_I \mu_N B_0 = -m_I \hbar\omega_L \; , \tag{3.52}$$

where ω_L is the Larmor frequency and $\omega_L = 2\pi\nu_L$.

On the other hand, a time-dependent perturbing Hamiltonian due to an oscillating field $\boldsymbol{B}_1$, directed for example along the x-axis, can be presented [Abr61] as

$$H_1 = -\boldsymbol{\mu_I} \cdot \boldsymbol{B_1} = -g_I \mu_N \boldsymbol{I} \cdot \boldsymbol{B_1} = -g_I \mu_N I_x B_1 \cos(\omega_1 t) \; , \tag{3.53}$$

with B_1 being the amplitude of the field and ω_1 – the oscillation frequency. H_1 is responsible for transitions between different m_I sub-levels. It has matrix elements different from 0 only when $m'_I = m_I \pm 1$.

In the β-NMR method used in our experiments and described in more detail in Chapter 4, the occupations of m_I sub-levels are determined by the optical pumping process. Hence, irradiation with electromagnetic waves perpendicular to $\boldsymbol{B}_0$ of frequency $\nu = \nu_L$ causes resonant absorption or emission, leading to equalisation of population. Such a resonance is observed as the loss of the β-decay asymmetry created by the optical pumping process. It reveals the Larmor frequency of the nuclear spin system, and thus allows to determine the nuclear g-factor

$$|g_I| = \frac{\nu_L\, h}{\mu_N\, B_0} \; . \tag{3.54}$$

If the spin of the nucleus is known, also its magnetic moment can be derived in this way, as presented by eqn. 2.6.

In order to calibrate the magnetic field, an NMR measurement can be performed on a different nucleus with a known g-factor, yielding:

$$|g_I| = |g_{ref}| \frac{\nu}{\nu_{ref}} \; . \tag{3.55}$$

If the reference is an isotope of a different chemical element, one has to include the diamagnetic corrections $1/(1-\sigma)$ [Rag89] due to different shielding of the external magnetic field by the electrons, which is to a good approximation identical for isotopes of one element:

$$|g_I| = |g_{ref}| \frac{\nu}{\nu_{ref}} \frac{1 + 1/(1-\sigma)}{1 + 1/(1-\sigma_{ref})} \; , \tag{3.56}$$

where σ is the magnetic shielding factor. For the measurements described in this thesis there was no radioactive Mg isotope of known magnetic moment, which could be used for callibration with the β-NMR technique. Therefore ^{8}Li was chosen as a reference, since it is produced in the same ISOLDE target and requires minor modifications of the setup.

If the nucleus possesses a quadrupole moment, and if one superimposes the magnetic field with an electric field gradient $V_{zz} = \partial^2 V_e / \partial z^2$, the energy level shifts given in eqn. 3.52 are modified by the quadrupole interaction. In the case of an axially symmetric field gradient parallel to the static magnetic field the additional shift takes the form [Kop69]

$$\Delta E(m_I) = \frac{e\,Q\,V_{zz}}{4I(2I-1)} \left(3m_I^2 - I(I+1)\right) \; . \tag{3.57}$$

Gradients strong enough to cause a measurable effect are provided by non-cubic crystal lattices, in which the NMR spectrum for transitions between the $2I+1$ Zeeman levels shows $2I$ different resonance peaks. The distance between neighbouring peaks $\Delta\nu_L$ is constant and it is related to the nuclear quadrupole moment by

$$Q = \Delta\nu_L h \frac{4I}{3e\,V_{zz}} \; . \tag{3.58}$$

If the quadrupole moment of at least one isotope of the same chemical element is known, a reference measurement can be performed, which yields

$$Q = Q_{ref} \frac{\Delta\nu I}{\Delta\nu_{ref} I_{ref}} \; . \tag{3.59}$$

Otherwise one has to rely on the theoretical values of V_{zz}, as is the case for Mg, since no quadrupole moment is known of any radioactive Mg isotope which could be studied with β-NMR.

3.4 Hyperfine splitting combined with NMR results: I and μ_I

In some cases, the hyperfine structure of a nucleus with an unknown spin and magnetic moment cannot provide the A-factor and the spin independently. Such a situation can take place if resonances overlap or not all of them are visible, because they are too weak for the measuring statistics. At the same time, the nuclear magnetic resonance can only yield the absolute value of the g-factor, but no spin. However, if one combines information from both methods, I and the value and sign of μ_I can be determined in an unambiguous way [Arn87], [Gei99]. This can be shown in the formula for the hyperfine splitting (eqn. 3.2). For two transitions from different ground-state sub-levels F and F' to the same excited-state sub-level, in absence of the quadrupole interaction the splitting between them equals to (see eqn. 3.2)

$$\Delta E_{F,F'} = \frac{A}{2}\left(F(F+1) - F'(F'+1)\right) , \tag{3.60}$$

When $F' = F - 1$, the above expression simplifies to

$$\Delta E_{F,F'} = AF . \tag{3.61}$$

If the hyperfine constant A is not known, one can use a measurement on a reference isotope with known A_{ref}. Using eqn. 3.3 this leads to

$$\Delta E_{F,F'} = A_{ref}\frac{g_I}{g_{ref}}(I + 1/2) . \tag{3.62}$$

As mentioned above, the absolute value of g_I is known from the NMR studies (eqn. 3.55 and 3.56), thus by using it in eqn. 3.62, the unknown spin and magnetic moment can be unambiguously determined. For Mg^+ and $J = 1/2$ this gives

$$I = \frac{|\Delta E|}{|g_I|}\frac{g_{ref}}{A_{ref}} - 1/2 , \tag{3.63}$$

and

$$|\mu_I| = |g_I|\, I . \tag{3.64}$$

Based on the position of different hyperfine resonances, as well as on their relative amplitudes connected via Clebsch-Gordan coefficients, one can also determine the sign of the A-factor and thus the sign of both the g-factor and the magnetic moment.

Chapter 4

Experimental techniques

4.1 Collinear laser spectroscopy

Collinear laser spectroscopy is a unique tool for high-resolution studies of optical transitions in ions or neutral atoms, which is particularly suitable for the investigation of radioactive species. It gives insight into the ground state properties of a variety of nuclei, from their hyperfine structure and isotope shifts, as discussed in Chapter 3. The basic idea is the geometrical superposition of a fast ion beam or atomic beam with a laser beam and the detection of optical resonances.

This collinear configuration offers several advantages. The primary one is a narrow Doppler width, prerequisite of high resolution and sensitivity. It comes from the acceleration in an electrostatic field[1], in which the spread of kinetic energy of the ions remains constant, but the difference in their velocity decreases [Kau76]. This effect can be illustrated by the formula

$$\delta E = \delta(\frac{1}{2}mv^2) = mv\,\delta v = \text{const}\ , \tag{4.1}$$

with the ion mass m, and the energy and velocity spreads δE and δv which are both connected to the initial temperature of the ions and the stability of the acceleration voltage.

The Doppler broadening $\delta\nu_D$ of an atomic transition is related to the underlying velocity spread δv by the simple formula $\delta\nu_D = \nu\,\delta v/c$, where ν is the transition frequency. Therefore, the Doppler width after acceleration by an electrostatic potential difference U can be expressed as

$$\delta\nu_D = \frac{\nu\,\delta E}{\sqrt{2eUmc^2}}\ , \tag{4.2}$$

where e is the charge of the ion.

As can be seen from this formula, the Doppler width is proportional to $1/\sqrt{U}$. Thus, with increasing potential difference and increasing ion velocity, $\delta\nu_D$ decreases, and so does the total line width, which is dominated by it. In our experiments $\delta E \approx 1.5$ eV and $U = 60$ kV. For Mg isotopes with masses around 25 atomic units (u) and a transition wavelength of 280 nm, this means a reduction of the Doppler broadening from several GHz to about 30 MHz, which is comparable to the natural linewidth of the two investigated transitions equal to 41 MHz and corresponding to the lifetime around 3.8 ns [Ans89].

An additional useful feature of the collinear method is the possibility to tune the laser frequency across optical resonances by modifying the beam velocity. Depending of their

---

[1] Such acceleration is possible only for ions. Hence, even when studying atoms one starts with ions, accelerates them and only later neutralizes.

velocity, due to the Doppler effect, the ions "see" a laser frequency ν_0 related to the frequency in the laboratory frame ν_{las}. For collinear propagation of the two beams, the shift can be expressed by the relativistic formula

$$\nu_{las} = \nu_0 \frac{1+\beta}{\sqrt{1-\beta^2}} \approx \nu_0(1+\beta) \; , \tag{4.3}$$

with $\beta = v/c$ derived from the relativistic energy expression:

$$\beta = \sqrt{1-(1+eU/mc^2)^{-1}} \approx \sqrt{2eU/mc^2} \; . \tag{4.4}$$

In the case of measurements described in this thesis $v \approx 0.002\,c$. At this velocity the Doppler shift of the 280-nm excitation is around 2400 GHz. For isotope shift measurements on isotopes with $\Delta A = 3$ the shift would be as large as 40 GHz, which corresponds to 6.5 kV in the Doppler tuning voltage. Changing the voltage at a constant laser frequency facilitates very much the experimental conditions of on-line running.

4.2 Optical pumping and nuclear polarisation

Detection of atomic and nuclear resonances via β-decay asymmetry requires an ensemble of short-lived nuclei which are polarised, i.e. the expectation value of the projection m of their spins is different from zero. In general, the polarisation of an ensemble of particles (atoms, nuclei, etc.) with angular momentum J can be defined as

$$P_J = \frac{\langle J_z \rangle}{J} = \frac{\sum_{m=-J}^{J} m\, N_m}{J \sum_{m=-J}^{J} N_m} \; , \tag{4.5}$$

where N_m is the occupation of a given magnetic sub-state m.

Nuclear spin polarisation can be obtained by several methods: capture of polarised thermal neutrons, nuclear reactions with selected recoil angle, reactions with polarised particles, or by interaction with circularly polarised laser light.

The latter method, known as optical pumping, is applied in our experiments [Kei00], since it is suitable to be used for low-energy beams with a small energy spread, which are available at the ISOLDE facility at CERN. Furthermore, it allows to obtain high degrees of polarisation (in some cases up to 50 %) and gives the possibility not only to study nuclear magnetic resonance, but also to use the β-decay asymmetry for a sensitive detection of the hyperfine structure and isotope shifts. However, it is not a universal method, but it depends to a large extend on the order and nature of atomic energy levels. Branched decays and decays into “dark states”, from which no repumping is possible, pose the largest constrains on effective pumping. In some cases, such as the noble gases, the transition energy may also be a limiting factor.

With this technique, one obtains first the polarisation of atoms/ions as a whole, i.e. $\langle m_F \rangle / F \neq 0$, by their resonant interaction with circularly polarised laser light. In our experiment the electron and nuclear spins are decoupled in a strong magnetic field before the nuclear spin polarised atoms/ions are implanted into a host crystal lattice.

The principle of optical pumping is straightforward. The atoms/ions are irradiated by circularly polarised laser light, which causes transitions between the m_F magnetic sub-states

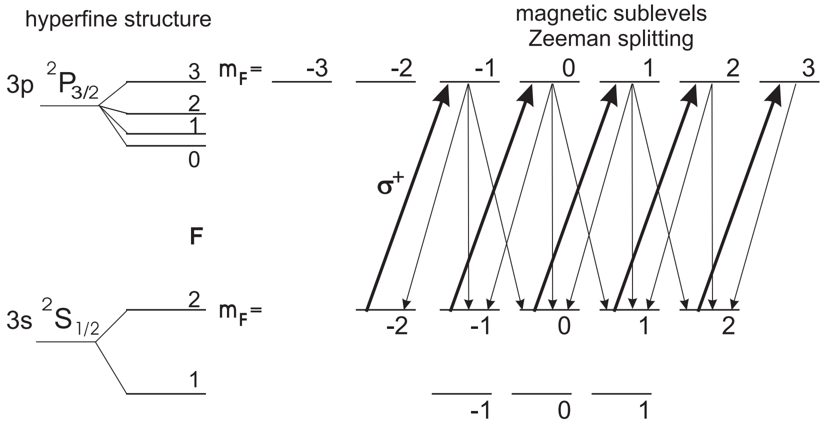

Figure 4.1: Optical pumping with σ^+ light for the D_2 line of $^{29}\mathrm{Mg}^+$ ($I = 3/2$, $\mu_I > 0$).

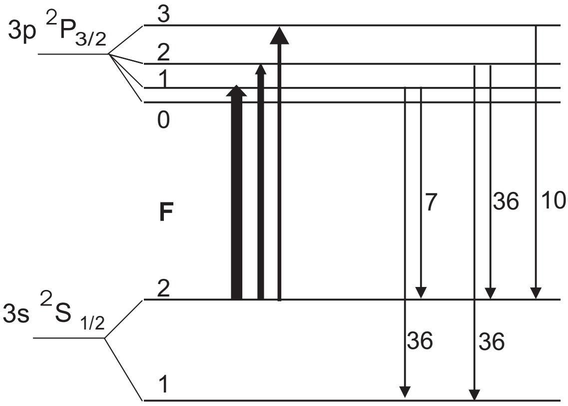

Figure 4.2: Hyperfine pumping in the D_2 line of $^{29}\mathrm{Mg}^+$ for a resonant $F = 2$ to $F' = 1$ transition. The thickness of the arrows represents schematically the population of the $^2P_{3/2}$ sublevels after the excitation: also neighbouring levels $F' = 2$ and $F' = 3$ are populated. The relative strengths [Kop69] of the spontaneous decay are indicated as well.

(Zeeman sublevels) of the hyperfine structure. For Mg, optical polarisation is readily achieved for a singly charged ion in the transitions from the ground state, $3s\,^2S_{1/2}$, to one of the first excited states, $3p\ ^2P_{1/2}$ or $3p\ ^2P_{3/2}$ (D_1 or D_2 line), both of which lie in the UV region around 280 nm ($\lambda^{-1} = 35669.32$ cm^{-1} for D_1 [Ris55] and 35760.83 cm^{-1} for D_2 line [Ita81]). The process is schematically shown in Fig. 4.1 for $^{29}\mathrm{Mg}^+$: σ^+ polarised light (σ^+) induces atomic transitions with $\Delta m_F = +1$ (for σ^-, $\Delta m_F = -1$). Although the decay is isotropic with $\Delta m_F = -1, 0$ or $+1$, the laser light interacts many times with the same atom and causes excitations in which m_F can only increase by 1 (decreases by 1 for σ^-). As a result, most of Mg ions are in the ground state substate with the highest m_F (for σ^+, or lowest m_F for σ^-). A complication to this quite straightforward process is caused by the hyperfine pumping (Fig. 4.2), in which the excited state decays to the other ground state level ($F = 1$ in Figs. 4.1 and 4.2). This lowers the population of the ground state component available for optical pumping and therefore limits the polarisation to less than 100 % [Kei00]. For example, the polarisation for spin 1/2 can reach 80 %, but for $I = 3/2$ equals around 40 %, and is even lower for spin 5/2 or 7/2. Results of optical-pumping simulations for Mg isotopes are presented in Section 5.3.2.

For the detection of polarisation by an asymmetry in the nuclear β-decay, the atoms/ions have to be confined in space, which is possible by implanting them into a host crystal. Because

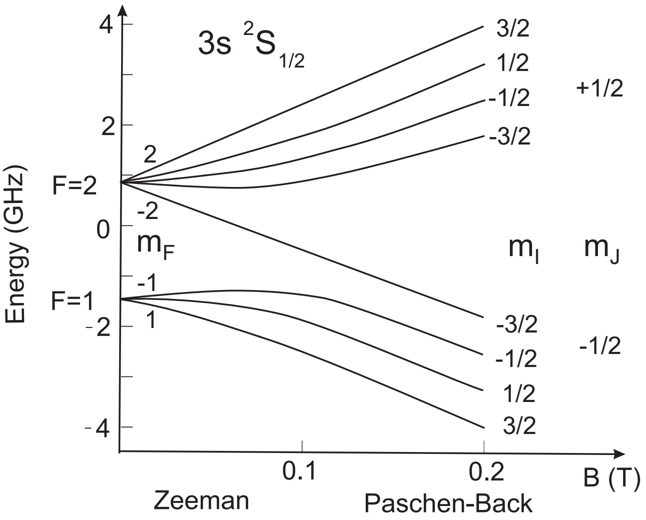

Figure 4.3: Behaviour of the ground state hyperfine structure of ^{29}Mg for weak and strong magnetic field ($I = 3/2$, $\mu_I > 0$).

electron spins loose their orientation very quickly due to interactions with the electrons of the crystal lattice, whereas the nuclear spin-relaxation is much slower (see Section 4.3.2), only a nuclear polarisation will remain. The observed nuclear polarisation $\langle m_I \rangle / I$ is reached after the adiabatic decoupling of the spins in gradually increasing static magnetic field in front of the stopping crystal.

The decoupling of spins and the energy shift of levels due to an increasing magnetic field are shown in Fig. 4.3, on the example of ^{29}Mg. This figure is based on the Breit-Rabi formula [Bra86] describing the energy levels for a system with $J = 1/2$ in the transition from the Zeeman regime (quantum numbers (F,m_F)) to the Paschen-Back regime (quantum numbers (m_J,m_I)).

4.3 Detection methods

In order to determine the nuclear ground state properties from atomic spectra, as described in Sections 3.1 and 3.2, the atomic resonances have to be detected. This is usually achieved by fluorescence detection, which is based on counting the photons emitted by the ions/atoms excited by the laser light. For short-lived β-emitting nuclei, however, one can use the asymmetry of their β-decay, which also offers the possibility to perform NMR measurements, yielding the electromagnetic moments of the nuclei (see Section 3.3).

The following section will discuss both techniques, their applicability and limits, including the influence of the bunched beam structure of radioactive isotopes delivered by ISOLDE.

4.3.1 Fluorescence detection

In classical collinear laser spectroscopy the detection of atomic resonances is performed by recording the fluorescence induced by laser light, which is the most straightforward method applicable for both stable and radioactive isotopes. However, this technique is not suitable for nuclei with very low production rates, due to the limited efficiency of detecting visible or

UV photons, as well as due to an unavoidable background coming mainly from the scattered laser light.

The fluorescence detection is not influenced very much by the pulsed nature of the protons underlying the production of radioactive nuclei which is described in more detail in Section 4.4.1. Due to chemical processes inside the production target, the radioactive beams have a semi-continuous structure. The possible pulse effects are averaged out by summing scans which start independently of the arrival of the proton pulse. In one scan the full hyperfine structure (if present) is recorded. The scan consists of 100 (for isotopes with no hyperfine splitting) to 500 (for isotopes with hyperfine splitting) channels, in each of which the photon counts are recorded during 10 ms. One full scan takes hence 1-5 s. A measurement consists usually of several to several hundred scans, depending on the yield of the studied isotope.

The minimum acceptable yield can be roughly evaluated based on the counts collected in one channel. The signal-to-noise ratio S/N is in principle limited by the noise of the incident radiation [Dem03], and can be thus expressed by

$$S/N = \frac{S}{\sqrt{B}} = \frac{\epsilon\, at}{\sqrt{b\, t}} = \frac{\epsilon\, a}{\sqrt{b}}\sqrt{t}\;. \tag{4.6}$$

Here B denotes the total background recorded during a measurement in one channel and b the background rate (per second), which are assumed to be purely statistical. The total efficiency of detecting a photon for each radioactive ion reaching the experimental setup is represented by ϵ. It takes into account the transmission into the detection setup, the solid angle covered by the light collection system, the detector efficiency, as well as other possible losses. Finally, a is the number of atoms reaching the setup per second, while t is the total detection time in one channel. As seen from the above formula, the signal-to-noise ratio increases proportionally to $\sqrt{t}$, thus e.g. a 10-fold increase in S/N requires a 100 times longer total measuring time.

In order to distinguish a signal from the noise, the usual condition is that S should be at least three times larger than N. This leads to the minimum required production yield (in atoms/s)

$$a_{min} = \frac{3\sqrt{b}}{\epsilon\sqrt{t}}\;. \tag{4.7}$$

The usual on-line conditions give background of $b = 3\,000$ counts/s for 1 mW laser power. For isotopes with spin zero and no hyperfine splitting, like ^{24}Mg and ^{26}Mg, the total detection efficiency is in the range of $\epsilon = 1 : 20\,000$. If one would like to see a resonance within one hour with 100 channels per scan, this means $t = 36$ s of data-collection in one channel. By inserting the above values into eqn. 4.7, one obtains the minimum yield equal to 5×10^5 atoms/s. In the case of isotopes with the hyperfine structure, such as ^{25}Mg, the detection efficiency is 5-10 times lower, due to hyperfine pumping. Since one scan on such nuclei consists of about 500 channels, this gives $t = 7.2$ s for one channel, if the resonance should be visible after 1 hour. With these values the minimum required yield is 5-10 $\times 10^6$ atoms/s.

4.3.2 β-decay asymmetry

For β-decaying isotopes with half-lives in the range of several milliseconds to several seconds, a suitable way of observing atomic and nuclear resonances is achieved via the detection of β-decay asymmetry of the nuclear ensemble stopped. In contrast to fluorescence spectroscopy, which is based on the beam passing in front of the photomultipliers, this method requires the nuclear ensemble to be implanted in a host crystal, where β particles originating from the radioactive decay of the ensemble are detected.

This approach relies on the parity non-conservation of the weak interaction which causes the anisotropic emission of β-particles by an ensemble of nuclei with polarised spins. If the polarisation is achieved with optical pumping (see previous section), the atomic resonances can be seen as an appearance of decay asymmetry. On the other hand, an NMR signal can be obtained, if the asymmetry created by the laser light is destroyed by a tunable radio-field at the nuclear Larmor frequency applied around the stopping lattice.

Distribution of radiation from an oriented nuclear state

In general, the angular distribution of any radiation (e.g. γ or β) emitted from an oriented ensemble of spin I is given [Kra86] by

$$W(\boldsymbol{k}_\Omega) = \sqrt{2I+1} \sum_{\lambda,q,q'} \rho_q^{\lambda *} A_{\lambda,q'} D^\lambda_{q,q'} \ . \tag{4.8}$$

W describes the probability of observing the radiation in the direction $\boldsymbol{k}_\Omega$ with respect to solid angle Ω. The angular distribution coefficients $A_{\lambda,q'}$ represent the properties of the involved nuclear states and $D^\lambda_{q,q'}$ transforms the quantization axis of the spin ensemble into the coordinate system specified by $\boldsymbol{k}$. The irreducible spherical tensors ρ_q^λ describe the orientation of the nuclear state emitting the detected radiation, and they can be related to the elements of the density matrix $\rho_{mm'}$ of the ensemble by the following formula [Kra86]

$$\rho_q^\lambda = \sqrt{2I+1} \sum_m (-1)^{I+m'} \begin{pmatrix} I & I & \lambda \\ -m' & m & q \end{pmatrix} \rho_{mm'} \ . \tag{4.9}$$

Even values of λ mean alignment, whereas odd values of λ correspond to polarisation.

If the oriented state is axially symmetric, with the symmetry given for example by a static magnetic field, only components with $q = 0$ are non-vanishing and the D-function can be reduced to the spherical harmonics, from which the resulting directional distribution of the radiation becomes [Kra86], [Mat71]

$$W(\theta) = \sqrt{2I+1} \sum_\lambda \rho_0^\lambda A_\lambda P_\lambda(\cos\theta) \ , \tag{4.10}$$

where $P_\lambda(\cos\theta)$ are the Legendre polynomials, and θ is the angle between the orientation axis and the direction of emission.

In the case of allowed β transitions with $\Delta I = 0, \pm 1$ and no parity change, just the terms with $\lambda = 0$ and 1 are non-zero, and only $\lambda = 1$ contributes to the observed decay asymmetry, thus

$$W(\theta) = 1 + \sqrt{2I+1}\, \rho_0^1 A_1 \cos\theta \ . \tag{4.11}$$

Furthermore, for such decays A_1 can be represented [Kra86] as

$$A_1 = \sqrt{\frac{I+1}{(2I+1)I}} \frac{v}{c} a \ , \tag{4.12}$$

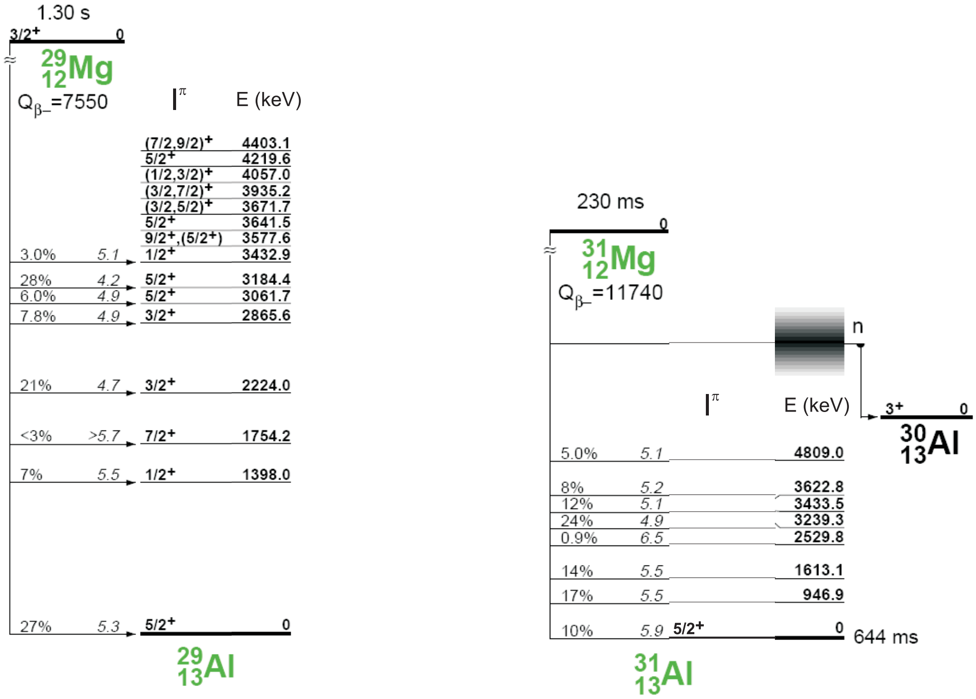

Figure 4.4: β-decay of ^{29}Mg (left) and ^{31}Mg (right). The latter: before our measurements. Source: [Fir03] and [Mar05].

where v is the velocity of β particles which for typical decay energies of several MeV is close to the light velocity and $v/c \approx 1$, while a is the asymmetry factor equal [Kra88] to

$$\begin{array}{ccc} -1 & \text{for} & \Delta I = -1 \\ I_i/(I_i+1) & \text{for} & \Delta I = +1 \\ -1/(I_i+1) & \text{for} & \Delta I = 0 \quad \text{(Gamow-Teller transition)} \\ 0 & \text{for} & \Delta I = 0 \quad \text{(Fermi transition)}\ , \end{array} \tag{4.13}$$

with I_i being the spin of the decaying state and ΔI the spin change in the decay of the nucleus.

For neutron-rich Mg isotopes studied so far with the β-asymmetry technique, only the levels involved in the β-decay of ^{29}Mg (Fig. 4.4) are known well enough to determine the asymmetry parameter. Summing over the decay branches with known spin comprising almost 100 % of all decays gives an asymmetry factor equal to only $a = 21(6)\,\%$. For ^{31}Mg no predictions of the expected asymmetry can be made, since there is scarce information about its decay, as shown in Fig. 4.4.

The statistical tensor ρ_0^1 can be easily connected with the nuclear spin polarisation P_I (see eqn. 4.5) [Bli57]

$$\rho_0^1 = \sqrt{\frac{I}{I+1}}\,\frac{\langle I_z\rangle}{I} = \sqrt{\frac{I}{I+1}}\,P_I\ , \tag{4.14}$$

based on which $W(\theta)$ for allowed β-decays takes the widely known form [Kra86]

$$W(\theta) = 1 + a\frac{v}{c}\,P_I\,\cos\theta\ . \tag{4.15}$$

The asymmetry in the distribution is thus directly proportional to the achieved polarisation, with the latter depending on atomic properties and experimental details as explained in Section 4.2.

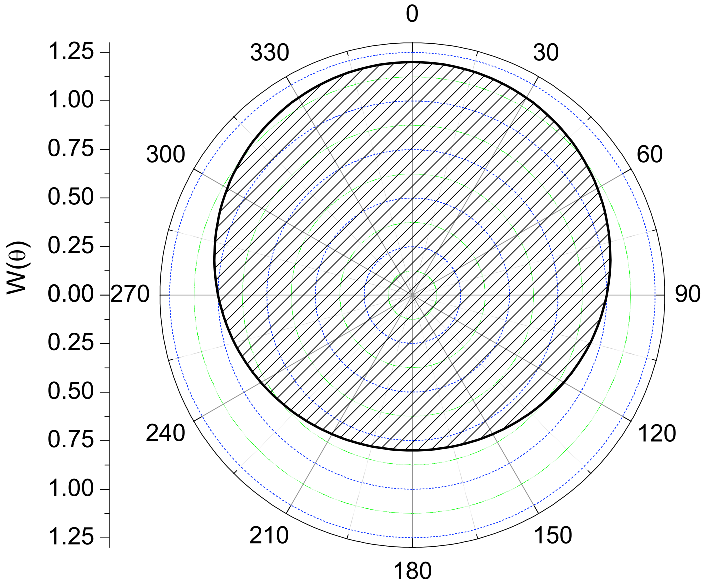

Figure 4.5: Angular distribution of β particles from allowed transitions, on the example of ^{29}Mg.

If the polarised ensemble is imbedded into a host crystal (see Section 4.2), it interacts with its environment. Due to this interaction, the polarisation decreases in time with the so called longitudinal or spin-lattice relaxation time constant T_1 [Abr61]. Therefore, even if unperturbed by external fields, also $W(\theta)$ decays with time, according to the formula

$$W(t) = 1 + a\frac{v}{c}\,P_I(0)\,e^{-t/T_1}\,\cos\theta\ . \tag{4.16}$$

Experimental asymmetry and signal-to-noise ratio

The predicted angular distribution of β-particles from a totally polarised ensemble with $P_I = 1$ is shown in Fig. 4.5 on the example of ^{29}Mg. In an experiment, one can observe the decay asymmetry, which is a normalised difference between the number of β particles N_β registered by detectors of the same detection efficiency placed at angles θ_1 and θ_2

$$A_{exp}(\theta_1,\theta_2) = \frac{N_\beta(\theta_1) - N_\beta(\theta_2)}{N_\beta(\theta_1) + N_\beta(\theta_2)}\ . \tag{4.17}$$

The biggest experimental asymmetry is reached for detectors placed in the directions parallel ($\theta_1 = 0°$), and antiparallel ($\theta_2 = 180°$) to the decoupling magnetic field, and this geometry has been chosen for the experiment. A_{exp} depends on the opening angle 2α of the detectors: it falls with increasing α and reaches about 50 % of A_{max} for a full 4π coverage, as shown in the formula

$$A_{exp}(0,\pi) = a\frac{v}{c}P_I\,\frac{\sin\alpha}{\alpha} \approx \frac{1}{2}a\frac{v}{c}\,P_I(1+\cos\alpha)\ . \tag{4.18}$$

The opening angle plays also a role in the signal-to-noise ratio, and since the number of counts $N(\alpha,\theta)$ is proportional to $\alpha \cdot W(\alpha,\theta)$, the signal-to-noise ratio becomes

$$S/N = A_{exp}/\left(\frac{2}{N(0)+N(\pi)}\sqrt{\frac{N(0)\,N(\pi)}{N(0)+N(\pi)}}\right) \propto a\frac{v}{c}\,P_I\frac{\sin\alpha}{\sqrt{\alpha}}\ . \tag{4.19}$$

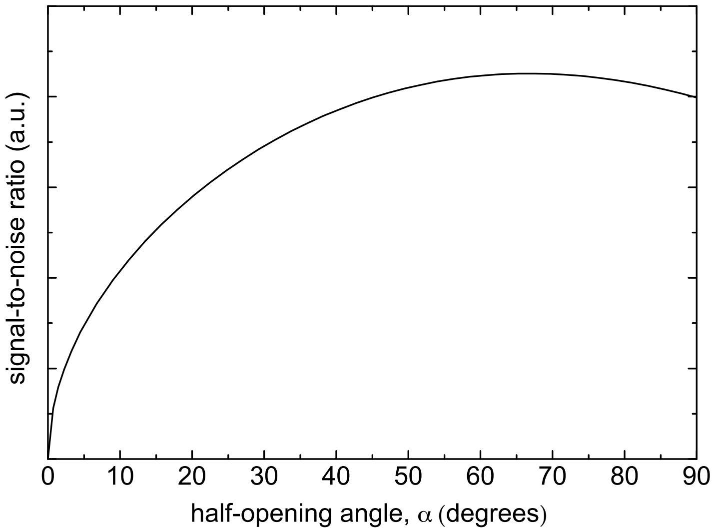

Figure 4.6: Signal-to-noise ratio of the experimental β-decay asymmetry as a function of half-opening angle.

This is plotted as a function of the half-opening angle α in Fig. 4.6. The maximum is reached for about 65°, an angle which doesn't depend on the asymmetry factor or on the amount of spin polarisation. It should be noted here that the increased back-scattering probability for β particles incident on the detector plane at lower angles (i.e. at large opening angles) was neglected.

Due to requirements of mechanical stability of the 50 μm-thin molybdenum windows in the aluminum vacuum chamber, α in the experiment was chosen to be 35°, which corresponds to about 10 % of the full solid angle. This allows to obtain about 75 % of the maximum signal-to-noise ratio and to observe more than 90 % of the maximum achievable asymmetry.

In this method, contrary to fluorescence detection, one synchronises the measurements with the arrival of the proton pulse which produces the radioactive nuclei. This is caused by the fact that one wants to observe all β particles emitted from the beam of radioactive nuclei with half-life around 1 s. Thus, for one proton pulse (coming every 1.2 s or its multiples) only one data point (one channel) is saved. A typical scan consists of 100-500 channels, hence in the best case one scan takes 2-10 minutes.

The signal-to-noise ratio can be evaluated for one channel based on eqn. 4.19:

$$S/N = A_{exp}/\left(\frac{2}{2\epsilon N}\sqrt{\frac{(\epsilon N)^2}{2\epsilon N}}\right) = A_{exp}\sqrt{2\epsilon\, n\, s}\,. \tag{4.20}$$

where ϵ is the total efficiency of detecting a β particle for each ion reaching the entrance of the experimental setup. N is the total number of β particles emitted in one measurement, while n are the particles emitted during one scan in one channel. Finally, s is the number of scans in a measurement. Like in fluorescence detection, the minimum acceptable yield a_{min} can be evaluated following the criterium $S/N > 3$. Assuming that the observation time is long enough to see the decay of most implanted nuclei, $n \approx a$, and using eqn. 4.20, the minimum yield is given by

$$a_{min} = \frac{9}{2\epsilon\, s\, {A_{exp}}^2}\,. \tag{4.21}$$

The usual achieved asymmetries are in the range of $A_{exp} = 3\,\%$. The $\epsilon = 5\,\%$ includes about 50 % transmission efficiency inside our setup, 10 % of the full solid angle covered by each of the detectors and almost 100 % detector efficiency. Assuming, like before, that the resonance should be visible within one hour with 100 channels per scan, this corresponds to $s = 30$ scans in a measurement, if every consecutive proton pulse is available. These conditions give $a_{min} = 3000$ atoms/s.

Since the nuclei have a finite lifetime τ, the intensity of radiation decreases with time and limits the observation to a few times τ after the implantation. This leaves the polarisation and angular distribution unchanged, but decreases the number of detected β particles. Assuming that all observed nuclei are implanted into the crystal at $t = 0$, the number of nuclei present in the ensemble at a time t is given by

$$n_{tot}(t) = n_{tot}(0)\, e^{-t/\tau} \; . \tag{4.22}$$

Therefore the total number of β particles emitted in all directions of space within the time interval dt is

$$dN_\beta(t) = -d\, n_{tot}(t) = \frac{1}{\tau}\, n_{tot}(0)\, e^{-t/\tau}\, dt \; . \tag{4.23}$$

After including decay asymmetry, the number of particles emitted in a given direction in space becomes

$$dN_\beta(t,\theta) = \frac{1}{\tau}\, n(0)\, e^{-t/\tau}\, (1 + a\frac{v}{c}\, P_I(t)\, \cos\theta)\, dt \; , \tag{4.24}$$

where $n(0)$ represents the particles coming from an unpolarised ensemble detected at $t = 0$ and at any angle θ.

If the decay is observed for a time period T, a time-integrated value is recorded:

$$N_\beta(T,\theta) = \int_0^T dN_\beta(t,\theta)\, dt. \tag{4.25}$$

Taking into account that the detectors are placed at 0 and 180 degrees and that they both cover an opening angle 2α, the two above expressions become

$$dN_\beta^{0,180}(t,\alpha) = \frac{2}{\tau}\, n(0)\, e^{-t/\tau}\, (\alpha \pm a\frac{v}{c}\, P_I(t)\, \sin\alpha)\, dt \; , \tag{4.26}$$

and

$$N_\beta^{0,180}(T,\alpha) = \int_0^T dN_\beta^{0,180}(t,\alpha)\, dt \; . \tag{4.27}$$

From the above equations, the final expressions for instantaneous β-decay asymmetry at time t, $A(t)$, as well as the average asymmetry observed during time T in our experiment take the following form

$$A(t) = a\frac{v}{c}\, P_I(t)\, \frac{\sin\alpha}{\alpha} \; , \tag{4.28}$$

$$\overline{A}(T) = a\, \frac{v}{c}\, \frac{\sin\alpha}{\alpha}\, \frac{\int_0^T e^{-t/\tau}\, P_I(t)\, dt}{\int_0^T e^{-t/\tau} dt} \; . \tag{4.29}$$

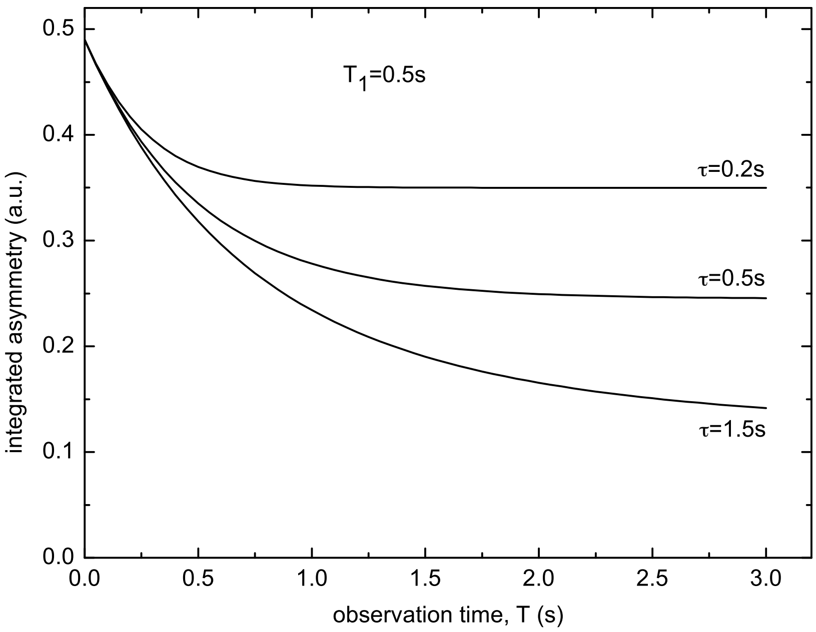

Figure 4.7: Average asymmetry as a function of the observation time for β-decay from states of different lifetimes ($T_1 = 0.5$ s in all three cases).

Atomic and nuclear resonances seen in the β-decay pattern

Atomic resonances can be observed in β-decay asymmetry thanks to the optical pumping mechanism, which leads to the creation of the nuclear polarisation. The principles of this method, as well as the reachable asymmetries and factors influencing them have been described in Section 4.2. Here, the temporal evolution of the expected asymmetries and of the signal-to-noise ratios will be discussed, under the simplifying assumption that the implanted nuclei arrive at time $t_0 = 0$.

Since the polarisation in presence of only static magnetic field decreases in time as e^{-t/T_1}, formula 4.28 for the instantaneous experimental asymmetry becomes

$$A(t) = A(0)\, e^{-t/T_1}, \tag{4.30}$$

where $A(0)$ is the initial asymmetry reached in the optical pumping process, which decreases with the time constant equal to the longitudinal relaxation time. The average asymmetry, however, decreases more slowly according to the formula

$$\overline{A}(T) = A(0) \frac{T_1}{T_1 + \tau} \frac{1 - e^{-T/\tau'}}{1 - e^{-T/\tau}} \ , \tag{4.31}$$

where τ' is the modified lifetime given by

$$\frac{1}{\tau'} = \frac{1}{\tau} + \frac{1}{T_1} \ . \tag{4.32}$$

As seen from the above, the average asymmetry depends not only on the longitudinal relaxation, but also on the nuclear lifetime. For observations in the same host crystal, which implies the same T_1, nuclei with shorter lifetimes will show higher asymmetry at a given observation time, as presented in Fig. 4.7. This can be explained as follows: for shorter τ

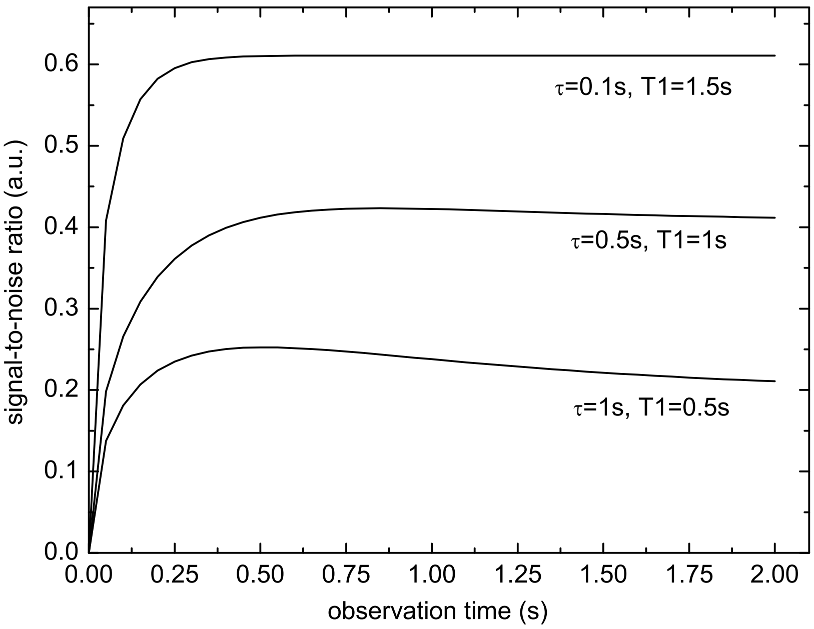

Figure 4.8: Expected average signal-to-noise ratio for the asymmetry of β-decay as a function of observation time.

more β particles are emitted at the beginning of the measurement, when the polarisation had little time to relax, and thus the asymmetry is larger.

Differently for the signal-to-noise ratio, S/N falls in time but $\overline{S/N}$ increases and saturates or reaches a maximum followed by a slow decrease, depending on the relative values of T_1 and τ. This temporal evolution of $\overline{S/N}$ is shown for three different cases in Fig. 4.8. For $T_1 < \tau$ or $\approx \tau$ a maximum is visible at around $t = T_1$, whereas for $T_1 > \tau$, $\overline{S/N}$, i.e. the average signal-to-noise ratio shows saturation behaviour. The optimal time of observation of emitted radiation is thus determined by the signal-to-noise ratio.

Nuclear magnetic resonances, on the other hand, are recorded in the presence of static B_0 and oscillating B_1 magnetic fields. If the oscillation frequency is close to the precession frequency of the spins (ω_L), the achieved polarisation changes periodically with the frequency ω_{eff}, and under the influence of relaxation it is eventually destroyed according [Mat71] to the expression

$$P_I(t,\omega) = P_I(0) \cdot e^{-t/T_1}(\cos^2\beta + \sin^2\beta\,\cos\omega_{eff}t)\ . \tag{4.33}$$

Here β is the angle between the symmetry axis and the direction of the so called effective field, given by $\tan\beta = B_1/((1-\omega/\omega_0)B_0)$, whereas $\omega_{eff} = \sqrt{(\omega_0-\omega)^2 + (\gamma\,B_1)^2}$ and $\gamma = g_I\mu_N/\hbar$.

By inserting the above equation into formula 4.29, one obtains [Mat71]:

$$\overline{A}_{rf}(T,\omega) = a\frac{v}{c}\,P_I(0)\,\frac{\tau'(1-e^{-T/\tau'})}{\tau(1-e^{-T/\tau})}\,\frac{1+(\omega-\omega_L)^2\tau'^2}{1+[(\omega-\omega_L)^2+(\gamma B_1)^2]\,\tau'^2}\ . \tag{4.34}$$

The first term describes the temporal decrease of the average asymmetry, which is the same as in absence of the oscillating field (eqn. 4.31). The second term shows the change in asymmetry depending on the frequency and the strength of the applied field.

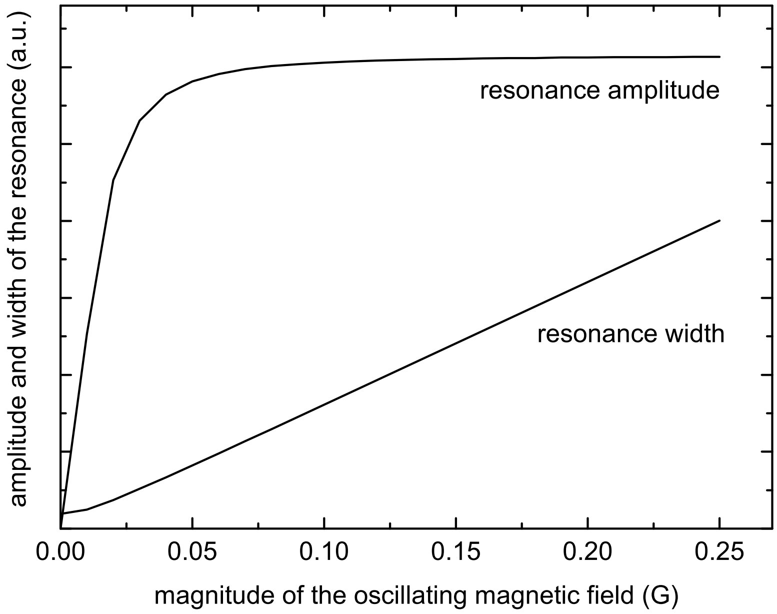

Figure 4.9: Width and amplitude of an NMR resonance as a function of the strength of the applied oscillating field (the values used for the calculations, $\tau = 0.36$ s and $T_1 = 0.5$ s, correspond to ^{31}Mg implanted into a MgO crystal.)

$\overline{A}_{rf}(\omega)$ can be also written in the form

$$\overline{A}_{rf}(\omega) = -D \cdot \frac{(\Gamma/2)^2}{(\omega-\omega_L)^2 + (\Gamma/2)^2} + C \; , \tag{4.35}$$

from which it is clear that the average decay asymmetry as a function ω has a Lorentzian shape of half-width equal to

$$\Gamma = 2\sqrt{(\gamma B_1)^2 + 1/\tau'^2} \tag{4.36}$$

and with the amplitude corresponding to

$$D = a\frac{v}{c}\, P_I(0)\, \frac{\tau'(1-e^{-T/\tau'})}{\tau(1-e^{-T/\tau})} \frac{(\gamma B_1)^2}{1/\tau'^2 + (\gamma B_1)^2} \; . \tag{4.37}$$

The last term, C, corresponds to the baseline and is determined by the polarisation obtained in the optical pumping process, as well as by the integration time:

$$C = a\frac{v}{c}\, P_I(0)\, \frac{\tau'(1-e^{-T/\tau'})}{\tau(1-e^{-T/\tau})} \; . \tag{4.38}$$

As seen above, the integration time influences only the amplitude of the resonance, which decreases in the same way as the undisturbed asymmetry (eqn. 4.31). The magnitude of the applied oscillating field, on the other hand, modifies both the width and the amplitude of the NMR signal, which both increase with stronger field (shown in Figure 4.9). For this reason B_1 has to be chosen in such a way that the resonance amplitude is close to saturation, but the power broadening is minimal.

Both Γ and D also depend on the modified lifetime of the investigated nuclear state. Since τ' depends in the same way on τ and T_1, this implies that a short lifetime has the same

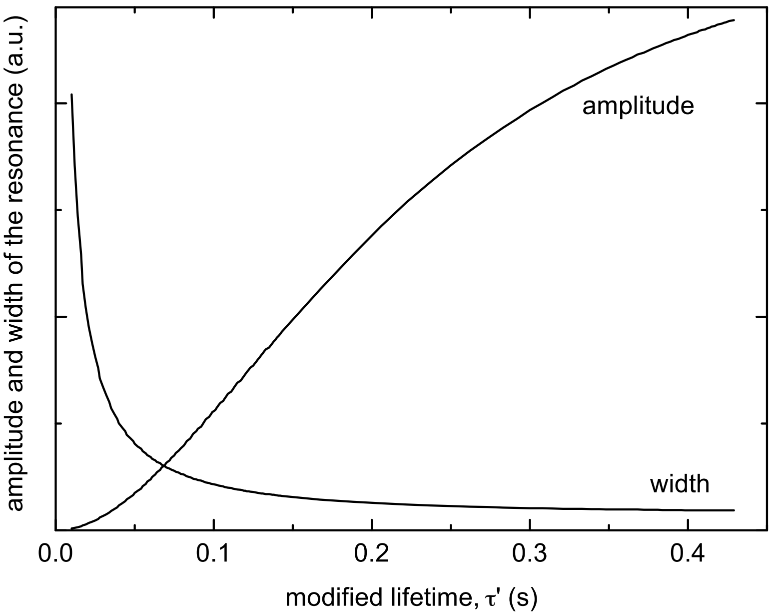

Figure 4.10: Width and amplitude of NMR resonances for different effective lifetimes τ'.

effect on resonances as a fast relaxation: they both shorten the observation time and thus increase the width of the resonance. Furthermore, small τ' also decreases the amplitude. For this reason shorter lived-isotopes or host crystals with faster relaxations require higher field powers in order to obtain saturation. However, this also implies broader resonances (see Fig. 4.10). If $1/\tau' \gg \gamma B_1$, then Γ is determined only by the lifetime.

It must be, however, noted that the above Lorentzian resonance shape neglects mechanisms responsible for the inhomogeneous line broadening, like the inhomogeneity of the magnetic field, which often limits the achievable precision.

The signal-to-noise ratio in principle depends on both τ' and B_1. However, if the resonance is close to saturation, i.e. all polarisation is destroyed, $D = \overline{A}$ and the formula for S/N in the NMR case does not depend on the strength of the oscillating field, but it takes the same form as when observing atomic resonances. For this reason, in the measurements always the same observation time T was taken for the detection of atomic and nuclear magnetic resonances.

4.4 Experimental setups

This section presents the ISOLDE facility which provides the beams of Mg isotopes, as well as the collinear laser spectroscopy setup, in which laser and β-NMR spectroscopy measurements are performed.

4.4.1 ISOLDE facility

The experiments presented in this thesis have been performed at the on-line isotope mass-separator ISOLDE [Kug00] located at the European Organization for Nuclear Research CERN in Geneva, which is dedicated to the production of a large variety of radioactive ion beams for different experiments in the field of nuclear and atomic physics, solid-state

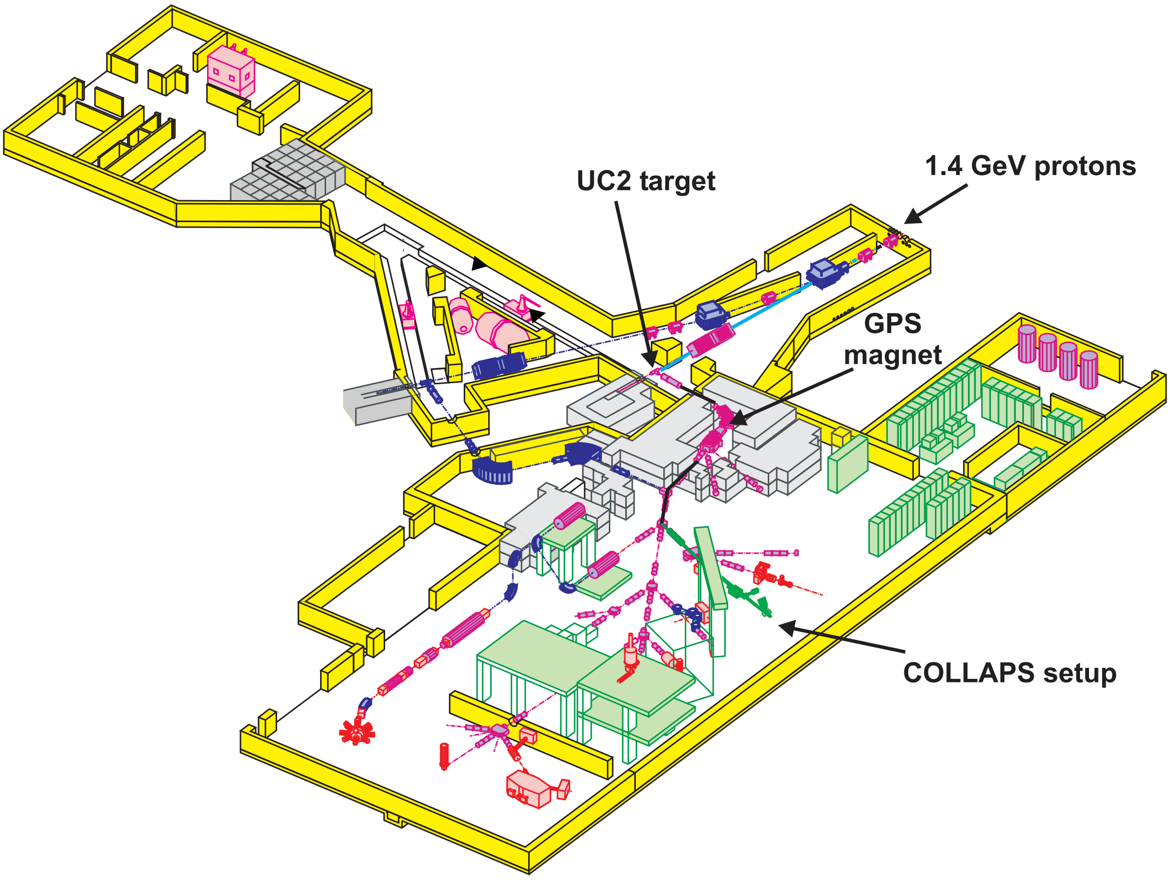

Figure 4.11: ISOLDE facility at CERN.

physics, life sciences and material science.

The radioactive nuclides are produced in thick high-temperature targets via proton-induced nuclear reactions. The radioactive species are subsequently ionised, extracted and accelerated, after which they are mass separated and steered to the experiments. Until now more than 600 isotopes of over 60 elements (Z=2 to 88) have been produced with half-lives down to milliseconds. The intensities reaching up to 10^{11} ions per second in favourable cases drop rapidly far from stability towards such short-lived nuclides.

The 1.4 GeV proton beam from the CERN Proton Synchrotron Booster has a maximum intensity of 3×10^{13} protons per pulse. The pulses are 2.5 μs in length and their period is a multiple of 1.2 s. Their impact on a heavy target induces spallation, fission or fragmentation reactions. The target material is chosen so that the production of the element of interest is as high as possible. Since neutron-rich Mg isotopes are most abundantly produced via fragmentation in a standard ISOLDE uranium carbide (UC_2) target, this material was used in all our measuring sessions.

The product nuclei evaporate from the target material and diffuse via a drift tube to a connected ion source (Fig. 4.12). In order to make the evaporation process fast enough, and to avoid adsorption of the produced species, the target material is contained in a heated tube which is kept at a temperature of about 1500 K. This is especially important for short-lived isotopes.

The atoms are then ionised in a 3 cm long tungsten cavity heated to 2000-2600 K. The ISOLDE ion source is adapted to the desired element. Depending on the chemical properties

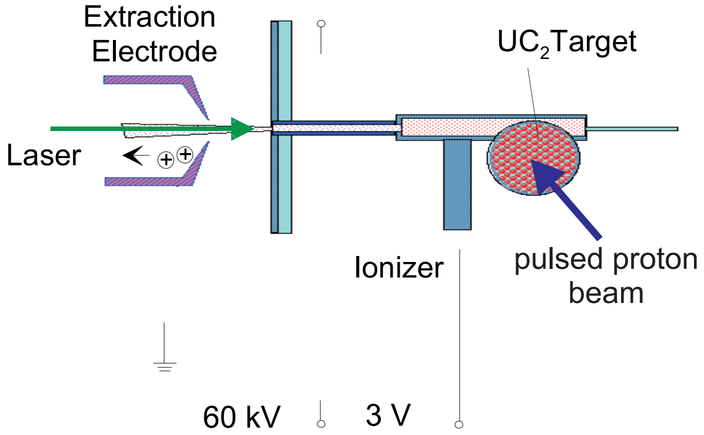

Figure 4.12: A schematic picture of the ISOLDE target with the laser ionisation and extraction section.

of the isotopes, surface ion sources (for elements with low work function like alkali metals), plasma ion sources (for elements with high ionization energies like noble gases) or resonant laser ionisation ion sources, RILIS, [Fed00] (in other cases) are used. For Mg, a three-step laser ionization was chosen, since it offers high efficiency (around 10 %) and in addition it gives high element selectivity [Koe03]. To allow efficient ionisation, enough light power has to be provided: pulsed lasers with a high repetition rate are used for this purpose. The laser light at the required frequencies is produced by dye lasers (including doubling or tripling of their frequencies) pumped by copper-vapour lasers with the repetition rate of 11 kHz. This rate is high enough to ensure that the probability of each atoms to be ionised in close to one. At the same time, the power allows to reach at least several percent of efficiency. The lasers are placed in a small laboratory inside the ISOLDE hall, and from there the laser beams are sent through a quartz window in the separator magnets straight into the hot cavity of the ion source.

The typical ISOLDE yields for neutron-rich Mg isotopes from UC_2 targets and laser ionisation are presented in Table 4.1.

Table 4.1: Typical ISOLDE yields for ^{29,31,33}Mg.

A	yield (atoms/s)
29	6.5×10^6
31	1.5×10^5
33	9×10^3

The ions are accelerated to 60 kV by an electrostatic potential and are guided to the separation zone. The separation is based on magnetostatic deflection, where species with the same energy but different masses are bent by different angles in a magnetic field perpendicular to the direction of their movement. This is performed in one of two ISOLDE bending magnets, the General Purpose Separator (GPS) with the mass resolution m/dm=2500 which is not large enough to reject all isobars. For neutron-rich Mg nuclei the most disturbing contaminant is from surface-ionised sodium. However, all neutron-rich Na isotopes have half-lives shorter than the isobaric Mg, $t_{1/2}(^{29}\mathrm{Na})$ = 45 ms and $t_{1/2}(^{31}\mathrm{Na})$ = 17 ms, and their yield is lower than 10 % of the Mg yield. Therefore one can reduce their influence by starting

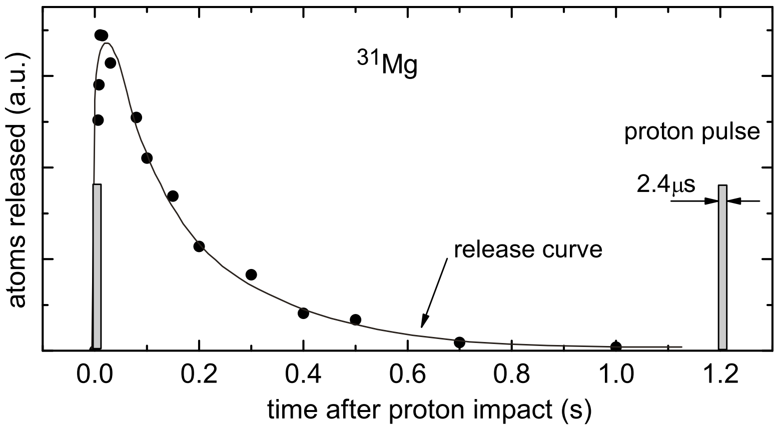

Figure 4.13: The typical time structure of the ISOLDE proton pulse and of the produced radioactive beam on the example of ^{31}Mg.

the measurement 50-100 ms after the proton pulse, when most of them have decayed. Other isobaric contaminants, such as ^{29}Al and ^{31}Al, have considerably longer lifetimes than the corresponding Mg nuclei and their surface-ionisation production rates are lower than 5 % of the Mg rates.

The ions selected by the magnet are guided to the setup for collinear laser spectroscopy with use of electrostatic deflectors and quadrupoles, bending and focusing the beam. The transmission is close to 100 % up to the entrance to the setup, and the acceptance into the setup is typically in the range of 50 %. Due to the pulsed nature of the proton beam, also the ion beam has a distinct time structure whose details depend on the diffusion and effusion time in the target. As an example, Fig. 4.13 shows the release of ^{31}Mg. The pulsed beam allows synchronization of our measurements with the arrival of the proton beam, and – if necessary – also with the ionising lasers, thus leading to higher efficiencies and the best possible background reduction.

4.4.2 Collinear laser spectroscopy setup

The setup for laser and β-NMR spectroscopy is located about 10 m from the production target. It has been installed at ISOLDE in 1980 [Neu81], [Buc82], [Mue83] but has undergone numerous modifications and improvements since this time [Neu86], [Arn87], [Sil88], [Sch91], [Geo95], [Kle96], [Gei99], [Gei05]. In the present configuration [Ney05], [Kow05], it is shown in Fig. 4.14.

The experimental system is kept at high vacuum (ca. 10^{-6} mbar) in order to avoid beam losses by collisions with the residual gases. The nuclei of interest are guided into the apparatus via an electrostatic deflector which bends their path by 10°, so that they can be overlapped with the laser light, which enters straight through a quartz window.

After passing 'beam-shaping' elements (quadrupole lenses, horizontal and vertical deflectors), the ion beam reaches the region of post-acceleration. This is achieved via a tunable voltage of maximum ±10 kV amplitude applied in steps to 4 cylindrical electrodes.

The post-acceleration part of the vacuum apparatus is followed by a 20 cm long charge

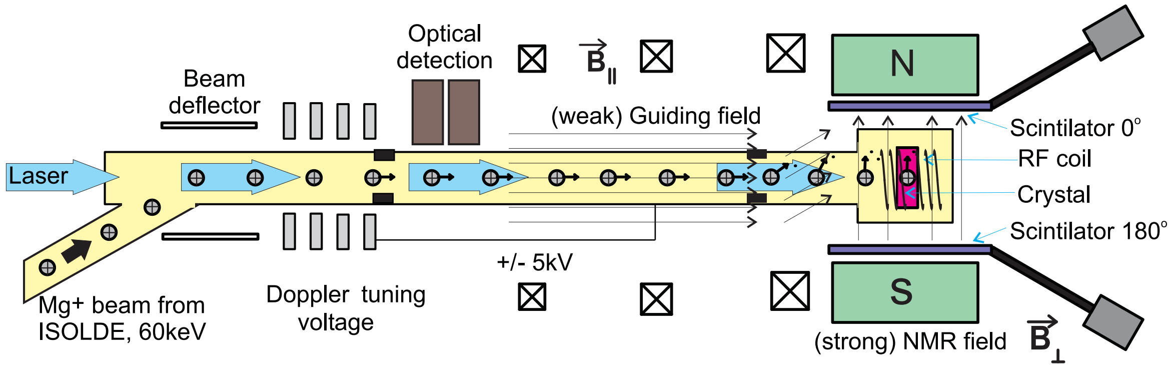

Figure 4.14: The setup for collinear laser spectroscopy and β-NMR measurements.

exchange region filled with a sodium vapour, used to neutralise ^{8}Li, which serves as a reference for NMR studies. For experiments on neutral atoms, the potential at the change exchange cell determines the velocity of the neutral atoms downstream. For measurements on Mg, the charge-exchange cell is not heated, thus there is no Na vapour and no neutralisation takes place.

Next, the ions (or atoms, in case of ^{8}Li) reach a 1 m long interaction region, insulated from both sides by thick plastic flanges and kept at a potential different by 200-500 V from the accelerating region. In this section the Doppler tuning of the ion velocity into resonance with laser light takes place. The voltage offset ensures that the Mg ions are not in resonance with the laser already in the charge-exchange region, a condition which is especially important for optical measurements.

The last part of the vacuum apparatus, used only for β detection, hosts the implantation crystal, surrounded by the NMR coil. Outside the vacuum, thin β detectors and the poles of the NMR-magnet are placed.

Optical detection part

For measurements with optical detection the laser light is linearly polarised and the entrance window is set at Brewster's angle to minimise the reflection losses and to reduce the background from scattered light. The detection of resonances takes place in the first 20 cm of the insulated region. For this purpose, the fluorescence is reflected on one side by a cylindrical mirror, and a 1 : 1 image of the beam is created by two 3-inch lenses, each in front of a UV photomultiplier (Burle 8850). Both lenses and photomultipliers are separated from the vacuum chamber by a quartz window and a very thin metal grid which ensures a constant electric potential inside the observation region. The overall efficiency of 1 : 20 000 can be reached in this configuration.

β detection part

For β-asymmetry detection, the laser light has circular polarisation, which is created by a UV polariser and a quarter-wave plate. In this configuration the light enters the vacuum apparatus by a quartz window placed perpendicular to the beam direction.

The optical pumping effectuating nuclear polarisation takes place in the whole isolated section. The quantization axis for σ^+ or σ^- resonance absorption is established by a small ($B \approx 4$ G) longitudinal magnetic field, the so called "guiding field". Additionally, this region is shielded from external magnetic fields by a μ-metal foil placed outside it.

From the pumping region, the ions are guided to a very homogenous high magnetic field ($dB/B < 10^{-4}$/cm), provided by a conventional electro-magnet operating at 0.2-0.3 T (Bruker). The strong field of the magnet is perpendicular to the "guiding field". The atomic spins are rotated and decoupled adiabatically in the fringe field of the magnet. Since Mg beams are used as ions, there is no danger of destroying the polarisation by uncontrolled pumping effects in the transition region: in this section, due to the voltage applied to the pumping region, the ions are no longer in resonance with the laser light.

The ions are finally implanted into a suitable crystal placed in the centre of the magnet, where the homogeneity of the magnetic field is the highest. The detection of β particles coming from the decaying nuclei is carried out by two pairs of 1 mm thin plastic scintillators (NE102), placed in front of the magnet poles outside the vacuum on both sides of the crystal, at 0 and 180 degrees in respect to the magnetic field. The windows of the vacuum chamber at these two positions are made of 50 μm-thin molybdenum foil, in order to minimise the energy lost by β particles passing through them.

Inside the scintillators, each β particle creates a "shower" of photons which pass through a light-guide and are detected by photomultipliers. The saturation of the photomultipliers in this mode is reached for several million β counts per second, which is not a danger for the ISOLDE yields of ^{29,31}Mg. In order to distinguish the β-signal from γ background, one records the coincidences for each pair of detectors placed on one side of the coil. The two coincidence signals are used to calculate the experimental asymmetries.

In the case of hyperfine structure measurements, the β-decay asymmetry is observed as a function of the potential in the optical pumping region. For NMR studies, on the other hand, the voltage is set at the hyperfine resonance giving highest asymmetry, and a tunable radio-frequency field is applied perpendicular to the strong magnet field. This oscillating field is generated by an rf current flowing through a conducting coil placed around the host crystal and produced in a signal generator of 10^{-8} absolute frequency precision (Rohde&Schwarz). In order to obtain sufficiently high rf field in the coil, the signal from the generator passes through an 100W-broadband amplifier (ENI) and a tunable resonant LCR circuit tuned so that $\omega_{\rm rf} \approx 1/\sqrt{LC}$. The usual amplitude of signals after amplification is in the range of 50-250 mA, which corresponds to the magnetic field amplitudes of about 0.1-0.5 G.

Laser system

Since the experiment uses quasi-continuous ion beams and requires small laser linewidths, a continuous-wave laser system is used, consisting of an Ar$^+$ ion laser (Innova 400 by Coherent) pumping in the visible range (488-514 nm) a ring dye laser (699 by Coherent).

For studies on Mg$^+$ Pyrromethene 556 (1 g/l) was used as the active medium and the 560-nm ring output was frequency-doubled in an external resonator (Wavetrain by Spectra Physics) with a Brewster-cut BBO used as the nonlinear doubling crystal, which has 5-10 % doubling efficiency. In this configuration, with 6 W of Ar$^+$ pumping, intensities of 0.5-1 W at 560 nm and 25-100 mW at 280 nm were reached. For measurement on a reference nucleus, ^{8}Li, a second 699 ring laser was used, with the DCM dye (0.5-1 g/l) as fluorescing medium. In this way powers of 150-300 mW at 670 nm were reached with 6 W pumping.

The dye laser output has about 1 MHz linewidth and a long-term drift smaller than 10 MHz/h. In order to minimise the influence of the long-term frequency drifts on the isotope shift measurements, the resonances are scanned in 1-5 minute intervals for the reference and the isotope of interest, and such sets of measurements are repeated several times. Alternatively, for longer measuring times, an additional stabilisation to less than 2 MHz was used, based on the locking of the dye laser output on a cavity, the length of which was controlled by a stabilised HeNe laser.

The ring-laser wavelength is monitored on a standard lambda-meter (Wavemeter by Burleigh) with 300 MHz precision, which is used only as a rough guide to the expected position of the resonances.

Chapter 5

Experimental results

5.1 Random and systematic uncertainties

There are two kinds of uncertainties present in every experiment [Bar89]. The first type, known as random or statistical, arises from random fluctuations in the registered value from one measurement to another, and it can be reduced by averaging over a large number of observations. The second type is called systematic, since it is due to insufficient knowledge of the experimental conditions causing an unknown difference between the observed and the true value. This difference cannot be eliminated by increasing the number of observations.

In the following section both types of uncertainties will be discussed in the context of our measurements. Also a brief explanation of the fitting and error determination procedure will be given.

5.1.1 Random uncertainties

In our experiment random uncertainties arise, on one hand, from the statistical nature of the observed physical processes, such as emission of a fluorescence photon or of a β particle. On the other hand, they are also due to instability and irreproducibility of the experimental conditions, caused for example by fluctuations of the accelerating voltage, the ion beam current or the laser frequency and intensity. The first type is always included in the evaluated experimental uncertainty and, if possible, so is the latter type.

For a set of data points a fit function $f_i(\widehat{a})$ is defined by a model or theory describing the data in terms of the relevant physics parameters $\widehat{a}$. The evaluation of these fit parameters and their errors is based on the minimisation of the empirical residuals, known also as the chi-square function χ^2_{emp} [Bar89]. For uncorrelated points this function takes the form

$$\chi^2_{emp} = \sum_{i=1}^{N} \frac{(y_i - f_i(\widehat{a}))^2}{\sigma_i^2}\,, \tag{5.1}$$

where N is the number of fitted points, y_i is the value of the observable at each point, $f_i(\widehat{a})$ represents the value of the fitting function at point i, which depends on fit parameters $\widehat{a}$. Finally, σ_i is the uncertainty in y_i, corresponding to 1-sigma deviation, i.e. a 68 % confidence interval in a Gaussian distribution. If y_i is equal to the number of counts n from a statistical process, such as photon or β-particle emission, then $\sigma_i = \sqrt{n}$.

The aim of the fitting procedure is to find such values of parameters $\widehat{a}$ which minimise χ^2_{emp}. The minimisation is performed with the MINUIT package [Jam75], [Jam04], which has been developed at CERN. It is also worth noting that the minimisation of χ^2 is equivalent to finding maximum likelihood, if one can assume that σ_i have a Gaussian distribution [Bar89].

If the parameters for which χ^2_{emp} is minimum describe the data correctly, then the experimental residuals are equal to the residuals expected at a chosen confidence level, $\chi^2_{emp} = \chi^2_{th}$. Since all σ_i used in our analysis correspond to a 68 % confidence level, χ^2_{th} is approximately equal to the number of degrees of freedom $N - k$, which is a difference in the number of points N and the number of fitted parameters k. However, one has to remember that this is the case only for 1-sigma errors, whereas for 2-sigma uncertainties $\chi^2_{th}/(N-k)$ is larger than 1, e.g. $\chi^2_{th}(20) = 31$ and $\chi^2_{th}(80) = 102$.

The approach taken in the thesis is equivalent to a χ^2 Goodness-of-Fit test [Bev69]. Thus, if $\chi^2_{emp}/(N-k) \approx 1$, then $f(\widehat{a})$ and the evaluated parameters are accepted. The uncertainty $\sigma(a_k)$ of parameter a_k is then calculated by finding such $a'_k = a_k + \sigma(a_k)$ that χ^2_{emp} increases by one with other parameters set free [Bar89], [Bev69][1]. The fact that other parameters are not fixed in this procedure allows to take into account the possible correlations between them. As in the case of σ_i, also $\sigma(a_k)$ corresponds to a 68 % confidence level.

If χ^2_{exp} is somewhat larger than χ^2_{th} and there are good reasons to believe that the fitting function is correct, then $f(\widehat{a})$ and parameters a_k which minimise χ^2_{emp} are also accepted. However, the errors of all parameters are increased by $\sqrt{\chi^2_{emp}/(N-k)}$, which is equivalent to multiplying all σ_i by this factor in order to obtain $\chi^2_{emp}/(N-k) = 1$ [Bev69], [Eid04]. Such a situation usually occurs in presence of experimental conditions which cannot be easily taken into account in $f(\widehat{a})$ or σ_i. To these belong fluctuations in laser and ion-beam intensities.

5.1.2 Systematic uncertainties

If the absolute or relative systematic uncertainties are the same during all measurements, their influence on the uncertainty of the fit parameters in $f(\widehat{a})$ can be evaluated using the well-known formula for error propagation [Bev69], according to which the uncertainty of parameter a_k due to the measured quantity x is given by $g'(x) \cdot \sigma(x)$. In order to assess correctly different contributions to the systematic uncertainty in the hyperfine splittings and isotope shifts, one can use the error propagation procedure on the approximate Doppler shift formula (eqn. 4.3). Based on this expression the frequency difference $\Delta\nu_0$ between two transitions of interest in the rest frame of atoms/ions can be represented as

$$\Delta\nu_0 = \frac{\nu_{las}}{c}\sqrt{2e}\left(\sqrt{\frac{U_1}{m_1}} - \sqrt{\frac{U_2}{m_2}}\right), \tag{5.2}$$

where ν_{las} is the laser frequency, U_1 and U_2 are the acceleration voltages at which each of the resonances was observed, whereas m_1 and m_2 are the atom/ion masses, for which, in the case of the hyperfine structure, $m_1 = m_2 = m$.

The systematic error of $\Delta\nu_0$ is hence due to uncertainties in laser frequency, acceleration voltage and ion masses. The contributions from the terms in front of the bracket are straightforward, since they are only proportionality factors. Using the formula for error propagation mentioned above, the uncertainty in the laser frequency $\sigma(\nu_{las})$ gives rise to the term $\sigma(\Delta\nu_0(\nu_{las})) = \Delta\nu_0 \cdot \sigma(\nu_{las})/\nu_{las}$. For $\sigma(\nu_{las}) \approx 0.3$ GHz, dominated by the accuracy of the

---

[1] This procedure is also included in the MINUIT package.

laser wavelength readout, one obtains the relative error in $\Delta\nu_0$ of 3×10^{-7}, which can be neglected in all our measurements.

The parts in the brackets give different uncertainties in the hyperfine structure and isotope shifts. For the mass, in the first case $\sigma(\Delta\nu_0(m)) = \Delta\nu_0 \cdot \sigma(m)/2m$, which corresponds to the relative uncertainty ranging from 5×10^{-10} for stable ^{25}Mg up to 3×10^{-7} for ^{31,33}Mg, based on Table 1.3. In isotope shift studies the absolute mass contribution equals to 1.5×10^{-3} MHz for stable isotopes and about 0.5 MHz for $^{29-33}$Mg. These absolute values result in relative uncertainties in isotope shifts (with ^{24}Mg as reference) between 5×10^{-7} (for ^{26}Mg) and 8×10^{-5} (for ^{29}Mg).

The error propagation is most complex for the acceleration voltage, which consists of three parts, as described in Section 4.4.2. The first one is the ISOLDE voltage $U_{IS} \approx 60$ kV, which is common for all measurements in our experiment. The next part is the main post-acceleration voltage U_{fix}, which stays constant during a measurement on a given isotope but which varies for different isotopes, and can be set to maximum ±10 kV. Finally, there is the small scanning voltage $U_{scan}^{max} = \pm 500$ V, which allows to go across the atomic resonances within one hyperfine multiplet. In all three cases the uncertainty is dominated not by short-term fluctuations of the voltage, but by accuracy of the measuring system (as presented in Table 5.1), which consists of 1000:1 voltage divider and integrating digital voltmeter with respectively 10^{-4} and 10^{-5} relative measuring accuracy.

Table 5.1: Short-term fluctuations in the acceleration voltages and uncertainties in their measurement.

	short-term fluctuations	measurement accuracy
U_{IS}	0.5 V	$10^{-4}U_{IS} \approx 6$ V
U_{fix}	<0.05 V	$10^{-4}U_{fix}+ 0.01\text{V} = 0.01 - 1\text{V}$
U_{scan}	<0.01 V	$10^{-4}U_{scan}+ 0.01\text{V} = 0.01 - 0.5\text{V}$

As seen above, the uncertainty in the accelerating voltages is indeed mainly due to the measuring accuracy. Since U_{fix} and U_{scan} are always measured as a sum (using Julie Research KV10 divider and Prema 6040 voltmeter), they can be treated as one voltage. Furthermore, since the relative uncertainty in their readout is always the same (10^{-4}), one is not interested in the error for absolute values of $U_{fix} + U_{scan}$, but in uncertainty of their difference $\Delta U = U_{fix2} + U_{scan2} - U_{fix1} - U_{scan1}$ for the two resonances. Based on this information, the formula for $\Delta\nu_0$ can be approximated [Mue83] to

$$\Delta\nu_0 = \nu_{las}\sqrt{\frac{eU_{IS}}{2mc^2}}\left(-\frac{\Delta U}{U_{IS}} + \frac{\Delta m}{m}\right) , \tag{5.3}$$

where m is the mass of the lighter isotope and Δm is the isotope mass difference. From this follows that the voltage contributions to the final systematic uncertainty in $\Delta\nu_0$ can be expressed [Mue83] as

$$\sigma(\Delta\nu_0(U_{IS})) = \frac{\nu_{las}}{2}\sqrt{\frac{eU_{IS}}{2mc^2}}\left(\frac{\Delta U}{U_{IS}} + \frac{\Delta m}{m}\right) \cdot \frac{\sigma(U_{IS})}{U_{IS}} , \tag{5.4}$$

$$\sigma(\Delta\nu_0(\Delta U)) = \nu_{las}\sqrt{\frac{eU_{IS}}{2mc^2}}\,\frac{\Delta U}{U_{IS}} \cdot \frac{\sigma(\Delta U)}{\Delta U} . \tag{5.5}$$

In the hyperfine splitting $\Delta m = 0$ and the relative uncertainties in $\Delta\nu_0$ are equal to 0.5×10^{-4}

and 10^{-4} for U_{IS} and ΔU, respectively. This gives the final relative uncertainty around 1.1×10^{-4}, when the two errors are added in quadrature.

Since the voltage difference for two isotopes is mainly determined by the mass-dependent Doppler shift, from eqn. 5.3 follows that $\Delta U/U \approx \Delta m/m$ and the U_{IS} and ΔU uncertainties give a contribution to the error of the isotope shift of about 5 MHz Δm/u each, almost independently of the particular value of $\Delta\nu_0$. After being added in quadrature, the final uncertainty in the isotope shift due to acceleration voltages equals to 7 MHz Δm/u, which corresponds to 4.5×10^{-3} relative uncertainty.

As seen above, the uncertainties in $\Delta\nu_0$ due to the acceleration voltages are several orders of magnitude larger that than those caused by uncertainties in the laser frequency or atomic masses. Therefore in further analysis only these systematic contributions will be included.

For NMR resonances there are clearly fewer systematic contributions, as seen in eqns. 3.54 and 3.55. The largest of them comes from the long term drift of the magnetic field, which is monitored by regularly measuring the electric current flowing through the magnet coils. To be exact, one monitors the voltage on a 0.05 Ω resistor, which is connected in series to the coils of the magnet. For a 24-48 hour period between measurements on Mg nuclei and the ^{8}Li reference, this effect gives a relative systematic uncertainty in the g-factor equal to 5×10^{-5}. The next important contribution comes from the uncertainty in the g-factor of ^{8}Li, which amounts to a relative error of about 10^{-5}. The relative long-term drift in the radio-frequency is smaller than 10^{-7}, and can be thus neglected.

5.1.3 Weighted average of several measurements

In order to obtain a final value of a given parameter a from j measurements, a weighted average is taken, with weights equal to the inverse of the squares of the statistical uncertainties σ_j of each measurement [Bev69]

$$\overline{a} = \frac{\sum_j (a_j/\sigma_j^2)}{\sum_j (1/\sigma_j^2)} \,. \tag{5.6}$$

The statistical error on this average is based on the expression

$$\sigma(\overline{a}) = \frac{1}{\sqrt{\sum_j (1/\sigma_j^2)}} \,, \tag{5.7}$$

when $\chi^2_{emp} = \sum_j (a_j - \overline{a})/\sigma_j^2$ is equal to $\chi^2_{th} \approx j$. If $\chi^2_{emp} > \chi^2_{th}$ and there are reasons to believe that the results are influenced by fluctuations not included in the errors of the individual values, the error of the average is increased by the factor $\sqrt{\chi^2_{emp}/j}$, following the procedure described by the Particle Data Group [Eid04].

Finally, the total statistical error obtained in this way is added in quadrature to the systematic error, which is common for all j measurements, as discussed in [Bar89].

5.2 Isotope shifts and change in charge radii for $^{24-26}$Mg

5.2.1 Isotope shifts of $^{24-26}$Mg

Since ^{24}Mg, ^{25}Mg and ^{26}Mg do not decay, they can be studied in our experiments only by the optical detection of atomic resonances. Measurements on these isotopes were mainly performed to study the feasibility of isotope shift measurements yielding information on the charge radii of radioactive isotopes. In order to eliminate the influence of the long-term drift of the laser frequency and of the accelerating voltages, all measurements were performed in the following way: about 1 minute was used in turn to take scans for mass 24, 25, and 26, and after one such cycle the data were saved. This cycle was repeated several times for each of the two investigated transitions.

In the case of ^{24}Mg and ^{26}Mg with spin 0 the determination of the isotope shift is straightforward: it is the frequency difference $\Delta\nu_0$ of the two resonances. For ^{25}Mg, with spin $I = 5/2$, the hyperfine structure has to be taken into account. In this case one determines the position of the ^{24}Mg resonance, which is the reference, relative to the centre of gravity of the ^{25}Mg multiplet, which is found by fitting the whole hyperfine structure. All ^{25}Mg resonances are fitted with profiles of the same width, and their positions are connected by the formulas for the hyperfine splitting (eqn. 3.2 and 3.14).

The resonances have clearly a Voigt shape [Dem03], i.e. they are a convolution of Gaussian and Lorentzian profiles. The usual full widths at half-maximum for these two distributions are equal to 35 and 40 MHz, respectively. This indicates that the Doppler broadening leading to a Gaussian shape is comparable to the natural linewidth of 41 MHz, which gives rise to a Lorentzian. Power broadening (at the usual laser powers around 1 mW), also leading to a Lorentzian shape, is negligible, since the total observed Lorentz width is comparable with the natural width. With very high statistics, and thus most clear for ^{24}Mg, an asymmetric tail appears on the side of higher acceleration voltage corresponding to lower beam energy (visible to the left of the main peak in Figs. 5.1 and 5.2). This tail is well described by a small resonance of the same width as the main peak, but its source is not yet clear. The fitting procedure is hence the following: First, the isotope with highest signals, ^{24}Mg, is fitted with two Voigt profiles of common linewidth for the main and the satellite peak. Next, the distance (in Volts) and the relative amplitudes of these two peaks, as well as their Lorentz and Gauss widths, obtained from the ^{24}Mg fit, are set to be the same for the other two isotopes. This procedure assures the consistency of the fits. Typical resonances and Voigt fits for $^{24-26}$Mg in both studied transitions are plotted in Figs. 5.1 and 5.2.

The resulting weighted averages of isotope shifts for ^{24,25}Mg and ^{24,26}Mg, together with their statistical and systematic errors, evaluated with help of procedures described in Section 5.1, are shown in Table 5.2. It is somewhat surprising that the difference in isotope shifts measured in D_1 and D_2 lines for ^{24,25}Mg is about 4 MHz larger than the same difference for ^{26,24}Mg. The King plot analysis presented in the following section shows that this would imply an unrealistic ratio of the field shifts in both transitions. The problem may be due to an offset in the fitted centre of gravity in the D_2 line. This could be caused by the hyperfine pumping effects connected to the overlapping of the lines in the D_2 transition, which were not included in the fitting procedure. Furthermore, there is a strong correlation between the fitted A-factor of the ground state and the A and B-factor of the $^2P_{3/2}$ excited state, which are all left as free parameters. Even setting the ground-state A-factor at the literature

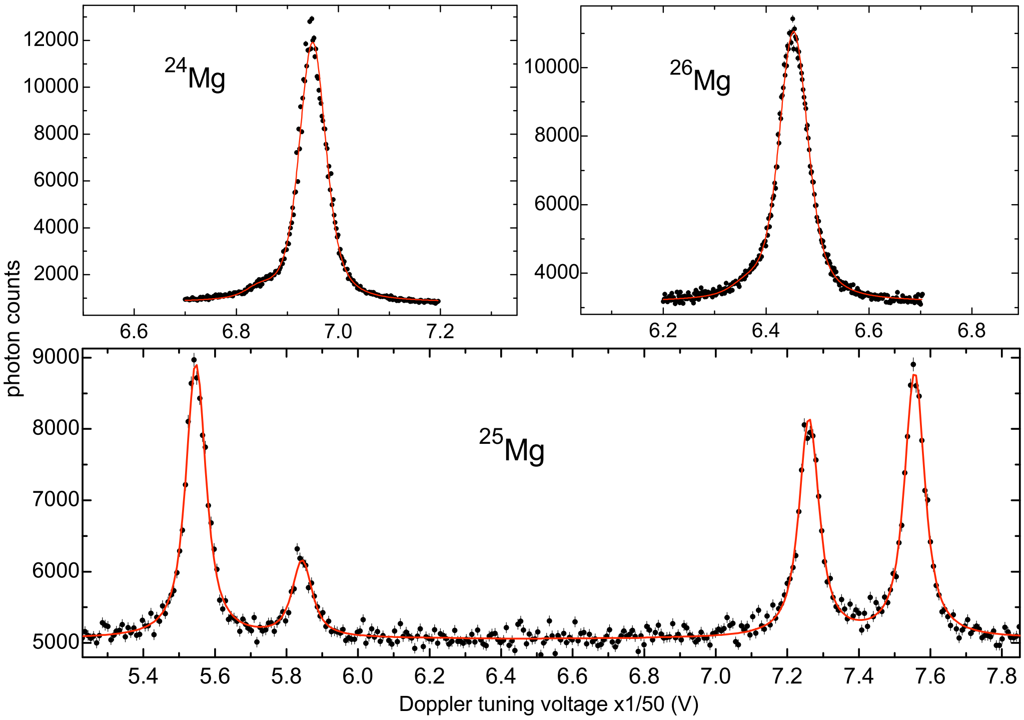

Figure 5.1: Optical resonances in the D_1 transition for $^{24-26}$Mg.

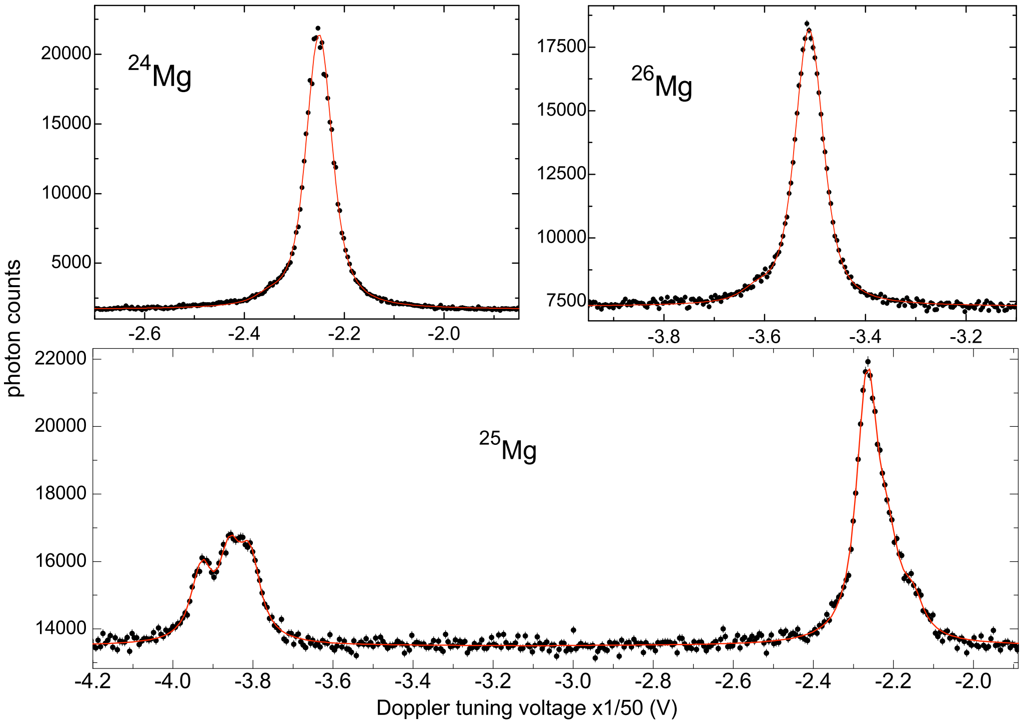

Figure 5.2: Optical resonances in the D_2 transition for $^{24-26}$Mg.

value did not improve the situation, since the unknown values of $A(^2P_{3/2})$ and $B(^2P_{3/2})$ are still correlated and can influence the position of the centre of gravity. In order to decide on the nature of this problem, the measurements should be repeated in the future with better resolution and statistics.

Table 5.2: Isotope shifts between $^{24-26}$Mg in both investigated transitions.

line	A	$\delta\nu_{IS}^{A,24}$ (MHz)	σ_{stat} (MHz)	σ_{syst} (MHz)
D_1	25	1603.7	0.5	7.1
D_1	26	3056.4	0.5	13.7
D_2	25	1598.3	0.9	7.1
D_2	25	3055.5	0.8	13.7

5.2.2 Considerations on the determination of changes in charge radii

So far, due to limited beam-time, no isotope shift study was completed on radioactive Mg isotopes. To prepare the ground for such measurements, this section discusses what was achieved so far in investigations of the stable isotopes, $^{24-26}$Mg.

As presented in Section 3.2.3, charge radii can be determined from optical isotope shifts independently of other methods only where reliable values of the electronic factor F_{el} and the mass shift constant K_{MS} exist. As this is not the case for Mg isotopes, one has to use the results from muonic atoms, summarised in Table 3.2. These data, available for stable $^{24-26}$Mg, can serve as a calibration to determine the changes in radii of radioactive isotopes.

Before using muonic data, one can determine the ratio of the electronic factors for both studied transitions and compare it with calculations. Since the influence of both the $^2P_{1/2}$ and $^2P_{3/2}$ states on the isotope shift is small, F_{el} should be very similar for both lines. This can be verified experimentally with help of the so-called King plot [Kin84], where the modified isotope shifts in the D_1 and D_2 transitions are plotted against each other. Since in such a plot the points corresponding to different isotope pairs lie on a straight line [Kin84]

$$\delta\nu_{IS}^{24,A'}(D_1)\,\frac{m_{24}m_{A'}}{m_{24}-m_{A'}} = \frac{F_{el}(D_1)}{F_{el}(D_2)}\,\delta\nu_{IS}^{24,A'}(D_2)\,\frac{m_{24}m_{A'}}{m_{24}-m_{A'}} - \frac{F_{el}(D_1)}{F_{el}(D_2)}\,K_{MS}(D_2) + K_{MS}(D_1)\ , \tag{5.8}$$

this method can be used to derive the ratio of the electronic factors $F_{el}(D_1)/F_{el}(D_2)$.

The King plot for $^{24-26}$Mg is shown in Fig. 5.3, based on which $F_{el}(D_1)/F_{el}(D_2)$ is obtained to be 1.8(2), which reflects the unexpected 4 MHz difference in isotope shifts discussed above. From experience on other alkali-like ions this ratio should not deviate from 1 by more than a few percent [Mar92] and *ab initio* calculations (eqn. 3.41) predict an equal electronic factor for both transitions. Although the derivation of the charge radii can be based only on the D_1 transition, in which the resonances are well resolved, it would be useful to have reliable cross-check data in the D_2 line, as well. Therefore these measurements should be repeated in the future, before starting studies on radioactive isotopes.

In order to find $\delta\langle r^2\rangle^{24,A'}$ using results on muonic atoms, first one has to make a modified King plot of the available $\delta\langle r^2\rangle$ and isotope shift data in the D_1 and D_2 lines, as described in Section 3.2. According to formula 3.49, if both $\delta\langle r^2\rangle$ and $\delta\nu_{IS}$ are multiplied with the factor $m_{24}m_{A'}/(m_{24}-m_{A'})$, the fit will yield K_{MS} and F_{el}, which are necessary for extrapolations.

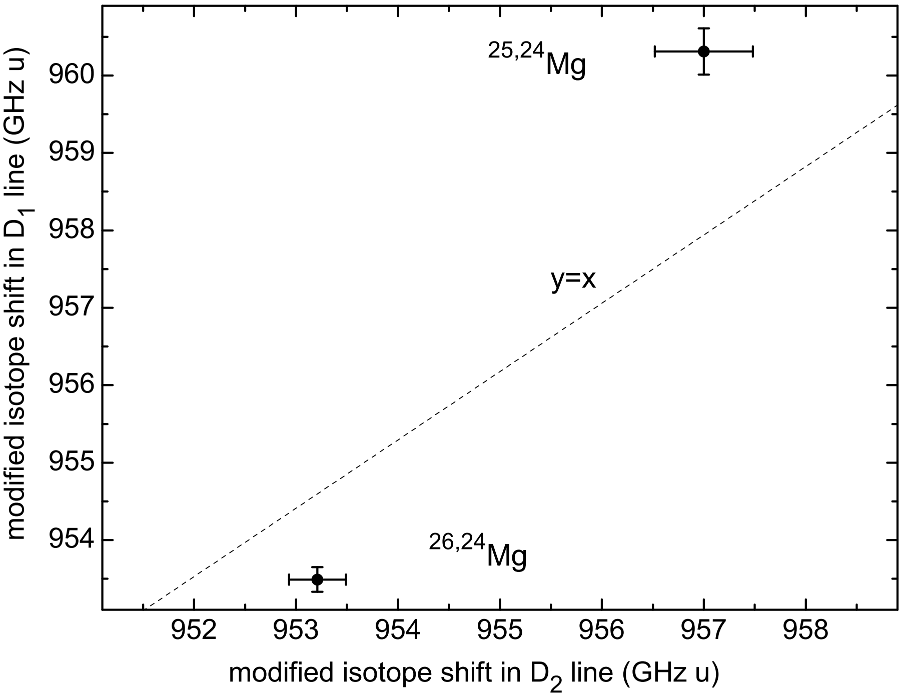

Figure 5.3: King plot for D_1 and D_2 transitions in $^{24-26}$Mg.

Because it facilitates the error handling, in the further analysis $\delta\langle r^2\rangle^{24,A'}$ has plotted on the y-axis and $\delta\nu_{IS}$ on the x-axis. By doing so, eqn. 3.48 becomes

$$\delta\langle r^2\rangle^{24,A'}\frac{m_{24}\,m_{A'}}{m_{24}-m_{A'}} = -\frac{K_{MS}}{F}+\frac{1}{F}\times\delta\nu_{IS}^{24,A'}\,\frac{m_{24}\,m_{A'}}{m_{24}-m_{A'}}\ . \tag{5.9}$$

The modified data used for the fit, together with their statistical and systematic errors, are shown in Tables 3.2 and 5.3, as well as in Fig. 5.4.

Table 5.3: Modified isotope shifts between $^{24-26}$Mg.

line	A	$\delta\nu_{IS}^{24,A'}\ \frac{m_{24}m_{A'}}{m_{24}-m_{A'}}$ (GHz u)	σ_{stat} (GHz u)	σ_{syst} (GHz u)
D_1	25	960.28	0.33	4.3
D_1	26	953.49	0.15	4.3
D_2	25	957.03	0.53	4.3
D_2	26	953.21	0.26	4.3

The evaluated values of K_{MS} and F_{el} are found easily from the straight line defined by the two points. The determination of their uncertainties, however, requires more care. Since absolute systematic errors in $\delta\langle r^2\rangle$ are not the same (only the relative errors are equal), they cannot be added to the fit errors afterwards. In order to handle them properly, it is best to use the covariance matrix $\widehat{V}_y$, in which the diagonal elements are given by the sum of random and systematic errors, and the off-diagonal elements are determined only by systematic errors shared between the points [Bar89]. Since statistical uncertainties of x cannot be neglected, they are projected onto the y-axis and added in quadrature to the statistical uncertainty of y. For Mg , there are two values y_1 and y_2 with random uncertainties σ_1 and σ_2, a common

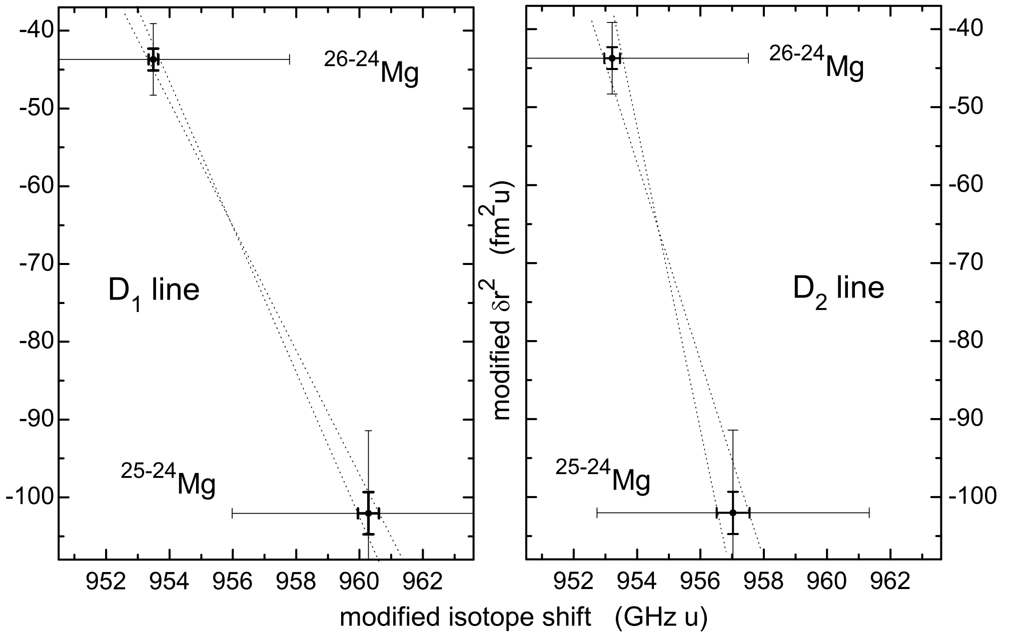

Figure 5.4: Modified King plots: difference in charge radii versus optical isotope shifts for three stable Mg isotopes in D_1 (left) and D_2 (right) lines. Thick line – statistical errors, thin line – systematic errors.

relative systematic uncertainty ε, and random uncertainties in x equal to σ_{x1} and σ_{x2}. In this case $\widehat{V}_y$ takes the form

$$\widehat{V}_y = \begin{pmatrix} \sigma_1^2 + (\varepsilon\, y_1)^2 + (m\sigma_{x1})^2 & \varepsilon^2 y_1 y_2 \\ \varepsilon^2 y_1 y_2 & \sigma_2^2 + (\varepsilon\, y_2)^2 + (m\sigma_{x2})^2 \end{pmatrix} , \tag{5.10}$$

where m is the approximate slope of the fitted line, necessary to project σ_x onto the y-axis.

In the presented formulas the systematic uncertainties of the isotope shifts have been fully neglected, which is possible, because they depend on the mass A approximately in the same way as the mass shift [Kle95], [Kle96]. Due to this property, these uncertainties only change K_{MS}, but have no influence on the differences in charge radii.

The resulting covariance matrix for the fit parameters, $a_1 = -K_{MS}/F_{el}$ and $a_2 = 1/F_{el}$, can be represented as

$$\widehat{V}_a = \begin{pmatrix} 1 & 1 \\ x_1 & x_2 \end{pmatrix} \cdot \widehat{V}_y \cdot \begin{pmatrix} 1 & x_1 \\ 1 & x_2 \end{pmatrix} . \tag{5.11}$$

Table 5.4 presents the values of F_{el} and K_{MS} and their uncertainties for both transitions based on a_1, a_2 and $\widehat{V}_a$ (the latter is also shown in the table).

For the D_1 line, the derived F_{el} agrees very well with the values predicted by *ab initio* calculations (eqn. 3.41), and is quite close to the value derived from the semi-empirical analysis (eqn. 3.38). For the D_2 line, the agreement is much worse, which indicates again that there is indeed a problem with the isotope shifts measured in this transition. K_{MS}, on the other hand, agrees very well with theoretical values (3.44 and 3.46). However, it has a very large error.

Charge radii differences $\delta\langle r^2\rangle^{24,A'}$ for other isotopes can be easily extrapolated by using eqn. 5.8. In order to determine their uncertainty one should use another matrix formula

Table 5.4: Electronic factors, mass shifts and covariance matrices based on isotope shifts for $^{24-26}$Mg in both investigated transitions.

line	$F_{el} = 1/a_2$	$K_{MS} = -a_1/a_2$	$\widehat{V}_a$
D_1	$-116(15)$ MHz/fm^2	$-948(167)^*$ GHz u	$\begin{pmatrix} 1.0 \cdot 10^6 & -1.1 \cdot 10^3 \\ -1.1 \cdot 10^3 & 1.15 \end{pmatrix}$
D_2	$-65(10)$ MHz/fm^2	$-951(190)^*$ GHz u	$\begin{pmatrix} 4.2 \cdot 10^6 & -4.4 \cdot 10^3 \\ -4.4 \cdot 10^3 & 4.6 \end{pmatrix}$

* The systematic error in $\delta\nu_{IS}$ would lead to additional 5 GHz u uncertainty in K_{MS}.

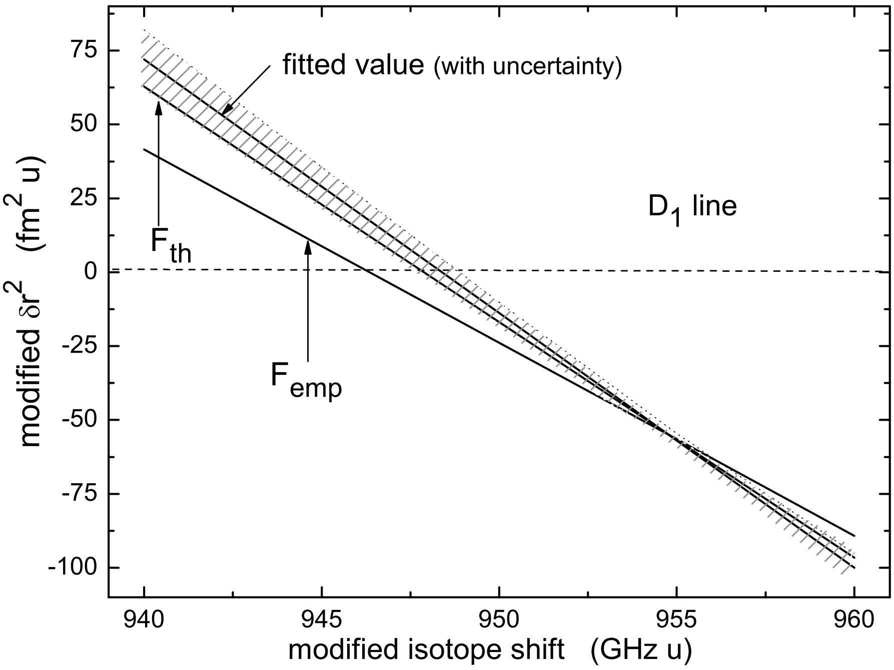

Figure 5.5: Extrapolated modified difference in charge radii, based on the data from muonic atoms and isotope shift measurements for $^{24-26}$Mg in the D_1 transition.

[Bar89], which takes into account correlations between fitted F_{el} and K_{MS}

$$\sigma(y_{extr}) = (1\ \ x) \cdot \widehat{V}_a \cdot (1\ \ x)^T \,, \tag{5.12}$$

where y_{extr} is the extrapolated modified charge radii difference $\delta\langle r^2\rangle^{24,A'} \cdot m_{24} m_{A'}/(m_{24} - m_{A'})$ and x represents the modified isotope shift, equal to $\delta\nu_{IS}^{24,A'} \cdot m_{24} m_{A'}/(m_{24} - m_{A'})$. Based on the above calculations, the expected ranges of $\delta\langle r^2\rangle^{24,A'}$ for both transitions are shown in Figs. 5.5 and 5.6.

Once data for radioactive Mg isotopes are available, it remains to be seen if the extrapolated differences in charge radii between them and ^{24}Mg are accurate enough. If not, one will have to follow the usual procedure, i.e. to fix the electronic factor at the value obtained from *ab initio* calculations or from semi-empirical study. In any case the results of our isotope shift measurements clearly show that the experimental resolution and accuracy are sufficient to be sensitive to the small field shifts containing the information on nuclear charge radii.

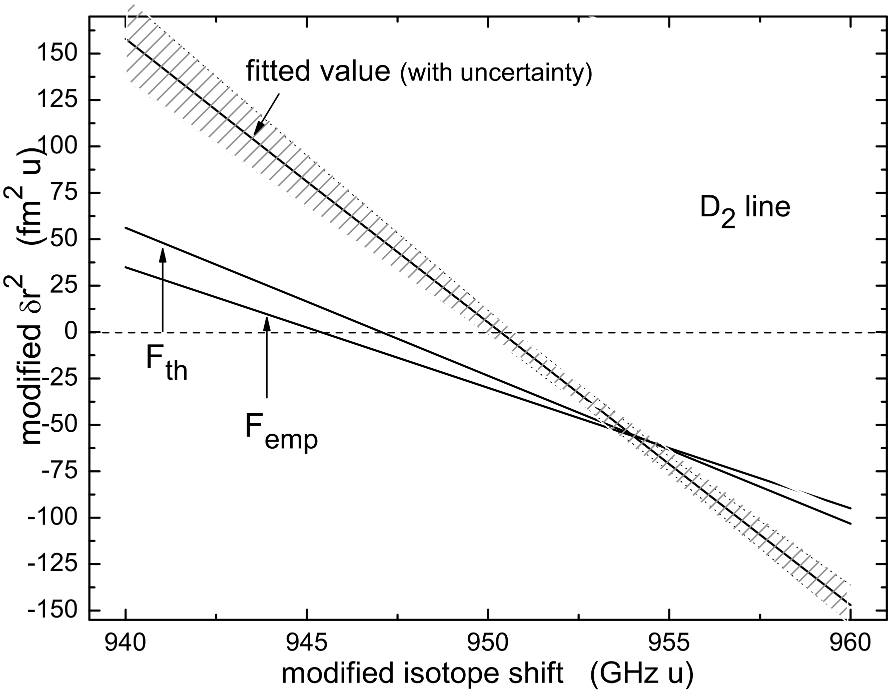

Figure 5.6: Extrapolated modified difference in charge radii, based on the data from muonic atoms and isotope shift measurements for $^{24-26}$Mg in the D_2 transition.

5.3 Hyperfine structure and β-NMR resonances of ^{29,31}Mg

5.3.1 Simulations of the nuclear polarisation reached by optical pumping

Before describing the experimental results on ^{29,31}Mg, this section will present simulations of the expected nuclear polarisation obtained via optical pumping. The calculations were performed within the semiclassical approach, with the laser radiation treated as a classical electric field and the atom (or ion) described by quantum mechanics [Dem03]. Furthermore, the weak-field assumption was made, in which the amplitude of the electromagnetic field of the laser light is relatively small, which allows to describe the interaction between the atoms and the field by standard perturbation theory to first order. This leaves the population of the higher atomic states very small compared with the lower ones, and thus the temporal evolution of the occupations of the levels can be described with atomic rate equations

$$\frac{d}{dt}N_i = \sum_j P_{ij}^{st}(\nu)\,(N_j - N_i) + \sum_j P_{ij}^{sp}\,N_j, \tag{5.13}$$

$$\frac{d}{dt}N_j = \sum_i P_{ij}^{st}(\nu)\,(N_i - N_j) - \sum_i P_{ij}^{sp}\,N_j, \tag{5.14}$$

where N_i and N_j are the populations of the states, whereas P_{ij}^{sp} and P_{ij}^{st} are the probabilities of spontaneous and stimulated transitions between levels i and j. Since we are interested in the atomic and nuclear polarisation, N_i represents populations of all magnetic sub-states m_F

in the ground state, and N_j in the ${}^2P_{1/2}$ or the ${}^2P_{3/2}$ excited state during the interaction with laser light.

The probability for spontaneous emission P_{ij}^{sp} is equal to the Einstein coefficient A_{ij} and can be derived from the lifetime of the excited $P_{1/2,\,3/2}$ states, $\tau \approx 3.8$ ns [Ans89], using the Wigner $3j$ and $6j$ symbols for the coupling of the angular momenta [Sob96]

$$P_{ij}^{sp} = A_{ij} = \tau^{-1}(2F+1)(2F'+1)(2J+1) \begin{Bmatrix} J & F & I \\ F' & J' & 1 \end{Bmatrix}^2 \begin{pmatrix} F & 1 & F' \\ m_F & \Delta m_F & -m'_F \end{pmatrix}^2 . \tag{5.15}$$

Here J and J' denote the total electronic angular momenta of the ground and excited states, I represents the nuclear spin and $\Delta m_F = m'_F - m_F$.

Probabilities of stimulated emission and absorption, on the other hand, are the product of the incident photon flux $\rho(\nu)$ and the optical cross section $\sigma(\nu)$

$$P_{ij}^{st} = \rho(\nu)\,\sigma(\nu). \tag{5.16}$$

The cross section depends on the Einstein coefficient for stimulated transitions B_{ij} and on the absorption profile, which is assumed to be dominated by natural line broadening, thus it can be described by a Lorentzian [Dem03]

$$\sigma(\nu) = B_{ij}\,\frac{1}{2\pi^2\tau}\,\frac{1}{(\nu_{ij}-\nu)^2 + (1/(2\pi\tau))^2}, \tag{5.17}$$

where ν_{ij} is the resonance frequency and B_{ij} can be expressed as $B_{ij} = A_{ij}\,c^3/(8\pi h\nu^3)$.

Assuming a narrow-band incident laser light of frequency ν and power density ρ_{las}, the probability of stimulated absorption and emission becomes

$$P_{ij}^{st} = \left(\frac{c}{2\pi\nu}\right)^3 \rho_{las}\,\frac{A_{ij}}{2h\tau}\,\frac{1}{(\nu_{ij}-\nu)^2 + (1/(2\pi\tau))^2} . \tag{5.18}$$

For the simulation purposes, the above rate equations have been solved numerically with the Runge-Kutta algorithm, which was implemented into a C++ code [Pre02].

After solving the coupled differential equations one obtains the populations of all involved magnetic substates m_F at a chosen moment of time. The adiabatic decoupling in the transitional field to the NMR magnet means a movement along the levels of the Breit-Rabi diagram from the $|F, m_F\rangle$ to the $|m_J, m_I\rangle$ regime. Therefore, with the occupation numbers obtained for the coupled system one can take the corresponding m_I values for the decoupled system and apply the following formula for nuclear spin polarisation which is observed in the experiment

$$P_I = \frac{\sum_{m_I} m_I\, N(m_I)}{I \sum_{m_I} N(m_I)} . \tag{5.19}$$

If one wants to obtain not only the initial P_I, but also the predicted average experimental decay asymmetry for the observation time T, formulas 4.18 and 4.31 have to be used, which give

$$\overline{A}(T) = \frac{1}{2} a \frac{v}{c}\, P_I (1+\cos\alpha)\, \frac{T_1}{T_1+\tau}\, \frac{1-e^{-T/\tau - T/T_1}}{1-e^{-T/\tau}} . \tag{5.20}$$

The asymmetry will be thus lower than the simulated polarisation due to influence of the decay asymmetry factor a, opening angle 2α, half-life of the nucleus $t_{1/2} = \tau \ln 2$ and relaxation time T_1.

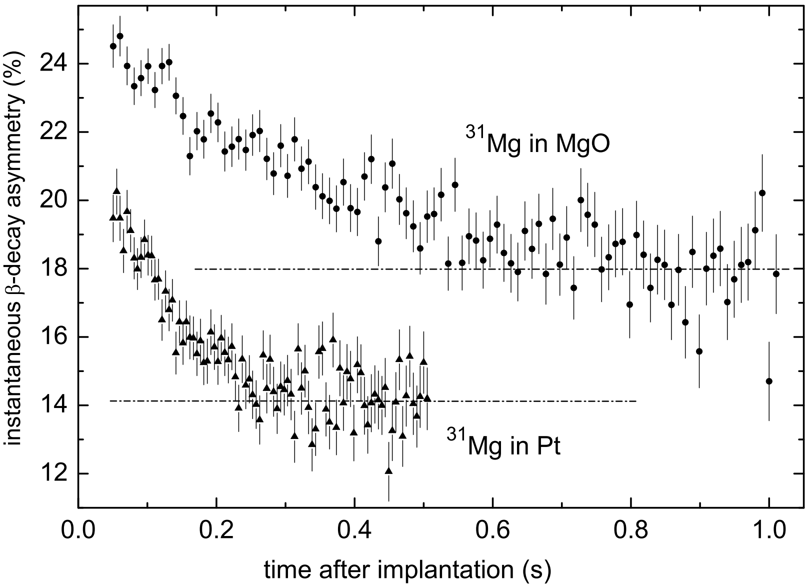

Figure 5.7: Relaxation of β-decay asymmetry in different cubic implantation crystals, on the example of ^{31}Mg. Relaxation is slowest in MgO. The baseline does not correspond to 0 %, but it is the instrumental asymmetry due to experimental conditions.

The free parameters in the simulations are the interaction time, the laser power density ρ_{las}, the laser polarisation and the hyperfine-structure factors A and B. The interaction time was chosen to be 1.5 μs, equivalent to the time required by the ions with the energy around 60 keV to pass 1 m of the optical-pumping region. The laser power densities were taken to be 40 mW/cm^2, corresponding to about 20 mW of UV light, and the polarisation was either circular positive or negative. The results are presented in the next section, in connection with the performed measurements.

5.3.2 Hyperfine structure observed in β-asymmetry

Mg isotopes studied via β-NMR method presented in this thesis are ^{29}Mg and ^{31}Mg. They are both suitable for this experimental approach because they have short half-lives (see Table 1.3) and this method is sensitive enough to cope with the low production yields (Table 4.1).

In the first step, several cubic implantation crystals were tested, since – as discussed in Section 4.3.2 – the host crystal can influence strongly both the linewidth and the amplitude of the observed resonance. At room temperature MgO turned out to be superior to metal hosts, Pt and Au. It showed a relaxation time T_1 around 500 ms, compared to 100 ms for Pt and Au (see Fig. 5.7, note that the baseline does not correspond to 0 %, but it is the instrumental asymmetry due to experimental conditions such as position of the implanted ions or detector efficiency). It also gave the highest average asymmetry, which for the decay of ^{31}Mg (observed for $T = 0.7$ s) was as high as $\overline{A} = 6.7,\%$, compared to 3.1, % for Pt and 1.8 % for Au (NMR showed similar linewidths for all three crystals). MgO was therefore used for further investigations on both isotopes.

The amount of polarisation also depends on the laser power. However, one has to find a trade-off between the reached polarisation and power broadening. Therefore test measurements at several laser intensities were performed, results of which are shown in Fig. 5.8. They

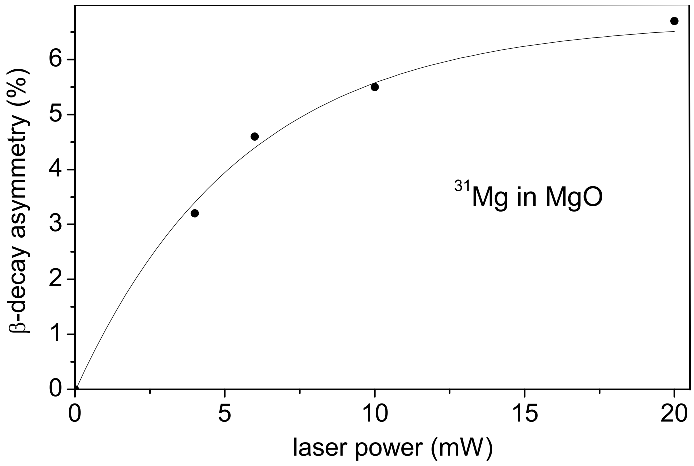

Figure 5.8: β-decay asymmetry as a function of the laser power.

agree well with predictions from the optical pumping simulations described in the previous section. Saturation takes place around 20 mW, corresponding to power density of about 40 mW/cm^2. The consecutive measurements were done with this or slightly lower densities.

After the tests, two successful online sessions were devoted to investigating the hyperfine structures of ^{29}Mg and ^{31}Mg in the D_2 transitions for both laser polarisations. ^{31}Mg – since its spin was unknown – was also studied in the D_1 line. Examples of the structures obtained for ^{29}Mg are shown in Fig. 5.9, for which the observation time T was set to about 2 s per beam pulse due to a relatively long half-life of this nucleus ($t_{1/2} = 1.3$ s). The maximum integrated asymmetry is 2 % and has been reached for both σ^+ and σ^- polarisation with about 10 mW of UV light.

The signs and amplitudes of the asymmetries can be well understood from the simulations including the decoupling scheme of the electron and nuclear spins. The predicted asymmetry pattern is presented also in Fig. 5.9. It was obtained based on the simulated spin polarisation and eqn. 5.20, by multiplying the polarisation at each laser frequency by 0.06. This term is the product of factor 0.15 due to the decay asymmetry factor (Section 4.3.2), 0.91 arising from the opening angle (Section 4.3.2), and 0.32 connected to the finite half-life and the relaxation time in the MgO crystal. The signs and relative amplitudes of the resonances in the simulation agree very well with the experimental data. The observed absolute asymmetries are only 1.5 smaller than the predictions, which can be explained by unpolarised background due to isobars and daughter nuclei or loss of polarisation during implantation into the host crystal.

One problem concerning ^{29}Mg is its relatively long lifetime for β-NMR measurements. Even if only every second proton pulse is used, more than 30 % of the implanted nuclei have still not decayed when the new proton pulse comes after 2.4 s. With 0.5 s relaxation time in the MgO crystal, at this point most of the polarisation has decayed, and thus these nuclei cause a background in β counts, which lowers the observed asymmetry. Then fluctuations in the proton beam intensity directly translate into fluctuations of the asymmetry. An irregular structure of proton pulses is even more disturbing. Depending on the accelerator conditions the asymmetry and the background change from data point to data point and with low asymmetries it makes the observation of resonances very difficult.

The above spectra, however, could yield the A-factors for the hyperfine structure of both involved states, which are presented together with their uncertainties in Table 5.5. They were

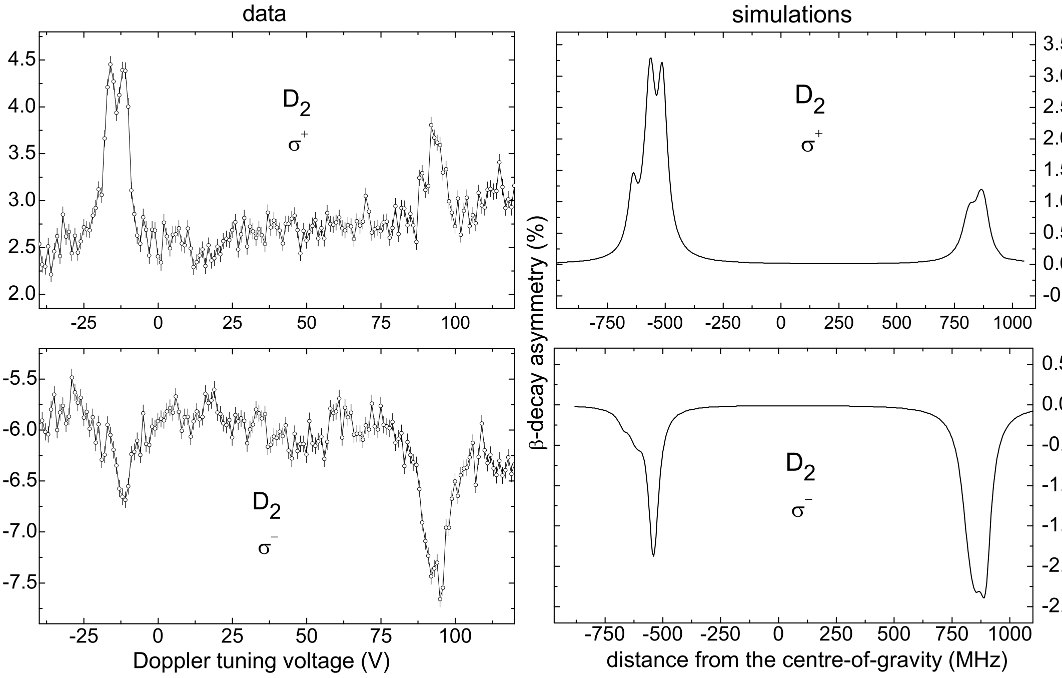

Figure 5.9: Hyperfine structure of ^{29}Mg observed in β-decay asymmetry (left) and the corresponding simulations (right).

obtained by fitting the spectra with several Lorentz resonances of independent amplitudes, but with positions connected by hyperfine splitting formulas (eqns. 3.2 and 3.14) and with common width. The quality of the data did not allow to see any improvement when Voigt profiles were used. Due to low resolution caused by the factors mentioned above, no final result is available for the B-factor of the $^2P_{3/2}$ level, which could reveal the quadrupole moment of ^{29}Mg.

Table 5.5: Hyperfine structure factors for the ground state and second excited state of ^{29}Mg in the D_2 transition.

level	A-factor (MHz)	σ_{stat} (MHz)	σ_{syst} (MHz)
$^2S_{1/2}$	+1131.0	4.5	0.1
$^2P_{3/2}$	+35.1	1.7	0.04

Based on the ground state splitting, the first evaluate of the magnetic moment of this isotope can be already made. Using formula 3.12 and ^{25}Mg as the reference, one obtains

$$g_I(^{29}\mathrm{Mg}) = +0.649(3)\ \mu_N\ , \tag{5.21}$$

with the sign derived from the positions of the hyperfine resonances (a mirror image of Fig. 5.9 would give a negative g-factor).

For ^{31}Mg, spectra for both polarisations and transitions were taken, examples of which are shown in Fig. 5.10. The highest average asymmetry of $\overline{A} = 6.7\,\%$ was obtained in the D_2 line with σ^+ light and $T = 0.7$ s observation time. Since there are only three resonances visible for both transitions, this could mean that the spin of this nucleus is 1/2. Also the simulations

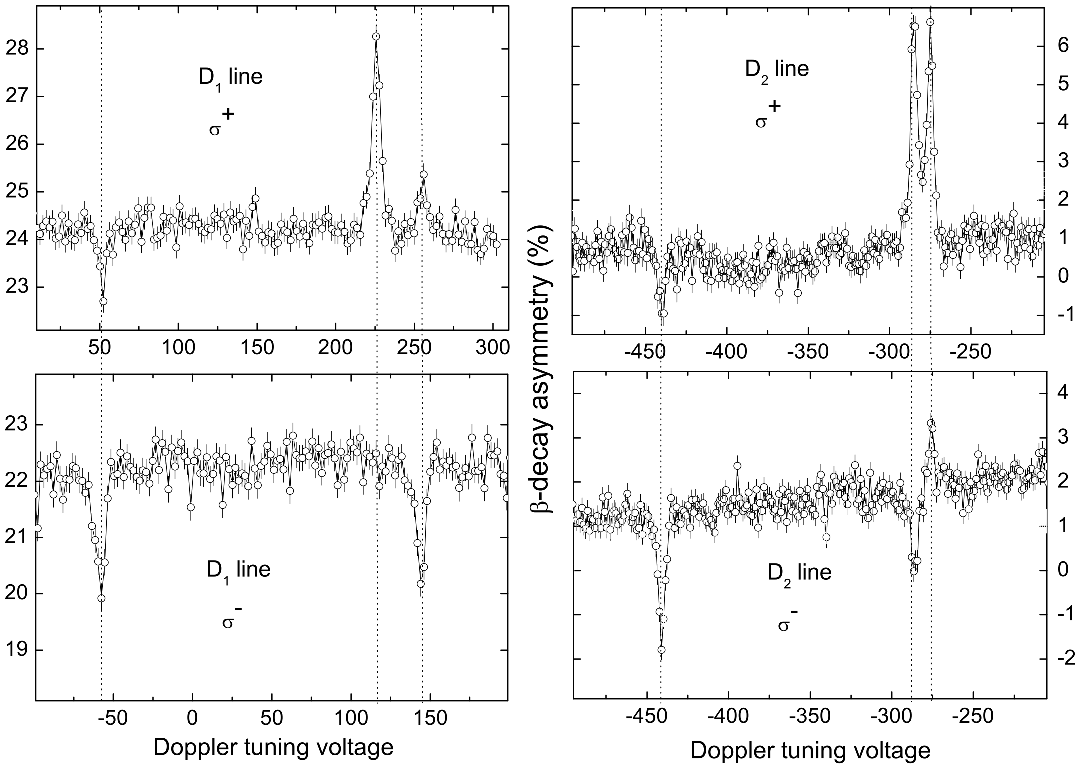

Figure 5.10: Hyperfine structure of ^{31}Mg observed in β-decay asymmetry.

point to $I = 1/2$ as the most possible situation[2]. The positions, relative amplitudes and signs of all observed hyperfine resonances agree very well with the simulations for $I = 1/2$ (Fig. 5.11), whereas they are in clear disagreement with predictions for other spins (Fig. 5.12). However, one could not know *a priori* how well the simulated curves describe the reality. The absence of other hyperfine components in the experimental spectra could also mean that they are hidden or too weak to be visible. Furthermore, spin 1/2 seemed to be excluded for the ground state by all shell model considerations: for unpaired neutron in the $d_{3/2}$ orbit one would expect $I = 3/2$, whereas one neutron in $f_{7/2}$ or $p_{3/2}$ orbits would give spin 7/2 and 3/2, respectively. Therefore, the ^{31}Mg spin could be unambiguously assigned only after performing complementary NMR studies.

The hyperfine A-factors derived from these measurements, and assuming spin 1/2, are summarised in Table 5.6. They were obtained, similarly to ^{29}Mg, by fitting the spectra with three Lorentz resonances of independent positions and amplitudes, but common width. There was no improvement in the fit residuals when Voigt profiles were used.

The above values will be used in Section 5.3.4 to finally determine the spin and the magnetic moment of ^{31}Mg.

---

[2] The asymmetry was derived from the simulated polarisation in the same way as for ^{29}Mg, i.e. with help of eqn. 5.20. Since the β-decay asymmetry factor a is not known for ^{31}Mg, it was assumed to be 1. Taking 0.7 s observation time and the other two factors equal to 0.91 and 0.65, one finally obtains $\overline{A} = 0.6\, P_I$.

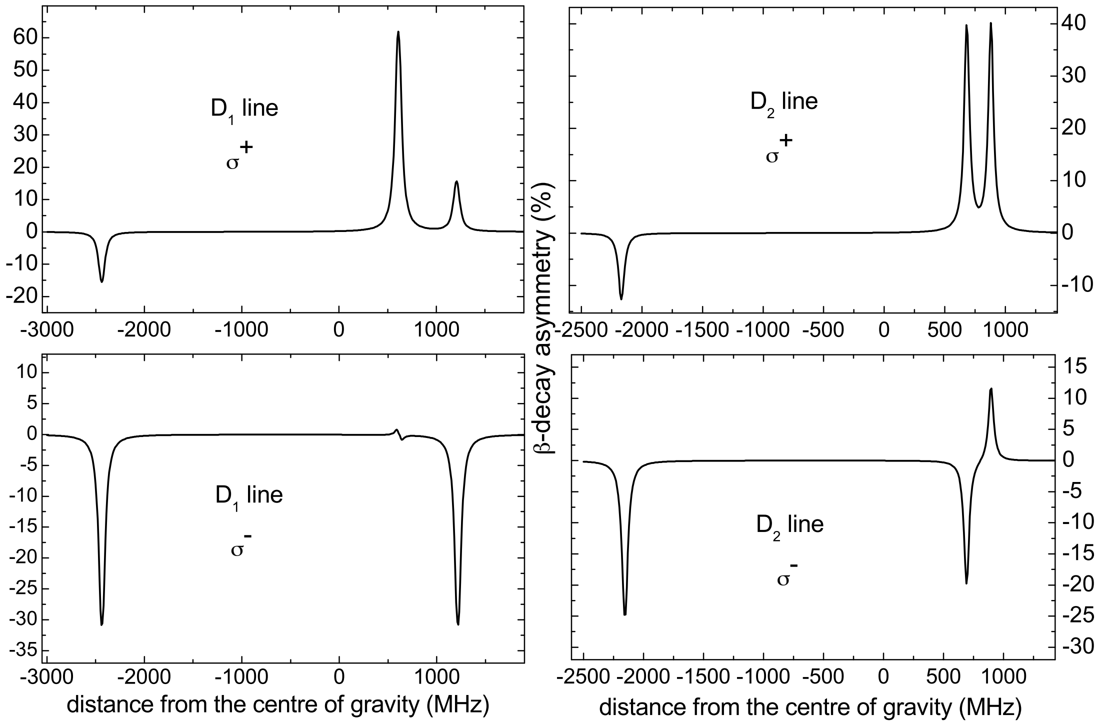

Figure 5.11: Simulations of the β-decay asymmetry reached due to optical pumping of the hyperfine structure of ^{31}Mg, assuming $I = 1/2$.

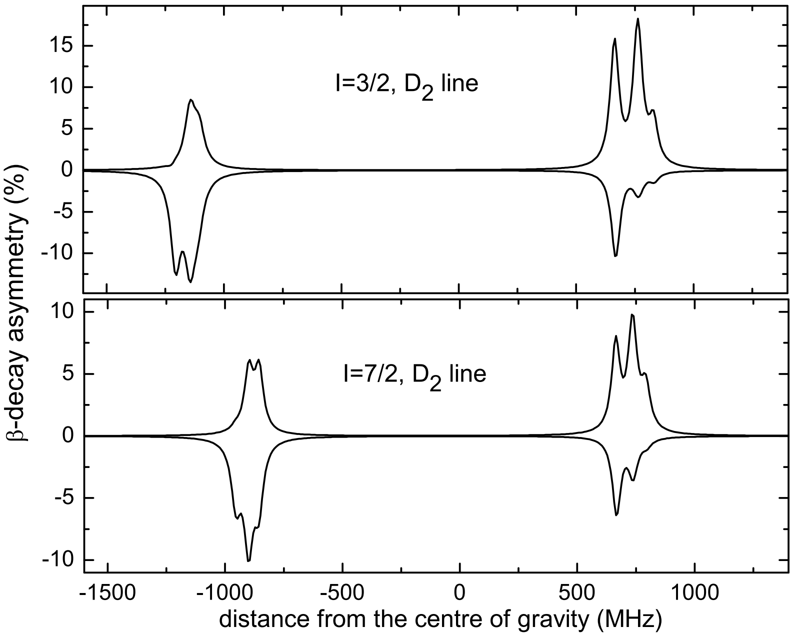

Figure 5.12: Simulations of the nuclear polarisation reached for the hyperfine structure with $I = 3/2$ or $7/2$. Negative peaks for σ^- laser polarisation, positive peaks – σ^+ polarisation.

Table 5.6: The hyperfine A-factors for D_1 and D_2 lines in ^{31}Mg assuming $I = 1/2$.

trans.	state	A-factor (MHz)	σ_{stat} (MHz)	σ_{syst} (MHz)
D_1	$^2S_{1/2}$	−3076.1	5.5	0.3
D_2	$^2S_{1/2}$	−3089.4	6.6	0.3
D_1	$^2P_{1/2}$	−529.9	7.0	0.05
D_2	$^2P_{3/2}$	−95.2	1.4	0.01

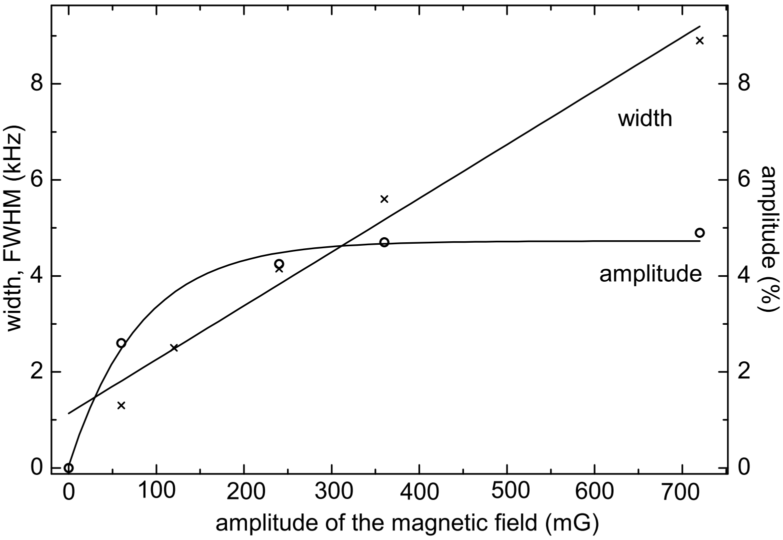

Figure 5.13: Width and amplitude of a Larmor resonance as a function of rf-amplitude, on the example of ^{31}Mg.

5.3.3 Results of β-NMR studies

As described in Section 4.4.2, the β-NMR studies were performed for the ion velocity tuned to the optical resonance giving highest asymmetry. In the case of ^{29}Mg this was the $|F = 2\rangle \rightarrow |F' = 3\rangle$ transition for the D_2 line and σ^+ laser polarisation. For ^{31}Mg, the middle resonance ($|F = 1\rangle \rightarrow |F' = 2\rangle$ transition, assuming I=1/2) in the D_2 transition excited also with σ^+ light was chosen.

With high voltage set at one of these resonances, the frequency of a magnetic radio-field generated in the coil placed around the host crystal was scanned. After the first indications of a Larmor resonance in ^{31}Mg, measurements with different amplitudes of the rf field were performed, since this parameter influences both the amplitude and the width of the NMR resonance (see eqn. 4.36). The results of this test are plotted in Fig. 5.13. The saturation of the resonance for ^{31}Mg took place for about 0.3 G, corresponding to 0.15 A amplitude of the radio-frequency signal flowing through the coil (the width of the resonance for this field was around 4 kHz), therefore this field range was chosen for most of the measurements. This saturation field is 2-3 times larger than predicted (see Fig. 4.9), which is expected due to magnetic-field shielding by the host crystal holder made of copper. NMR scans on ^{29}Mg were, on the other hand, performed with rf amplitude around 0.2 A, which corresponds to magnetic field amplitudes of 0.4 G (and widths of 4 kHz). Examples of typical NMR signals for both studied isotopes are shown in Figs. 5.14 and 5.15.

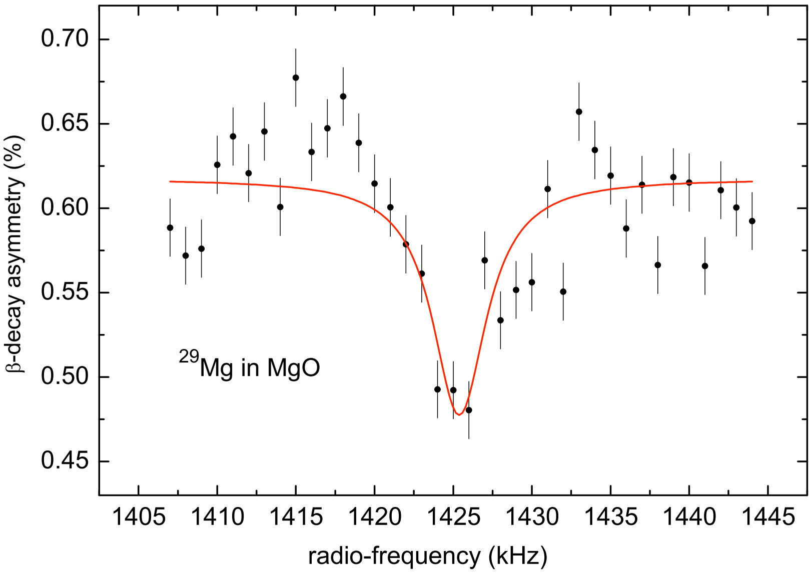

Figure 5.14: A typical β-NMR signal for ^{29}Mg implanted into MgO.

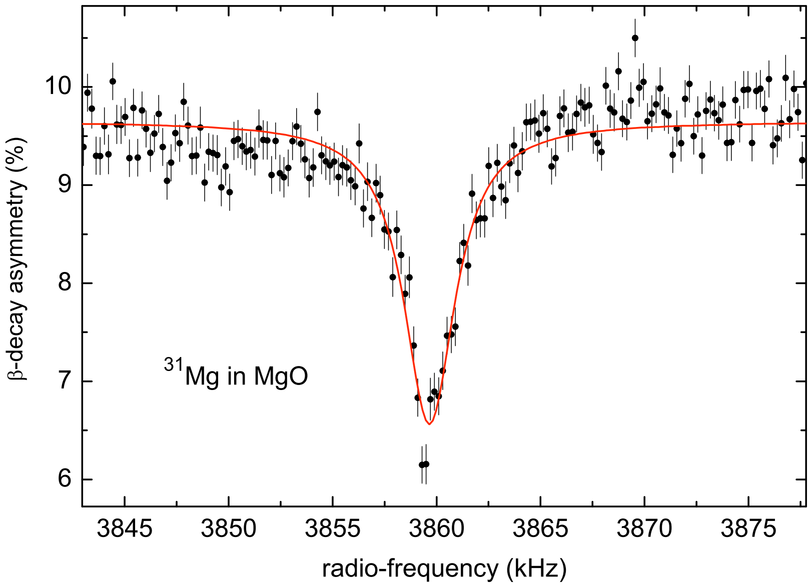

Figure 5.15: Example of β-NMR resonance for ^{31}Mg in MgO.

The NMR spectra were fitted with a Lorentz profile because there was no improvement by including a Gaussian part. This indicates that the inhomogeneous broadening of the spectra can be neglected. The Larmor frequency for ^{29}Mg was evaluated to be 1426.1(16) kHz. The average of 9 measurements in the case of ^{31}Mg gave 3859.73(18) kHz. Within 24-48 hours from the measurements on these two isotopes, β-NMR signals were also recorded for the reference nucleus, ^{8}Li, whose resonance position was evaluated to lie at 1807.03(2) kHz. These results, with their statistical errors, are summarised in Table 5.7.

Table 5.7: Larmor frequencies of ^{29,31}Mg and the reference nucleus ^{8}Li in a MgO crystal.

nucleus	Larmor frequency (kHz)	σ_{stat} (kHz)
^{29}Mg	1426.1	1.6
^{31}Mg	3859.73	0.18
^{8}Li	1807.03	0.02

The absolute values of the nuclear g-factors for both Mg isotopes can now be evaluated, by following eqn. 3.56 and using the known $g_I(^{8}\text{Li})$ [Rag89], as well as the diamagnetic corrections for Mg and Li [Rag89] (see Section 5.1.2):

$$g_I(^{8}\text{Li}) = +0.826780(9)\ , \tag{5.22}$$

$$1/(1-\sigma_{\text{Mg}}) = 0.0007322\ , \tag{5.23}$$

$$1/(1-\sigma_{\text{Li}}) = 0.0001048\ . \tag{5.24}$$

Based on the above values, the calculations yield $|g_I(^{29}\text{Mg})| = 0.653(1)$ and $|g_I(^{31}\text{Mg})| = 1.7671(3)$ (see Table 5.8). The source of the systematic error lies in the uncertainty of $g_I(^{8}\text{Li})$ and in the magnetic field drift between measurements on Mg and Li, as it was discussed in Section 5.1.2. The final errors include random and systematic errors added in quadrature.

Table 5.8: Absolute values of g-factors for ^{29,31}Mg.

nucleus	$\|g$-factor$\|$	σ_{stat}	σ_{syst}	σ_{final}
^{29}Mg	0.653	0.0008	0.0003	0.001
^{31}Mg	1.7671	0.00013	0.00022	0.0003

5.3.4 Combined hyperfine structure and β-NMR results – value of spin and sign of the g-factor

As described in Section 3.4, if one combines the information available from the hyperfine structure and NMR studies, also the spin of a nucleus can be determined independently of the ambiguities in the interpretation of the hyperfine structure pattern. Using eqn. 3.63 and the ground-state splitting (weighted average from D_1 and D_2 lines) for ^{31}Mg, the following value of the spin is derived

$$I(^{31}\text{Mg}) = 0.4992(11)\,, \tag{5.25}$$

which represents spin 1/2.

On the other hand, the hyperfine structure pattern corresponds to a negative A-factor and thus to a negative magnetic moment. Therefore, the g-factor and magnetic moment of this isotope are equal to

$$g_I(^{31}\mathrm{Mg}) = -1.7671(3)\,, \tag{5.26}$$

$$\mu_I(^{31}\mathrm{Mg}) = -0.88355(10)\ \mu_N\ . \tag{5.27}$$

From comparisons with magnetic moments predicted for different nucleon configurations in ^{31}Mg, one can also conclude that the parity of the ground state is positive, hence $I^\pi = 1/2^+$ (more details on the parity assignment will be given in Chapter 6).

The spin of ^{29}Mg was already known to be 3/2 before our studies. Eqn. 3.63 results in $I = 1.49(1)$ and confirms the value available in the literature. Furthermore, the simulations (Fig. 5.9) in comparison with the observed hyperfine structure clearly indicate a positive magnetic moment, hence the final values of μ_I and g_I for this nucleus become

$$g_I(^{29}\mathrm{Mg}) = +0.653(1)\,, \tag{5.28}$$

$$\mu_I(^{29}\mathrm{Mg}) = +0.9795(15)\ \mu_N\ , \tag{5.29}$$

with a positive parity corresponding to a $d_{3/2}$ neutron state (see Chapter 6).

Chapter 6

Interpretation and discussion of results

6.1 Charge radii of stable Mg isotopes

In our studies of changes in mean square charge radii $\langle r^2 \rangle$ no definite measurement has been performed so far for any radioactive Mg isotope. However, our isotope shift measurements on stable isotopes ^{24}Mg, ^{25}Mg and ^{26}Mg show as the most important result that such measurements on radioactive isotopes are feasible. For this, the essential criterion is a resolution and measuring accuracy which is sensitive to the small field shifts yielding $\langle r^2 \rangle$, on top of the huge mass shifts. As a small introduction to the future experiments on radioactive isotopes, one can discuss the charge radii for stable Mg isotopes based on muonic atom data [Fri95] and our isotope shift measurements and their Ne isotones studied recently by our group [Gei05]. Both of them are presented in Fig. 6.1. It is interesting that both isotope chains show similar features: the radii of nuclei ^{24}Mg and ^{22}Ne, $N = 12$ nuclei with 4 neutrons in the $d_{5/2}$ shell, are considerably larger than those of their heavier isotopes. This is an anomalous behaviour, since usually by adding neutrons the charge radius becomes larger, due to the increase in the nuclear volume. Fricke *et al.* [Fri92] give an explanation for this strange behaviour: based on shell model considerations including the proton-neutron interaction for the subshells $d_{5/2}$, $s_{1/2}$ and $d_{3/2}$.

A more obvious phenomenological interpretation can be based on eqn. 2.3 relating the mean square charge radii to deformation. Large deformations of ^{22}Ne and especially ^{24}Mg have been also seen in other observables, such as low energies of their first 2^+ state and large $B(E2)$ values [Ram01], as discussed in Section 1.1.

It will be very interesting to see if the charge radii of ^{27}Mg and heavier isotopes follow the trend in Ne isotopes, and eventually to find out what is the behaviour of more neutron-rich Mg isotopes towards the "island of inversion", which should have large charge radii due to deformations connected with intruder configurations.

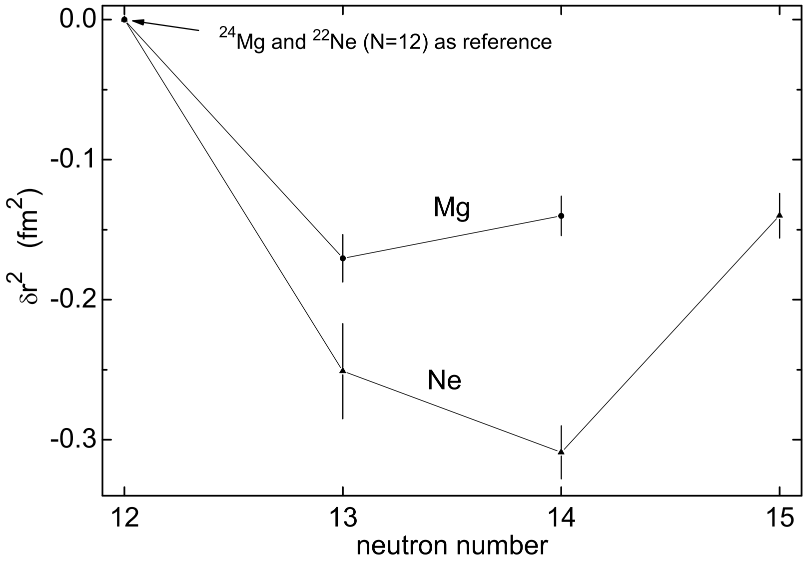

Figure 6.1: Measured changes in mean square charge radii for Mg isotopes, with ^{24}Mg as a reference, and for its closest even-Z neighbour, Ne (^{22}Ne as reference). Source: [Fri95] and [Gei02].

6.2 Magnetic moments of ^{29,31}Mg – towards the island of inversion

6.2.1 Shell model calculations used for comparison with data

Many-particle spherical shell model

In the extreme single-particle spherical shell model, known also as the independent-particle model, each nucleon moves independently in an effective spherical potential formed by all the other nucleons [Gre96]. However, this approximation works well only in nuclei with one particle or hole outside a closed shell. When more valence nucleons are present, a residual interaction between them has to be added to the mean-field potential [Gre96]. In this many-particle shell model most nuclear states are no longer pure single-particle orbits, but they consist of mixtures of different configurations with the nucleons in closed shells as an inert core. This assumption of an inert core does not have to be modified, as long as the interactions and operators are renormalised to compensate for the simplifications, therefore they are known as effective [Bro01]. The main limitation of modern shell model calculation comes from the large dimensions of the many-nucleon Hamiltonian to be diagonalised, which is why the model space, i.e. the orbits which are allowed to be occupied by valence nucleons, has to be limited. This is the reason why even the most successful model will encounter states which are not described by it. These are often called intruder states, and they can be attributed to configurations outside the model space [Bro01]. However, due to increasing computational power and more efficient diagonalisation methods, the shell model has considered progressively larger and larger model spaces, so that states which would be called intruders in a small model space become fully incorporated into a larger space. If the experimental levels are still not described in a satisfactory way with very large model spaces, this can indicate that modifications to the effective residual interaction have to be made. In this Chapter we will see what is the situation for nuclei around the “island of inversion”.

The experimental results on ^{29,31}Mg presented in the previous chapter will be compared to three modern (spherical) shell model calculations, which all assume $^{16}_{8}O_8$ as an inert core and which either block valence neutrons in the *sd* shell, described by the single particle orbits $d_{5/2}$, $s_{1/2}$ and $d_{3/2}$, or allow excitations into the *pf* shell with $f_{7/2}$, $p_{3/2}$, $f_{5/2}$ and $p_{1/2}$ orbits (see Fig. 1.1 for a schematic presentation of the above shells and orbits).

The first of these interactions, the USD [Bro88] developed by the Michigan group, allows the valence protons and neutrons to move in the full *sd* shell. It was developed around 1985 and is based on experimental data from stable and close-to-stable nuclei available at that time. USD was updated to USD-05 in 2005 to include new experimental results collected since 1985. The predictions of the energies of different levels in ^{29,31}Mg for the 2005 version are very close to the ones of the original USD interaction [Bro06], but there are so far no g-factor predictions and, furthermore, the updated interaction is not yet available publicly. Therefore, in this thesis, only results of calculations using the original USD will be presented.

The SDPF.SM interaction, known also as iokin.spdf.si35 [Ret97], [Cau02] by the Madrid-Strasbourg groups, extends over the full *sd* shell for the valence protons and the full *sd* and *pf* shells for the neutrons, since it is aimed to study the very neutron-rich isotopes with $Z < 20$. It includes the USD interaction for the *sd* shell (see above), a modified Kuo-Brown interaction [Pov81] for the *pf* shell (obtained from the renormalisation of the G-matrix), as well as the G-matrix of Lee, Kahana, and Scott [Kah69] for the cross-shell part.

In the last interaction, SDPF-M [Uts99] by the Tokyo group, the valence orbits for protons and neutrons include the full *sd* shell plus the $f_{7/2}$ and $p_{3/2}$ single-particle orbitals. As for SDPF.SM, the effective interaction consists of slightly modified three parts: USD for the *sd* shell, Kuo-Brown [Kuo68] for *pf* shell, and a modified Millener-Kurath interaction for *sd*-*pf* interaction [Mil75]. Moreover, in a recently modified version, SDPF-M’, which was also used in the calculations presented below, the *pf* terms have been replaced by a new interaction, GXPF1 [Hon04], developed in 2004 and including more terms that improve the description of the “island of inversion”.

Because the last two interactions both allow particles into the *pf* shell, but differ in some matrix elements, it is worth to compare them, in order to better interpret the theoretical results and to understand the sources of possible deviations in their predictions. Fig. 6.2 gives a graphical comparison between the effective single-particle energies for neutrons at $N = 20$ and $Z = 8 - 20$ calculated with both interactions. SDPF.SM and SDPF-M give very similar effective single particle energies for $d_{3/2}$, $f_{7/2}$ and $p_{3/2}$ orbits in nuclei with $Z = 14-20$. For the remaining nuclei, however, they diverge. And thus, at $Z = 8$, SDPF-M predicts the $p_{3/2}$ orbit below $f_{7/2}$ and gives a two times smaller shell gap (between $d_{3/2}$ and $f_{7/2}$) than SDPF.SM. The latter effect is mainly due to the upwards shift of the $d_{3/2}$ orbit for low-Z nuclei related to the proton-neutron interaction suggested by Otsuka *et al.*, as described in Section 1.2.1. Evidently, due to the smaller *sd*-*pf* gap, SDPF-M will produce enhanced correlations and an enlarged “island of inversion”. We will see further what implications it gives for the theoretical description of ^{31}Mg.

All presented calculations were performed using free nucleon g-factors, i.e. for the proton $g_\ell = 1$, $g_s = 5.58$ and for the neutron $g_\ell = 0$, $g_s = -3.81$. This approach is motivated by studies on other elements in this area (see e.g. [Him06b]) and arguments pointed out

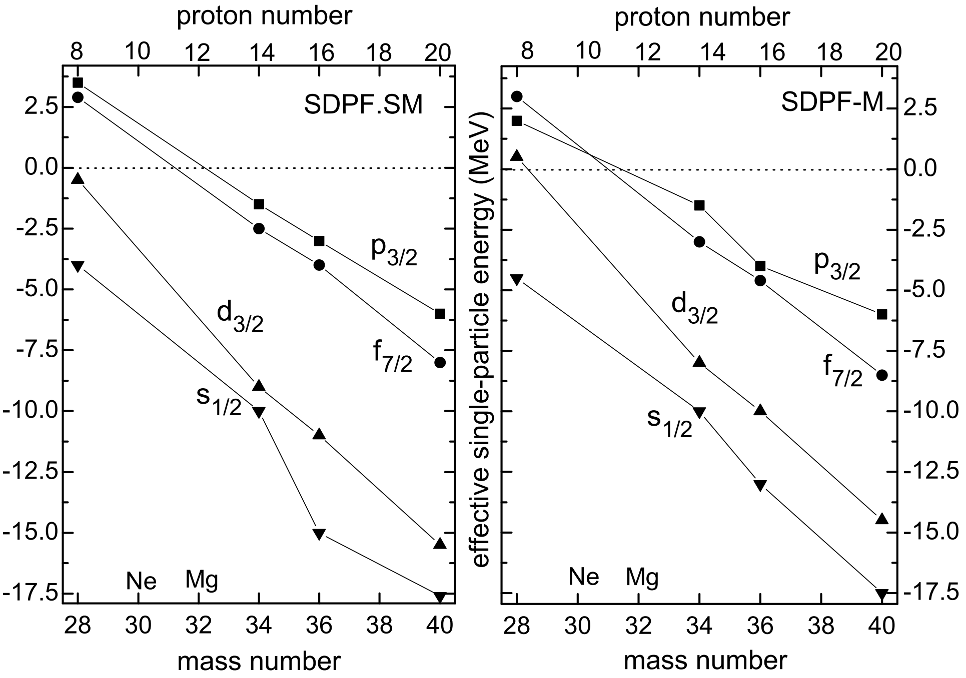

Figure 6.2: Predicted effective single-particle energies for neutrons at $N = 20$ as a function of the proton number for SDPF.SM (left) and SDPF-M (right) interactions. Adopted from [Cau02].

by Brown and Wildenthal [Bro88]. However, according to Utsuno *et al.* [Uts04], for their SDPF-M interaction effective g-factors give better overall predictions. The main motivation is a very good description of Na isotopes with these values [Uts04], as well as the truncation to $f_{7/2}$ and $p_{3/2}$ orbits. Therefore for this interaction also results with effective g-factors: $g_\ell^p = 1.15$, $g_\ell^n = -0.15$, and $g_s^p = 5.027$, $g_s^n = -3.4437$, as well as the tensor part arising from the dipole-dipole interaction within the nucleus $g_p^p = 0.5$ and $g_p^n = -0.5$, will be given for comparison.

The two first described interactions, USD and SDPF.SM, are available publicly in the library of a shell model code ANTOINE [Cau06], which makes use of the so called m-scheme to diagonalise the many-particle Hamiltonian. Therefore, all results based on them and presented in this thesis were performed with this code (some of the values were already available in the literature, thus they served as a cross-check). The matrix elements for the modification of SDPF.SM, called SDPF.NR, are not available publicly, therefore results for this interaction are based only on published values. On the other hand, the code used by the Tokyo group (for SDPF-M and SDPF-M' interactions) is based on the Monte Carlo sampling to restrict the orbits in the model space according to the importance of a configuration. This code is not open to the public, thus in this case the values given in the thesis are based on published results and on private communication with the authors.

Deformed shell model – Nilsson model

In the shell model, the effective potential in which each nucleon moves independently is spherical and the possible deformation of a nucleus in a given state is due to the residual interaction between the valence nucleons causing a collective movement. The nuclear deformation can, however, be included phenomenologically already in the mean-field potential without the need of using residual interaction [Gre96]. This approach results in the so called deformed shell model, also known as the Nilsson model, introduced in 1955 by S.G. Nilsson [Nil55].

In a deformed potential the energy of the state depends on the orientation of single-particle motion with respect to the nuclear symmetry axis, and levels with angular momentum j are not degenerate. Therefore in the Nilsson model it is customary to label the single-particle levels with the set of quantum numbers $K^{\pi}[Nn_zm]$ [Gre96]. K is the projection of the total angular momentum on the symmetry axis (taken as z direction), π represents the parity, N is the principal quantum number denoting the major shell, n_z the number of quanta in the z-direction and m stands for the component of the orbital angular momentum along the z axis.

By investigating the ordering of states in a given nucleus one can derive the deformation parameter β which was introduced in Section 2.1. Furthermore, one can also make predictions of different observables, such as the magnetic moment, as a function of β. This model will therefore also be used to interpret our ^{31}Mg results.

6.2.2 Comparison with theory and interpretation of measured spin and g-factor of ^{29}Mg

For ^{29}Mg we obtained the following results: $I = 3/2$ (confirmation of previous assignment) and $g_I = +0.653(1)$ (see Section 5.3.4). In the extreme single-particle picture the ground state properties of this nucleus, which has 12 protons and 17 neutrons, should be governed by one unpaired neutron in the $d_{3/2}$ shell. This implies $I^{\pi} = 3/2^{+}$, which agrees with our observations and gives us additional information concerning the parity of the ground state. The corresponding g-factor, based on the Schmidt formula, is expected to be +0.764 (eqn. 2.9). This is close to the measured value, but the agreement is not prefect, which indicates that configuration mixing plays a role.

Before presenting results of many-particle shell model calculations, it is interesting to compare the g-factor of ^{29}Mg to other measured g_I of nuclei with even Z and one unpaired neutron (or hole) in the $d_{3/2}$ shell, i.e. $N = 17$ or 19. In Fig. 6.3 it is visible that the ^{29}Mg g-factor is close to the g-factors of $N = 19$ neighbours, which are all comparable with the Schmidt value. Surprisingly, the results for isotones of ^{29}Mg are almost two times lower. This might indicate that for $N = 17$ in nuclei with more protons than Mg, such as S and Ar, the neutron $d_{3/2}$ configuration is less pure than in other cases. This is confirmed by the USD calculations, which reproduce very well all g-factors in Fig. 6.3 and which show that in the ground states of ^{33}S and ^{35}Ar proton excitations play a much larger role than in ^{29}Mg or the $N = 19$ isotones.

Our results are now compared to the many-particle spherical shell model predictions. Fig. 6.4 shows the experimental and theoretical energies and g-factors for several lowest lying levels in ^{29}Mg. The $3/2^{+}$ state is found at 50 keV with the USD interaction, but taking into account the usual accuracy of the shell model in the range of 100 keV, this state is degenerate with the $1/2^{+}$ the ground state. This interpretation is supported by the results of the two other calculations, which give the right ordering: $I = 3/2^{+}$ as the ground state and $I = 1/2^{+}$ about 50 keV higher. Also the measured g-factor agrees remarkably well with

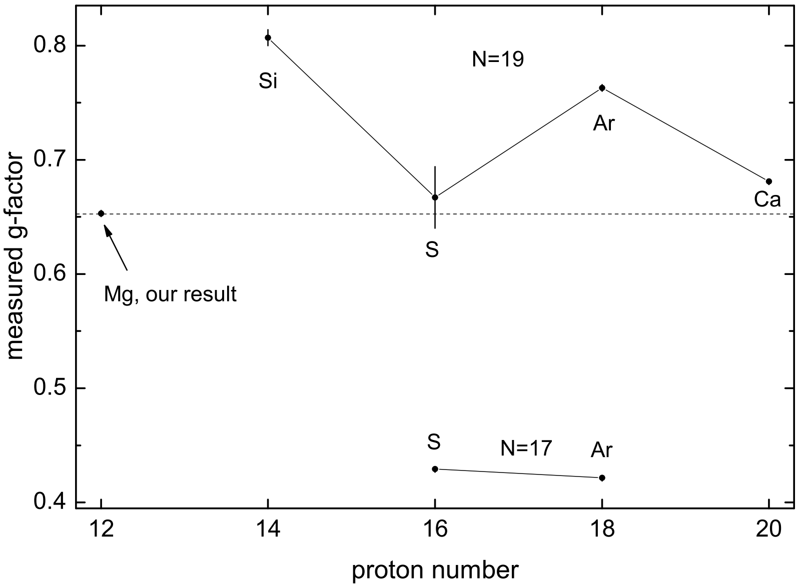

Figure 6.3: Experimental g-factors for even-Z odd-N nuclei with one unpaired neutron in the $d_{3/2}$ shell ($N = 17$ or 19). Source [Rag89], [Sto05] and our measurements.

predictions of all three interactions which deviate from the experimental value by less than 8 % in the worst case. Moreover, all predict this level to be an almost pure $(d_{5/2})^6(s_{1/2})^2d_{3/2}$ configuration for neutrons and $(d_{5/2})^4$ for protons, therefore its g-factor is so close to the Schmidt value.

This comparison with theory shows firmly that the ground state of ^{29}Mg, with spin-parity of $3/2^+$ and the g-factor of +0.653(1), can be described very well with existing shell model interactions using only the sd shell and free-nucleon g-factors. Thus, this nucleus lies clearly outside the "island of inversion".

6.2.3 Comparison with theory and interpretation of measured spin and g-factor of ^{31}Mg

In the case of the more exotic ^{31}Mg ($N = 19$) the extreme single-particle predictions are the same as for ^{29}Mg (i.e. $I^\pi = 3/2^+$ and $g_{Schmidt} = +0.764$), since they are based on one unpaired neutron in the $d_{3/2}$ shell. Our measured spin is 1/2 and, thus, it excludes the simple picture of one unpaired neutron in the $d_{3/2}$ orbit and the two remaining $d_{3/2}$ neutrons coupled to spin 0. There are several possible explanations for this unexpected spin, even if one assumes only neutron excitations, since the proton $d_{5/2} - s_{1/2}$ gap is large and makes proton excitations into $s_{1/2}$ or $d_{5/2}$ orbits in the ground state very improbable. The first obvious candidate for $I_{gs} = 1/2$ is the neutron configuration $s_{1/2}(d_{3/2})^4$ (yielding positive parity), which is the only way to stay within the sd shell. All other scenarios involve promotion of neutrons to the pf shell, e.g. $(s_{1/2})^2d_{3/2}(f_{7/2})^2$ (two neutrons in the pf shell, which yields positive parity). To decide which scenario is correct, Fig. 6.5 presents excitation energies and g-factors of the lowest states in ^{31}Mg for the three residual interactions described before.

From this comparison the following conclusions can be made: the USD interaction, which

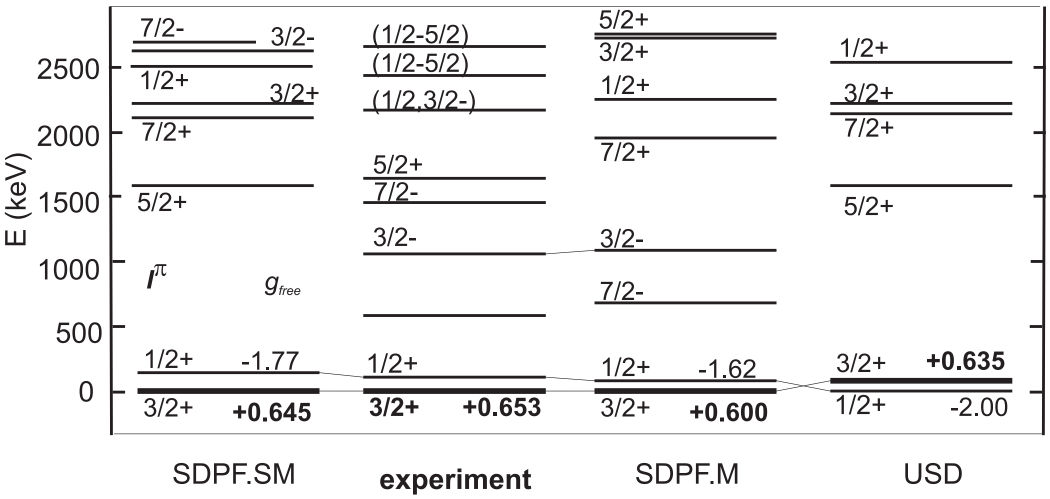

Figure 6.4: Measured and predicted excitation energies and g-factors for the ground and lowest excited states in ^{29}Mg. Experimental results from [Bau89] and our measurements [Kow06], theoretical values from own calculations, [Bro06], [Smi06] and [Uts06].

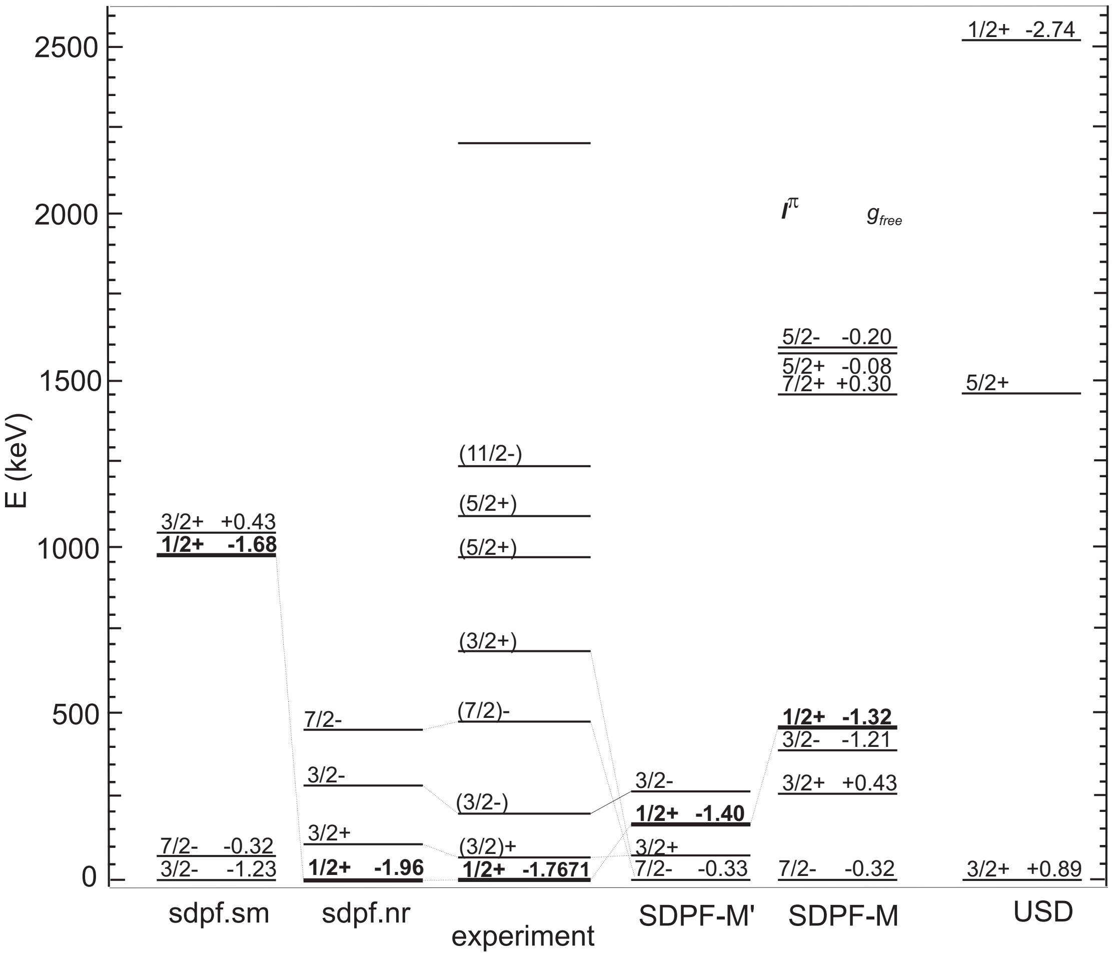

Figure 6.5: Measured and predicted excitation energies, spins, parities and g-factors for ground and lowest excited states in ^{31}Mg. Experimental results from [Klo93], [Mac05] and our measurements [Ney05]. Theory: own calculations, [Ney05], [Mar05], [Bro06], [Ots06], [Uts06] and [Smi06].

restricts valence neutrons to *sd* shell, cannot reproduce the observed $I = 1/2$ level as the ground state, and not even as a low lying state. The lowest $I = 1/2$ state (of positive parity), corresponding to the $s_{1/2}(d_{3/2})^4$ configuration, appears at 2.5 MeV. Moreover, although the corresponding value of the g-factor has the same sign as the measured g-factor, it is by 50 % larger. On the other hand, for both interactions allowing neutrons into pf orbits the predicted level scheme and g-factor of the lowest 1/2 state are much closer to the experimental value. In the case of SDPF.SM with up to 6 neutrons in the $f_{7/2}p_{3/2}$ orbits and no mixing between configurations which have different number of neutrons in the pf shell, there is a $1/2^+$ state composed purely of two neutrons promoted across the shell gap. It appears at about 1 MeV excitation energy and has $g_I = -1.68$ (calculated with free-nucleon g-factors), based on the present calculations and the correspondence with N. Smirnova [Smi06]. The agreement is even better for SDPF-M, which also allows several neutrons in the $f_{7/2}p_{3/2}$ orbits, but includes mixing. It predicts a $1/2^+$ level at only 500 keV with the g-factor equal to -1.70 (with free-nucleon g-factors, compared to -1.32 with effective g-factors) [Ots06], [Uts06], [Ney05]. Also in this approach the 1/2 state is composed almost entirely (about 96 %) of configurations with two neutrons in the pf shell. The newer interaction of the Tokyo group, SPDF-M', gives even better agreement with the experimental energies: the $1/2^+$ state goes down to 300 keV. However, the predicted g-factor is slightly worse and equals -1.4 (free-nucleon g-factors, otherwise -1.2) [Ots06], [Uts06].

Both the Strasbourg-Madrid and Tokyo interactions predict intruder states from the pf shell at lower energies than the *sd*-only configurations, which agrees with the experiment. However, the negative-parity states with one neutron in the pf shell are still placed lower than the observed $1/2^+$ ground state. In this situation it is hard to decide which of the two *sd*-*pf* interactions gives a better description of ^{31}Mg.

As shown by the above discussion, the experimental g-factor and spin of the ^{31}Mg ground state are both in good agreement with the shell model predictions made with interactions existing at the time of our studies, if at least two neutrons are promoted across the $N = 20$ gap. Theory predicts that this level has positive parity and is located much lower than the first *sd*-only $I = 1/2$ configuration. However, a 1/2-state is not predicted as the ground state, but only as one of the low lying states. So far, there exists only one theoretical calculation in full agreement with the experiment [Mar05], which is based on the SDPF.NR interaction [Cau05] and includes $sd - f_{7/2}p_{3/2}$ neutron orbits. Its results are also shown in Fig. 6.5. SDPF.NR is a modification of the SDPF.SM interaction, which aims to describe best ^{31}Mg without changing the description of some neighbouring nuclei, such as ^{33}Mg and ^{35}Si. The fact that it yields a spin 1/2 ground state with $g_I = -1.97$ is a very positive result, however, one should keep in mind that it is much easier to explain experimental results *a posteriori* by applying modifications to the model, rather than to predict the results of a measurement *a priori* without changing details of the interaction. Hence, it remains to be seen if forthcoming measurements, e.g. I and g_I of ^{33}Mg, can be predicted properly *a priori* with this interaction.

Discussing the shape of this nucleus, its rich low-energy spectrum clearly suggests a deformed ground state, in which a neutron hole is coupled to a deformed core of ^{32}Mg ($N = 20$). In the deformed shell model, a $1/2^+$ ground state for $N = 19$ corresponds to a $1/2^+[200]$ configuration coming from the $d_{3/2}$ spherical orbit, which has to get above the $1/2^-[330]$ orbit from the spherical $f_{7/2}$ state, as presented in Fig. 6.6. The $K = 1/2^+$ orbit crosses

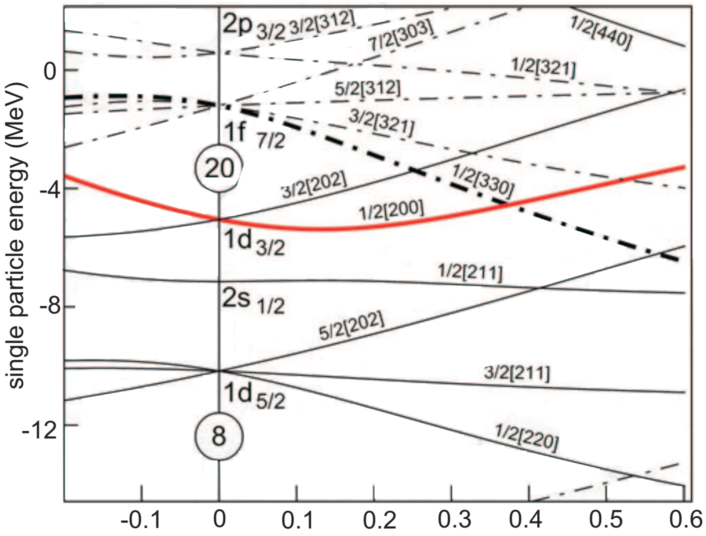

Figure 6.6: Single particle energy of various levels in the Nilsson model as a function of the deformation parameter β. The $1/2^+[200]$ level becomes the ground state of ^{31}Mg for deformations larger than $\beta = 0.4$.

$K = 1/2^-$ only for a deformation parameter $\beta \approx 0.4$, which means that the ground state of ^{31}Mg is very deformed. The experimental g-factor of the $1/2^+$ state is reproduced extremely well for a very large deformation parameter, $\beta \approx 0.5$ yielding $g_I = -1.78$ [Mar05]. Marechal *et al.* [Mar05] also calculated g-factors of other low-lying states in this nucleus, and found a surprising agreement with the spherical shell model calculations using SDPF.SM interaction. This result supports the interpretation of the ground state of ^{31}Mg as being a well-deformed structure due to promotion of neutrons across the *sd*-*pf* shell gap.

Based on the measured spin and magnetic moment of the $1/2^+$ ground state of ^{31}Mg, the present conclusion can be expressed as follows: already in its ground state this nucleus requires a promotion of at least two neutrons into the *pf* shell, and thus it belongs to the "island of inversion". Furthermore, the Nilsson shell model indicates a large deformation for this nucleus, $\beta \approx 0.5$, which confirms the importance of intruder *pf* states. Hence, the "island of inversion" for Mg isotopes starts already at $N = 19$, as was suggested by Otsuka *et al.* (see Section 1.2.2). An open problem, however, remains in the difficulty to predict the $I = 1/2^+$ configuration as the actual ground state. This can be an indication that neutrons have to be allowed into the full *pf* shell and not only into the two lowest shells, and that full mixing between all possible states should be included. There is, indeed, presently an effort to perform calculations in the full *pf* shell with mixing between different configurations [Uts06], which will hopefully improve the situation. Another explanation for the difference between the experiment and theory is the possibility that interactions used to describe this region of the nuclear chart are still not optimal. The necessity to explicitly include three-body forces can be one reason for this situation.

It remains to be seen what are the ground state properties of other Mg isotopes of the "island of inversion", such as ^{33}Mg, and if the existing models can predict them correctly. One has to remember that there are scarce data available for cross-shell nuclei. Therefore both experimental and theoretical effort in such regions of the nuclear chart are crucial for a better understanding of the nuclear force in the nuclear medium.

Chapter 7

Summary and outlook

In the frame of this thesis I presented measurements concerning charge radii of stable ^{24}Mg, ^{25}Mg and ^{26}Mg, as well as ground state spins, g-factors and magnetic moments of short-lived ^{29}Mg and ^{31}Mg. This study was motivated by the poor understanding of the borders and the physics mechanism of the so called “island of inversion”, which is a region of the nuclear chart around $Z = 10$-12 and $N = 20$ where the picture of a closed $N = 20$ neutron shell breaks down.

The experiments were performed at the ISOLDE facility at CERN, using collinear laser and β-NMR spectroscopy to study radioactive nuclei produced by the impact of a 1.4 GeV proton beam. The Mg isotopes were investigated with continuous-wave laser beams as singly charged ions in the 280-nm transition from the atomic ground state $^2S_{1/2}$ to one of the two lowest excited states $^2P_{1/2,\,3/2}$. In the fluorescence detection the isotope shifts of stable Mg isotopes were successfully studied. It was shown that the achieved precision makes it possible to extract the tiny field shift, and based on it to derive the differences in nuclear charge radii also for short-lived Mg isotopes with low production yields. A very high sensitivity of the β-asymmetry detection allowed successful measurements of the hyperfine splitting and nuclear magnetic resonance on short lived ^{29}Mg and ^{31}Mg with half-lives around 1 s. Thanks to efficient optical pumping with UV light generated by a dye laser and an external frequency doubler, β-asymmetries close to saturation were obtained. To observe this asymmetry the ions were implanted into a host cubic crystal lattice of MgO. This allowed to determine the g-factor with relative uncertainty as low as 0.02 %. The combination of both methods allowed also the measurement of an unknown spin of ^{31}Mg and the confirmation of the spin of ^{29}Mg.

The results concerning differences in charge radii of stable Mg isotopes, and the expected uncertainty in measurements on more exotic isotopes, show clearly that it is feasible to extend these measurements towards the “island of inversion”. On the other hand, the measured spins and magnetic moments of more neutron-rich Mg isotopes and their comparison to modern shell model calculations showed that ^{29}Mg has a ground state dominated by one unpaired neutron in the $d_{3/2}$ orbit. At the same time, the ground state of ^{31}Mg is very deformed and requires promotion of at least two neutrons into the next major shell, leaving behind 3 holes in the *sd* shell and giving rise to the unexpected $1/2^+$ spin-parity. These results show clearly that for Mg isotopes at $N = 17$ the closed *sd* shell is still a correct description, whereas for $N = 19$ promotion of neutrons across the *sd*-*pf* shell gap takes place already in the ground state. There remains, however, still one problem: the $1/2^+$ configuration could not be predicted *a priori* as the ground state, and only *a posteriori* modifications in the otherwise successful residual interactions succeed in this task. Current effort to enlarge the model space to the full pf shell will hopefully bring instructive results.

The studies presented in this thesis are now being extended. On one hand, measurements of differences in mean square charge radii are planned for isotopes beyond ^{26}Mg, which for more exotic nuclei, like ^{29}Mg and ^{31}Mg, will be performed not by fluorescence detection, but via β-decay asymmetry. On the other hand, β-NMR measurements will soon be carried out on the even more exotic ^{33}Mg, which represents an experimental challenge, because the half-life is only 90 ms and the yield will be less than 10 000 atoms per second.

Bibliography

[Abr61] A. Abragam, *The principles of nuclear magnetism*, 1961.

[Ahm88] S.A. Ahmad et al., *Mean square charge radii of radium isotopes and octupole deformation in the* $^{220-228}$*Ra region*, Nuclear Physics A **483** (1988), 244.

[Ans89] W. Ansbacher, Y. Li, and E.H. Pinnington, *Precision lifetime measurement for the 3p levels of MgII using frequency-doubled laser radiation to excite a fast ion beam*, Physics Letters A **139** (1989), 165.

[Ari54] A. Arima and H. Horie, *Configuration Mixing and Magnetic Moments of Odd Nuclei*, Progress of Theoretical Physics **12** (1954), 623.

[Arn87] E. Arnold, J. Bonn, R. Gegenwart, W. Neu, R. Neugart, E.-W. Otten, G. Ulm, K. Wendt, and ISOLDE Collaboration, *Nuclear Spin and Magnetic Moment* ^{11}*Li*, Physics Letters B **197** (1987), 311.

[Aud03] G. Audi, A.H. Wapstra, and C. Thibault, *The AME2003 atomic mass evaluation*, Nuclear Physics A **729** (2003), 337.

[Aud06] G. Audi, A.H. Wapstra, and C. Thibault, *Accurate mass measurements of* ^{26}*Ne,* $^{26-30}$*Na,* $^{29-33}$*Mg performed with the MISTRAL spectrometer*, Nuclear Physics A **766** (2006), 52.

[Bar70] R.C. Barrett, *Model-independent parameters of the nuclear charge distribution from muonic x-rays*, Physics Letters B **33** (1970), 388.

[Bar89] R.J. Barlow, *Statistics: a guide to the use of statistical methods in the physical sciences*, 1989.

[Bau89] P. Baumann et al., *Beta decay of* ^{30}Na*: Experiment and theory*, Physical Review C **39** (1989), 626.

[Ber03] J.C. Berengut, V.A. Dzuba, and V.V. Flambaum, *Isotope-shift calculations for atoms with one valence electron*, Physical Review A **68** (2003), 022502.

[Bev69] P.R. Bevington, *Data reduction and error analysis for the physical sciences*, 1969.

[Bla52] J. Blatt and V. Weisskopf, *Theoretical nuclear physics*, 1952.

[Bli57] R.J. Blin-Stoyle and M.A. Grace, *Oriented nuclei*, Handbuch der Physik **42** (1957), 555.

[Blu85] S.A. Blundell, P.E.G. Baird, C.W.P. Palmer, D.N. Stacey, G.K. Woodgate, and D. Zimmermann, *A re-evaluation of isotope shift constants*, Zeitschrift für Physik A **321** (1985), 31.

[Boh50] A. Bohr and V. Weisskopf, *The Influence of Nuclear Structure on the Hyperfine Structure of Heavy Elements*, Physical Review **77** (1950), 94.

[Bra86] B.H. Bransden and C.J. Joachain, *Physics of atoms and molecules*, 1986.

[Bro88] B.A. Brown and B.H. Wildenthal, *Status of the nuclear shell model*, Annual Review of Nuclear and Particle Science **38** (1988), 29.

[Bro01] B.A. Brown, *The Nuclear Shell Model Towards the Drip Lines*, Progress in Particle and Nuclear Physics **47** (2001), 517.

[Bro06] B. A. Brown Home Page, http://www.nscl.msu.edu/˜ brown.

[Buc82] F. Buchinger, A.C. Mueller, B. Schinzler, K. Wendt, C. Ekstrom, W. Klempt, and R. Neugart, *Fast-Beam Laser Spectroscopy on Metastable Atoms Applied to Neutron-Deficient Ytterbium Isotopes*, Nuclear Instruments and Methods in Physics Research **202** (1982), 159.

[Cam75] X. Campi, H. Flocard, A. K. Kerman, and S. Koonin, *Shape transition in the neutron rich sodium isotopes*, Nuclear Physics A **251** (1975), 193.

[Cas90] B. Castel and I.S. Towner, *Moder Theories of Nuclear Magnetic Moments*, 1990.

[Cau98] E. Caurier, F. Nowacki, A. Poves, and J. Retamosa, *Shell model study of the neutron rich isotopes from oxygen to silicon*, Physical Review C **58** (1998), 2033.

[Cau02] E. Caurier, F. Nowacki, and A. Poves, *Large-scale shell model calculations for exotic nuclei*, European Physical Journal A **15** (2002), 145.

[Cau05] E. Caurier, G. Martinez-Pinedo, F. Nowacki, A. Poves, and A.P. Zucker, *Shell model study of the neutron rich isotopes from oxygen to silicon*, Review of Modern Physics **77** (2005), 427.

[Cau06] E. Caurier, ANTOINE webpage, http://sbgat194.in2p3.fr/˜ theory/antoine/menu.html.

[Chi01] V. Chiste et al., *Electric and nuclear transition strength in* $^{30,32}Mg$, Physics Letters A **514** (2001), 233.

[Chu80] W. Chung and B.H. Wildenthal, *Collapse of the conventional shell-model ordering in the very neutron-rich isotopes of Na and Mg*, Physical Review C **22** (1980), 2260.

[Com99] Committee on Nuclear Physics and National Research Council, *Nuclear Physics: The Core of Matter, The Fuel of Stars*, 1999.

[Dem03] W. Demtröder, *Laser Spectroscopy*, 2003.

[Det79] C. Detraz et al., *Beta decay of* $^{27-32}Na$ *and their descendants*, Physical Review C **19** (1979), 164.

[Eid04] S. Eidelman et al., *Review of Particle Physics*, Physics Letters B **592** (2004), 1.

[Fed00] V.N. Fedoseyev et al., *The ISOLDE laser ion source for exotic nuclei*, Hyperfine Interactions **127** (2000), 409.

[Fir03] R. Firestone and V. Shirley, *Table of the Isotopes*, 1996. R. Firestone, LBNL Isotopes Project Nuclear Data Dissemination Home Page (last update in 2003), http://ie.lbl.gov/toi.html.

[Fri92] G. Fricke et al., *Behavior of the nuclear charge radii systematics in the sd shell from muonic atom measurements*, Physical Review C **45** (1992), 80.

[Fri95] G. Fricke et al., *Nuclear Ground State Charge Radii from Electromagnetic Interactions*, Atomic Data and Nuclear Data Tables **60** (1995), 177.

[Fuk92] N. Fukumishi, T. Otsuka, and T. Sebe, *Vanishing of the shell gap in N=20 neutron-rich nuclei*, Physics Letters B **296** (1992), 279.

[Gei99] W. Geithner et al., *Measurement of the magnetic moment of the one-neutron halo nucleus* ^{11}Be, Physical Review Letters **83** (1999), 3792.

[Gei02] W. Geithner, *PhD Thesis, CERN-THESIS-2002-030*, 2002.

[Gei05] W. Geithner et al., *Nuclear moments of neon isotopes in the range from* ^{17}Ne *at the proton drip line to the neutron-rich* ^{25}Ne, Physical Review C **71** (2005), 064319.

[Geo95] U. Georg et al., *Changes in mean-square nuclear charge radii from optical isotope shifts*, International Conference on Exotic Nuclei and Atomic Masses: ENAM '95 (1995), 133.

[Gre96] W. Greiner and J.A. Maruhn, *Nuclear models*, 1996.

[Han87] P.G. Hansen and B. Jonson, *Isotope-shift calculations for atoms with one valence electron*, Europhysics Letters **4** (1987), 409.

[Hei74] K. Heilig and A. Steudel, *Changes in mean-square nuclear charge radii from optical isotope shifts*, Atomic Data and Nuclear Data Tables **14** (1974), 613.

[Him06a] P. Himpe et al., *submitted*, Physical Review C (2006).

[Him06b] P. Himpe, *PhD Thesis*, 2006.

[Hon04] M. Honma, T. Otsuka, B.A. Brown, and T. Mizusaki, *New effective interaction for pf-shell nuclei and its implications*, Physical Review C **69** (2004), 034335.

[Hub78] G. Huber et al., *Spins, magnetic moments, and isotope shifts of* $^{21-31}Na$ *by high resolution laser stectroscopy of the atomic* D_1 *line*, Physical Review C **18** (1978), 2342.

[Ike66] H. Ikegami and M. Sano, *Effect of collective vibrational motion on the anomalous coupling states*, Physics Letters **21** (1966), 323.

[Ita81] W.M. Itano and D.J. Wineland, *Precision measurement of the ground-state hyperfine constant of* $^{25}Mg^{+}$, Physical Review A **24** (1981), 1343.

[Iwa01] H. Iwasaki, T. Motobayashi, H. Sakurai, K. Yoneda, et al., *Large collectivity of* ^{34}Mg, Physics Letters B **522** (2001), 227.

[Iwa05] H. Iwasaki, T. Motobayashi, H. Sakurai, K. Yoneda, et al., *Quadrupole collectivity of* ^{28}Ne *and the boundary of the island of inversion*, Physics Letters B **620** (2005), 118.

[Jam75] F. James and M. Roos, *Minuit - a system for function minimization and analysis of the parameter errors and correlations*, Computer Physics Communications **10** (1975), 343.

[Jam04] F. James and M. Winkler, *MINUIT User's Guide*, www.cern.ch/seal (2004).

[Kah69] S. Kahana, H.C. Lee, and C.K. Scott, *Effect of Woods-Saxon Wave Functions on the Calculation of* $A = 18$*, 206, 210 Spectra with a Realistic Interaction*, Physical Review **180** (1969), 956.

[Kau76] S. Kaufman, *High-resolution laser spectroscopy in fast beam*, Optical Communications **17** (1976), 309.

[Kei00] M. Keim, U. Georg, A. Klein, et al., *Measurement of the electric quadrupole moments of* $^{26-29}Na$, European Physical Journal A **1** (2000), 31.

[Kel39] J.M.B. Kellogg, I.I. Rabi, N.F. Ramsey Jr., and J.R. Zacharias, *An Electrical Quadrupole Moment of the Deuteron*, Physical Review **55** (1939), 318.

[Kin84] W.H. King, *Isotope Shifts in Atomic Spectra*, 1984.

[Kin86] W.H. King and W.P. Palmer, *Isotope Shifts: How Much Can Be Deduced from the Field Shift?*, Comments on Optical and Molecular Physics **18** (1986), 11.

[Kle95] A. Klein, *PhD Thesis*, 1995.

[Kle96] A. Klein et al., *Moments and mean square charge radii of short-lived argon isotopes*, Nuclear Physics A **607** (1996), 1.

[Klo93] G. Klotz et al., *Beta decay of* $^{31,32}Na$ *and* ^{31}Mg*: Study of the* $N = 20$ *shell closure*, Physical Review C **47** (1993), 002502.

[Koe03] U. Köster, V.N. Fedoseyev, and V.I. Mishin, *Resonant laser ionization of radioactive atoms*, Spectrochimica Acta B **58** (2003), 1047.

[Kop69] H. Kopfermann, *Nuclear moments*, 1969.

[Kow05] M. Kowalska, D. Yordanov, et al., *Laser and* β*-NMR spectroscopy on neutron-rich magnesium isotopes*, European Physics Journal A **25s01** (2005), 193.

[Kow06] M. Kowalska et al., *publication in preparation.*

[Kra86] K.S. Krane, *Low-temperature nuclear orientation* (N.J. Stone and H. Postma, eds.), 1986.

[Kra88] K.S. Krane, *Introductory nuclear physics*, 1988.

[Kug00] E. Kugler, *The ISOLDE facility*, Hyperfine Interactions **129** (2000), 23.

[Kuo68] T.T.S. Kuo and G.E. Brown, *Reaction matrix elements for the 0f-1p shell nuclei*, Nuclear Physics A **114** (1968), 241.

[Mac05] H. Mach et al., *New structure information on ^{30}Mg, ^{31}Mg and ^{32}Mg*, European Physical Journal A **25s01** (2005), 105.

[Mar92] A. MårtenssonPendrill, A. Ynnerman, H. Warston, L. Vermeeren, R.E. Silverans, A. Klein, R. Neugart, C. Schulz and P. Lievens., *Isotope shifts and nuclear-charge radii in singly ionized $^{40-48}Ca$*, Physical Review A **45** (1992), 4675.

[Mar05] F. Marechal et al., *β decay of ^{31}Mg: Extending the "island of inversion"*, Physical Review C **72** (2005), 044314.

[Mat71] E. Matthias, B. Olsen, D.A. Shirley, J.E. Templeton, and R.M. Steffen, *Theory of Nulear Magnetic Resonance Detected by Nuclear Radiations*, Physical Review A **4** (1971), 1626.

[Mil75] D.J. Millener and D. Kurath, *The particle-hole interaction and the beta decay of ^{14}B*, Nuclear Physics A **255** (1975), 315.

[Moh05] P.J. Mohr and B.N. Taylor, *CODATA recommended values of the fundamental physical constants: 2002*, Review of Modern Physics **77** (2005), 1.

[Mot95] T. Motobayashi et al., *Large deformation of the very neutron-rich nucleus ^{32}Mg from intermediate-energy Coulomb excitation*, Physics Letters B **346** (1995), 9.

[Mue83] A.C. Müller et al., *Spins, moments and charge radii of barium isotopes in the range $^{122-146}Ba$ determined by collinear fast-beam laser spectroscopy*, Nuclear Physics A **403** (1983), 234.

[Neu81] R. Neugart et al., *Laser Spectroscopy on Mass-Separated Radioactive Beams*, Nuclear Instruments and Methods in Physics Research **186** (1981), 165.

[Neu86] R. Neugart, W. Klempt, and K. Wendt, *Collisional ionization as a sensitive detection scheme in collinear laser-fast-beam spectroscopy*, Nuclear Instruments and Methods in Physics Research B **17** (1986), 354.

[Neu06] R. Neugart and G. Neyens, *Nuclear Moments*, Lecture Notes in Physics **700** (2006), 117.

[Ney05] G. Neyens, M. Kowalska, D. Yordanov, K. Blaum, P. Himpe, P. Lievens, S. Mallion, R. Neugart, N. Vermeulen, Y. Utsuno, and T. Otsuka, *Measurement of the Spin and Magnetic Moment of ^{31}Mg: Evidence for a Strongly Deformed Intruder Ground State*, Physical Review Letters **94** (2005), 022501.

[Nil55] S.G. Nilsson, *Binding States of Individual Nucleons in Strongly Deformed Nuclei*, Kongelige Danske Videnskabernes Selskab matematisk-fysiske meddelelser **29** (1955), 16.

[Nil95] S.G. Nilsson and I. Ragnarsson, *Shapes and shells in nuclear structure*, 1995.

[Ots01] T. Otsuka, R. Fujimoto, Y. Utsuno, B.A. Brown, M. Honma, and T. Mizusaki, *Magic Numbers in Exotic Nuclei and Spin-Isospin Properties of the NN Interaction*, Physical Review Letters **87** (2001), 082502.

[Ots05] T. Otsuka et al., *Evolution of Nuclear shells due to the Tensor Force*, Physical Review Letters **95** (2005), 232502.

[Ots06] T. Otsuka, private communication.

[Pat91] S.K. Patra and C.R. Praharaj, *Relativistic mean field study of "island of inversion" in neutron-rich Ne, Na, Mg nuclei*, Physics Letters B **273** (1991), 13.

[Poe96] D. Poenaru and W. Greiner, *Handbook of Nuclear Properties*, 1996.

[Pov81] A. Poves and A. Zuker, *Quasiconfigurations and the theory of effective interactions*, Physics Reports **70** (1981), 4.

[Pov87] A. Poves and J. Retamosa, *The onset of deformation at the $N = 20$ neutron shell closure far from stability*, Physics Letters B **184** (1987), 311.

[Pre02] W.H. Press, S.A. Teukolsky, W.T. Vetterling, and B.P. Flannery, *Numerical Recipes in C++*, 2002.

[Pri99] B.V. Pritychenko et al., *Role of intruder configurations in ^{26,28}Ne and ^{30,32}Mg*, Physics Letters B **461** (1999), 322.

[Rag89] P. Raghavan, *Table of nuclear moments*, Atomic data and Nuclear Data Tables **42** (1989), 189.

[Ram01] S. Raman, C.W. Nestor Jr., and P. Tikkanen, *Transition probability from the ground to the first-excited 2^+ state of even-even nuclides*, Atomic Data and Nuclear Data Tables **78** (2001), 1.

[Ren96] Z. Ren, Z.Y. Zhu, Y.H. Cai, and G. Xu, *Relativistic mean-field study of Mg isotopes*, Physics Letters B **380** (1996), 241.

[Ret97] J. Retamosa, E. Caurier, F. Nowacki, and A. Poves, *Shell model study of the neutron rich nuclei around $N = 28$*, Physical Review C **55** (1997), 1266.

[Rin80] P. Ring and P. Schuck, *The Nuclear Many Body Problem*, 1980.

[Ris55] P. Risberg, *Spectrum of singly ionized magnesium, MgII*, Arkiv för Fysik **9** (1955), 483.

[Ros32] J.E. Rosenthal and G. Breit, *The Isotope Shift in Hyperfine Structure*, Physical Review **41** (1932), 459.

[San06] R. Sánchez et al., *Nuclear Charge Radii of ^{9,11}Li: The Influence of Halo Neutrons*, Physical Review Letters **96** (2006), 033002.

[Sch35] H. Schüler and T. Schmidt, *Über Abweichungen des Atomkerns von der Kugelsymmetrie*, Zeitschrift für Physik **94** (1935), 457.

[Sch90] C.P. Schlichter, *Principles of Magnetic Resonance*, 1990.

[Sch91] Ch. Schulz et al., *Resonance ionization spectroscopy on a fast atomic ytterbium beam*, Journal of Physics B **24** (1991), 4831.

[Sch05] H. Scheit et al., *Coulomb excitation of neutron-rich beams at REX-ISOLDE*, European Physics Journal A **25** (2005), 397.

[Sel69] E.C. Seltzer, *K X-ray isotope shifts*, Physical Review A **188** (1969), 1916.

[Sil88] R.E. Silverans et al., *Nuclear Charge Radii of $^{78-100}$Sr by Nonoptical Detection in Fast-Beam Laser Spectroscopy*, Physical Review Letters **60** (1988), 2607.

[Smi06] N. Smirnova, private communication.

[Sob96] I. Sobelman, *Atomic Spectra and Radiative Transitions*, 1996.

[Sto83] M.H. Storm, A. Watt, and R.R. Whitehead, *Crossing of single-particle energy levels resulting from nneutron excess in the sd shell*, Journal of Physics G **9** (1983), L165.

[Sto05] N.J. Stone, *Table of nuclear magnetic dipole and electric quadrupole moments*, Atomic Data and Nuclear Data Tables **90** (2005), 75.

[Sun91] D. Sundholm and J. Olsen, *Element MCHF Calculations on Mg(3s3p;$^3P^0$): the Nuclear Quadrupole Moment of ^{25}Mg*, Nuclear Physics A **534** (1991), 360.

[Tan85] I. Tanihata et al., *Measurements of interaction cross sections and nuclear radii in the light p-shell region*, Physical Review Letters **55** (1985), 2676.

[Ter97] J. Terasaki et al., *Deformation of nuclei close to the two-neutron drip line in the mg region*, Nuclear Physics A **621** (1997), 706.

[Thi75] C. Thibault et al., *Direct measurement of the masses of ^{11}Li and $^{26-32}$Na with an on-line mass spectrometer*, Physical Review C **12** (1975), 644.

[Tor85] G. Torbohm, B. Fricke, and A. Rosén, *State-dependent volume isotope shifts of low-lying states of group-IIa and -IIb elements*, Physical Review A **31** (1985), 2038.

[Ulm86] G. Ulm, S.K. Bhattacherjee, P. Dabkiewicz, G. Huber, H.-J. Kluge, T. Kuhl, H. Lochmann, E.W. Otten, S.A. Ahmad K. Wendt, W. Klempt, and R. Neugart, *Isotope shift of ^{182}Hg and an update of nuclear moments and charge radii in the isotope range ^{181}Hg–^{206}Hg*, Zeitschrift für Physik **325** (1986), 247.

[Uts99] Y. Utsuno, T. Otsuka, T. Mizusaki, and M. Honma, *Varying shell gap and deformation in $N \sim 20$ unstable nuclei studed by the Monte Carlo shell model*, Physical Review C **60** (1999), 054315.

[Uts02] Y. Utsuno, T. Otsuka, T. Mizusaki, and M. Honma, *Monte Carlo shell model calculation for unstable nuclei around $N = 20$*, Nuclear Physics A **704** (2002), 50c.

[Uts04] Y. Utsuno, T. Otsuka, T. Glasmacher, T. Mizusaki, and M. Honma, *Onset of intruder ground state in exotic Na isotopes and evolution of the $N = 20$ shell gap*, Physical Review C **70** (2004), 044307.

[Uts06] Y. Utsuno, private communication.

[War90] E.K. Warburton, J.A. Becker, and B.A. Brown, *Mass systematics for $A = 29{-}44$ nuclei: The deformed $A \sim 32$ region*, Physical Review C **41** (1990), 1147.

[Web82] R. Weber, B. Jeckelmann, J. Kern, U. Kiebele, et al., *Spectroscopic quadrupole moments of ^{25}Mg and ^{27}Al from muonic X-rays*, Nuclear Physics A **377** (1982), 361.

[Wil98] S. Wilbert et al., *β-NMR measurement of the nuclear quadrupole moments of ^{20,26,31}Na*, AIP Conference Proceedings **455** (1998), 142.

[Woo80] G.K. Woodgate, *Elementary Atomic Structure*, 1980.

[Yan03] Y. Yanagisawa et al., *The First Excited State of ^{30}Ne Studied by Proton Inelastic Scattering in Reversed Kinematics*, Physics Letters B **566** (2003), 84.

[Yon01] K. Yoneda et al., *Deformation of ^{34}Mg studied via in-beam gamma-ray spectroscopy using radioactive-ion projectile fragmentation*, Physics Letters B **499** (2001), 233.